THE UNIVERSITY OF
TECHNOLOGY, SYDNEY

Faculty of Engineering

An Investigation of the Dynamic Characteristics of Hydraulic Power Steering Systems

A thesis submitted for the degree of

Doctor of Philosophy
in Engineering

Miao Wang

Nov 2006

CERTIFICATE OF AUTHORSHIP / ORIGINALITY

I certify that the work in this thesis has not previously been submitted for a degree nor has it been submitted as part of requirements for a degree except as fully acknowledged within the text.

I also certify that the thesis has been written by me. Any help that I have received in my research work and the preparation of the thesis itself has been acknowledged. In addition, I certify that all information sources and literature used are indicated in the thesis.

Signature of Candidate

Production Note:
Signature removed prior to publication.

Acknowledgements

The author wishes to sincerely thank the following people for offering much needed help and support during this research.

First of all, my sincere gratitude goes to my supervisor, Dr. Nong Zhang, for his confidence in my ability, his guidance and encouragement and for his generosity of offering so much time in helping me throughout the whole program.

I would also like to thank my co-supervisor, Dr Jeku Jeyakumaran, for his valuable advice and support.

My thanks also go to Mr. Chris Chapman for his willing and very helpful assistance with so many aspects of the laboratory procedures.

I am grateful to my colleagues within the project team who have given me support and encouragement: Dr. William Hu and PhD candidate Wade Smith.

Finally, my special thanks go to my wife Tina for her love and support throughout this research.

Table of contents

List of figures

Figure **Page**

List of tables

Table **Page**

Abstract

The dynamic characteristics of the rack and pinion hydraulic power steering systems have been investigated in the time domain and the frequency domain by using modelling, simulation and testing methods. A model of the hydraulic power steering system and the numerical solution scheme were developed in order to obtain the time domain responses of the system. For the frequency domain analysis, a state space representation of the system incorporating the dynamics of the mechanical and hydraulic subsystems was proposed and the system coefficient matrices were derived. A root searching method was developed to determine the natural frequencies and corresponding modes of the steering system. Applications to a typical hydraulic power steering system were conducted to validate the developed models and computational schemes. The results obtained from the frequency domain analysis agreed well with those obtained from the transient analysis. The examples illustrated the dynamic coupling between the mechanical and hydraulic subsystems. In addition, the dynamic characteristics of the variable ratio rack and pinion steering system and the speed sensitive steering system were investigated.

A hydraulic power steering system test rig, which provided an approximately realistic working environment for the hydraulic steering system, was designed and built to validate the mathematical models. A series of experiments including the impact testing on the front wheel, the steering shudder testing and the pressure ripple testing were carried out. The experimental results confirmed the presented modelling and simulation analysis.

The models and test rig may assist automotive engineers in performing theoretical noise and vibration analysis of the steering system for optimising its performance. The modelling methods and numerical solution scheme which reveal the mechanical and hydraulic coupling action can be applied to the dynamics study of other complex mechanical/hydraulic systems.

CHAPTER 1 INTRODUCTION

1.1 Overview of the research

Steering systems are basic and crucial systems in ground bourne vehicles. With the steering system, a driver applies a torque on the steering wheel and controls the driving direction. If the front axle load due to the weight of the vehicle gets higher, the manual torque required to turn the steering wheel gets higher. Therefore, power assisted steering systems, including hydraulic power steering systems and electric power steering systems, are widely used in modern vehicles to increase the handling performance of vehicles and reduce the required input torque on the steering wheel, and hence, driver fatigue. Though facing a challenge from electric power steering systems in recent years, hydraulic power steering systems still dominate the automotive market because of their higher assisting force, higher reliability and lower cost.

The hydraulic steering system with the rack and poinion gear is one of the most popular hydraulic steering systems and the dynamic characteristics of the system are the main concerns of this research. The main dynamic components of a typical hydraulic power rack and pinion steering system are the steering wheel, input shaft, rotary spool valve, rack and pinion gear, pump, hydraulic cylinder, hydraulic hoses, tie rod linkages, front wheels and front tyres. During a steering process, the rotational displacement between the sleeve and spool of the rotary spool valve is generated by the driver's steering input. This rotational displacement regulates high pressure fluid to one side of the piston in the hydraulic cylinder and discharges the low pressure fluid from the other side of the cylinder to the reservoir. The force from the rack and pinion gear, together with the pressure difference between the two sides of the piston provides the force to steer the two front wheels.

Although the hydraulic power steering system has many advantages, there are quite a few different vibration and noise phenomena existing in the system, including the steering shudder, steering wheel nibble, steering shimmy, etc. Since the steering system affect the driving comfort of the driver, as well as the ride and handling of the vehicle, a large amount of effort have been dedicated by researchers both in academic institutes and industrial organisations to analyse the dynamic characteristics of the

system and to minimise the noise and vibration. While the analytical and experimental methods have been used to investigate the vibration in hydraulic power steering systems and the improvement has been achieved by different measures, there are few theoretical models and explanations to unveil the coupling and interaction of the mechanical and hydraulic components in these frequency-dependent systems.

In this research, the dynamic characteristics of typical rack and pinion hydraulic power steering systems are investigated in time domain and frequency domain. The mathematical models and a steering system test rig are developed, and the numerical simulation and experiments are conducted.

A broad and thorough literature survey has been done and it covers the research outcomes on different power steering systems. This includes the latest achievements in the field obtained by some of the most prestigious steering system research and development organisations. The vibration and noise phenomena are grouped and discussed, the various theoretical methods and models are compared and analysed. Based on the literature survey, the appropriate dynamics theories for mechanical and hydraulic components are chosen, and the mathematical models of the hydraulic power steering system are illustrated.

During the modelling process, the hydraulic power steering system is firstly divided into two subsystems, the mechanical subsystem and the hydraulic subsystem. The two subsystems are discussed by different theories because of their evidently different features. The mechanical subsystem is modelled as a multi-degree of freedom system and the one-dimensional linear resistance compressible flow model is adopted to analyse the hydraulic subsystem. Then, the two subsystems are combined and the steering system is analysed as an integrated system. The free vibration analysis of the mechanical subsystem is conducted to investigate natural frequencies and mode shapes of the mechanical subsystem. The numerical calculation of the whole system is adopted to investigate the time domain responses of the whole steering system under various inputs.

The variable ratio steering system and the speed sensitive steering system are the important improvements of the conventional hydraulic steering system. The variable ratio system contains the variable ratio rack and pinion gear to improve the vehicle drivability, and the speed sensitive system has a specially designed rotary spool valve to enable different hydraulic boost responses. Many unique dynamic characteristics of these two systems have not been investigated theoretically. The two systems are investigated in this research based on the extensional forms of the hydraulic power steering system model.

In this research, a fundamental study of the coupling of the mechanical and hydraulic components is presented. After using the transfer matrix method and conducting a transformation process, a novel system matrix coupling the mechanical and hydraulic components of the power steering system is developed and a root searching method is adopted to locate the natural frequencies of the frequency-dependent steering system.

A test rig for testing hydraulic power steering systems is designed and built. This rig covers all the dynamic components of the steering system and provides a general simulation platform for the hydraulic power steering system in the laboratory.

The frequency domain analysis of the system matrix, the numerical simulation of the time domain steering system model and testing results are compared and discussed.

1.2 Research objectives

While the analytical and experimental studies have been carried out to investigate vibration in hydraulic power steering systems and continuous improvement has been achieved by other researchers, there is a need to discover a comprehensive theoretical model and to explain the dynamic coupling and interaction of the mechanical and hydraulic components in the integrated system.

The key objectives of this research are:

- Develop the time domain mathematical models of hydraulic power steering systems, including the mechanical and hydraulic components,

- Develop the mathematical models of speed sensitive and variable ratio steering systems,
- Develop the coupled system matrix of steering systems and conduct the frequency domain analysis,
- Design and build a test rig and carry out the experiments to validate the mathematical model,
- Analyse the mathematical model and experimental data to investigate the dynamic characteristics of hydraulic steering systems.

1.3 Outline of thesis

This thesis consists of nine chapters. This chapter presents an overview of the research. In Chapter 2, the structure and the key components of a typical hydraulic power steering system is introduced folowed by a literature review which shows the current knowledge of hydraulic power steering systems. Also, the methods and theories used in this research are presented. Chapter 3 illustrates the details of the comprehensive mathematical model, including the mechanical subsystem, the supply line, the rotary spool valve and the hydraulic cylinder/piston unit. In Chapter 4, the results of the free vibration analysis of the mechanical subsystem and the transient simulation of the hydraulic steering system are presented. In Chapter 5, after a coupled system matrix is developed, the natural frequencies of the integrated system are determined and the mechanical and hydraulic coupled system frequencies are analysed. By extending the steering system model developed in Chapter 3, Chapter 6 discusses two particular power steering systems: the variable ratio system and the speed sensitive system. Chapter 7 describes the design of the test rig which is used to test the steering system. Chapter 8 focuses on the analysis of the experimental data. The summary and conclusion are presented in Chapter 9.

CHAPTER 2 BACKGROUND AND LITERATURE REVIEW

2.1 Structure of hydraulic power steering systems

The components of a typical hydraulic power steering can be grouped in two categories: the mechanical components and hydraulic components. It should be mentioned that, in this thesis, the "mechanical components" and "mechanical subsystem" of the hydraulic power steering system represent the mechanism components and the multi-body subsystem of the system, whereas the "hydraulic components" and "hydraulic subsystem" stands for the hydraulic circuit components and the hydraulic circuit. The mechanical components generally include steering wheel, steering column, torsional bar, rack and pinion gear, tie rods and front wheels. The steering pump, reservoir, high-pressure and low pressure hoses, rotary spool valve, feed pipes and the actuator cylinder/piston unit are the hydraulic components. Figure 2.1 [Harter *et al.* (2000)] shows a typical hydraulic power steering system.

2.1.1 Rack and pinion steering gear

The function of the steering gear is to transfer the rotational movement of the steering wheel to the translational movement of the tie rods. The rack and pinion gear is one of the most popular steering gears, and it can be equipped in a wide range of vehicles, from small size passenger cars and light vans to luxury sedans and high performance roadsters. Therefore, this research focus on the hydraulic steering system equipped with a rack and pinion gear. Figure 2.2 [website 1] is a schematic of the rack and pinion gear steering system.

When the driver turns the steering wheel, the torque is transferred to the pinion by the steering shaft through two universal joints. The rack is driven by the pinion, and it pushes the tie rods to the left or right. Then the front two wheels are turned by the steering arms which are connected with the tie rods.

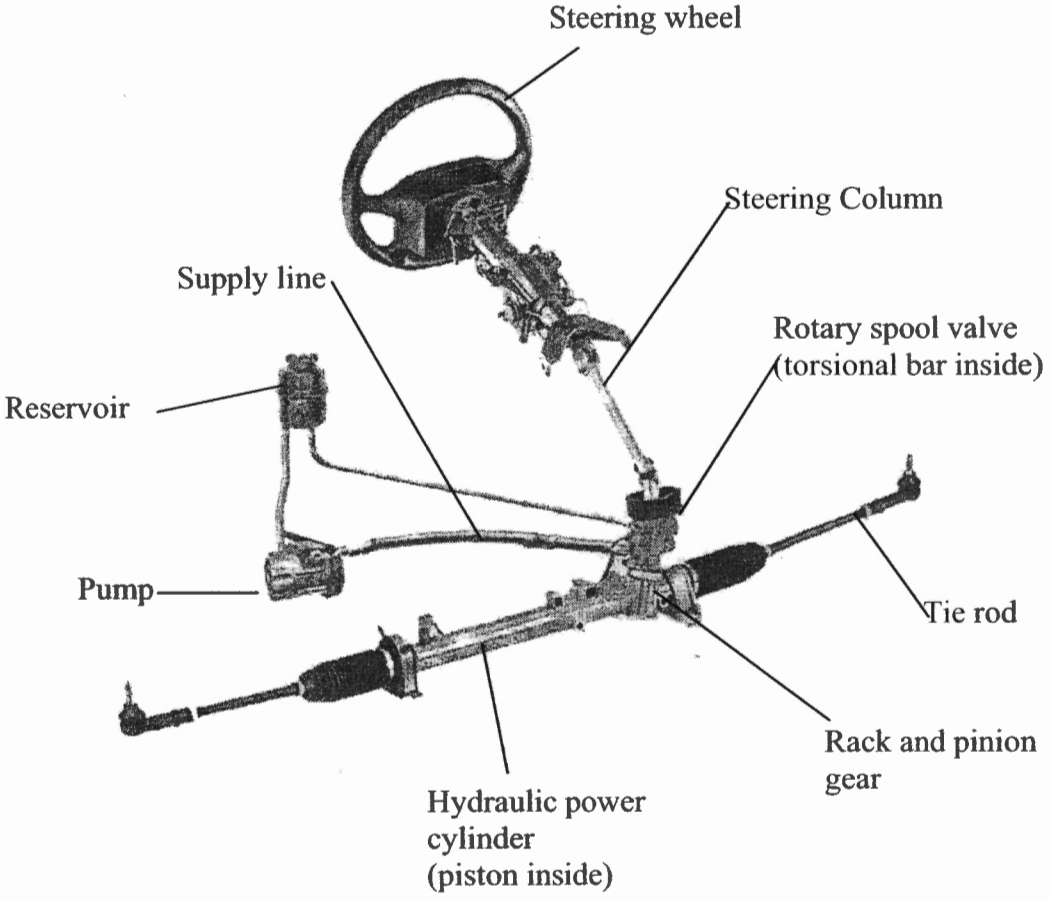

Fig. 2.1 A typical hydraulic power steering system

[Harter *et al.* (2000)]

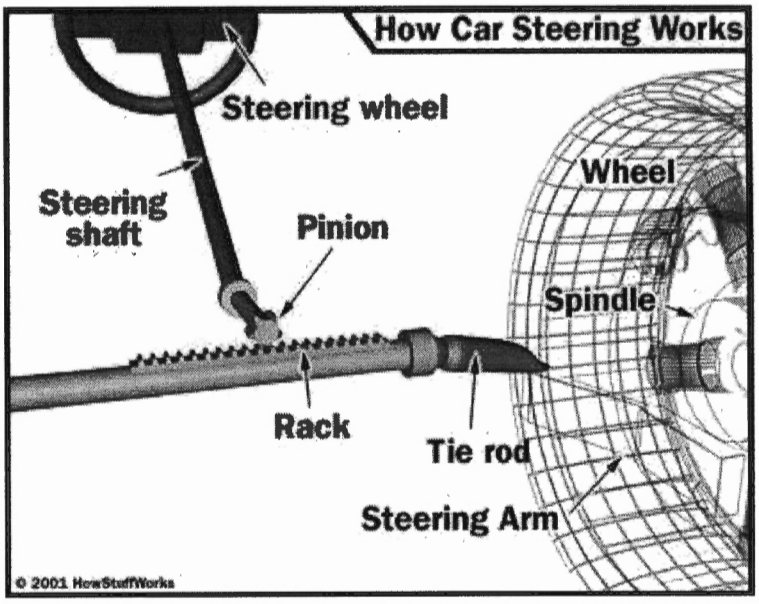

Fig. 2.2 Detail of the rack and pinion gear [website 1]

2.1.2 Rotary spool valve

The rotary spool valve (also called control valve) is one of the most important parts of a hydraulic power steering system. Figures 2.3 and 2.4 are photos of the disassembled and assembled rotary spool valve respectively. A typical rotary spool valve includes the valve sleeve, the valve spool, the torsional bar and the pinion. One end of the torsional bar (also called T-bar) is fixed to the pinion, and the other end is connected to the steering column. Also, the sleeve is fixed to the pinion and the spool is connected to the steering column. As a result, if the driver turns the steering wheel, the torque from the steering column twists the torsional bar and generates an angle difference between the valve sleeve and spool. This angle difference controls the fluid circuit of the system.

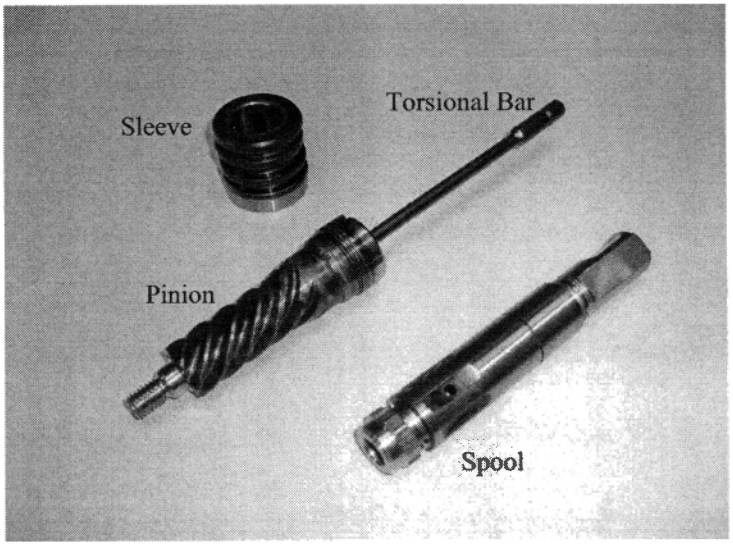

Figure 2.3 Disassembled rotary spool valve

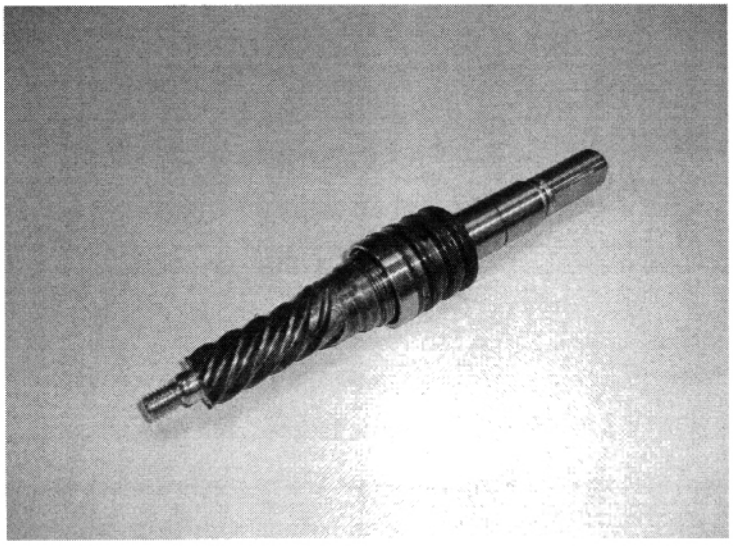

Figure 2.4 Assembled rotary spool valve

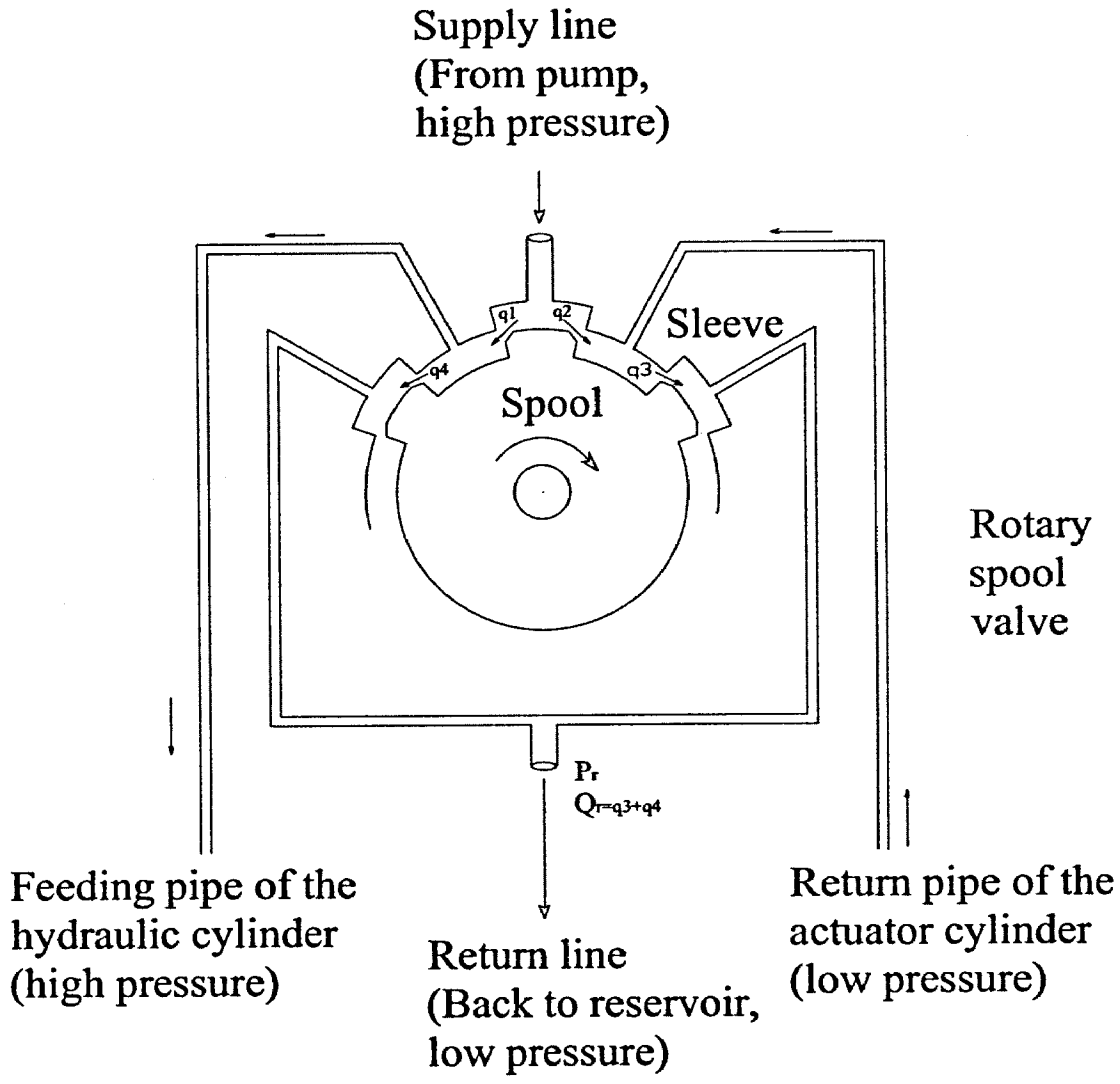

Fig. 2.5 Schematic of rotary spool valve

Figure 2.5 shows a schematic of the fluid circuit of the rotary spool valve. When the steering wheel is turned to right, the torsional bar is twisted and angle difference (also called angle error) occurs between the spool and the sleeve of the valve. The flow rates q1 and q3 increase, while q2 and q4 decrease. The high pressure fluid goes left to the feed pipe of the hydraulic power cylinder, and applies high pressure on left side of the

piston. Simultaneously, through the return pipe, the low pressure fluid in right side of the cylinder goes back to the reservoir.

The characteristics of the rotary spool valve are usually designed as per customer requirements, and are non-linear in nature. A typical valve curve is shown in Figure 2.6 [Delphi (2004)]. The horizontal axis is the angle difference (in degrees) between the spool and the sleeve, and the vertical axis is hydraulic inlet pressure (psi and MPa). The dashed lines and solid lines with different weights represent the performance of the valves with different profiles. It can be seen from the figure that the pressure does not change much when the angle different is relative small, but the pressure increases dramatically if the angle is above certain value. This feature is one reason for the vibration of steering systems and will be discussed in the following chapters.

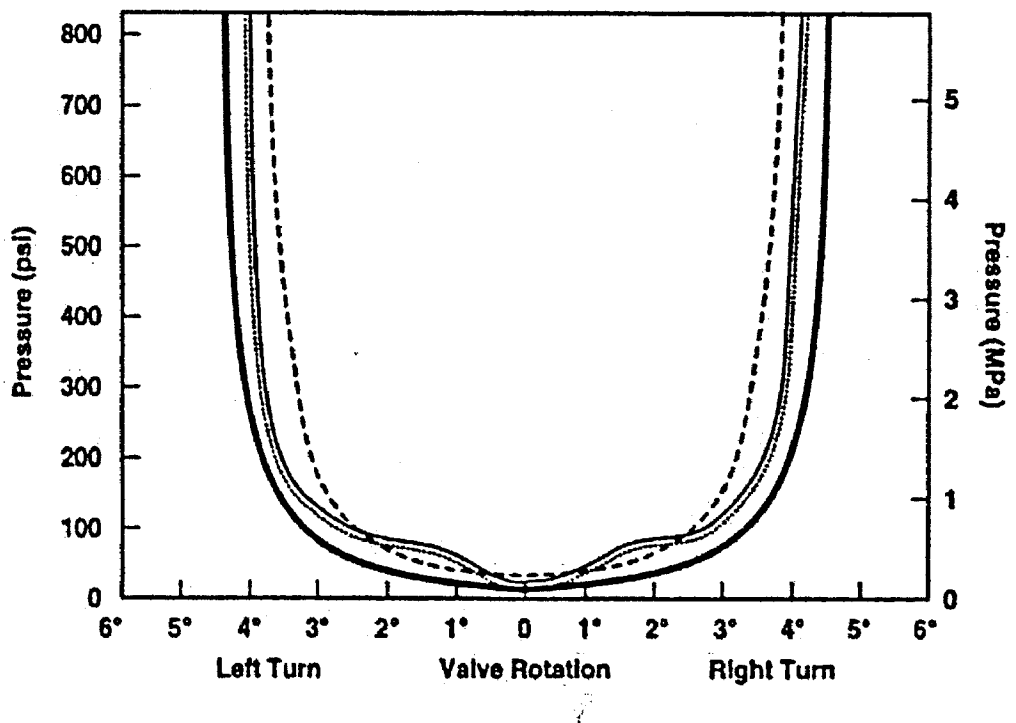

Figure 2.6 Rotary spool valve operating characteristics [Delphi (2004)]

2.1.3 Hydraulic power cylinder

Figure 2.7 [Delphi (2004)] shows the function of the hydraulic power cylinder (or called actuator cylinder) in a hydraulic steering system. The control valve assigns the high pressure fluid to the left side or the right side of the actuator cylinder and at the same time discharges the low pressure fluid from the other side of the cylinder. As the steering assistant force, the pressure difference between the two sides of the cylinder helps the piston to push the rack and reduce the driver's steering torque.

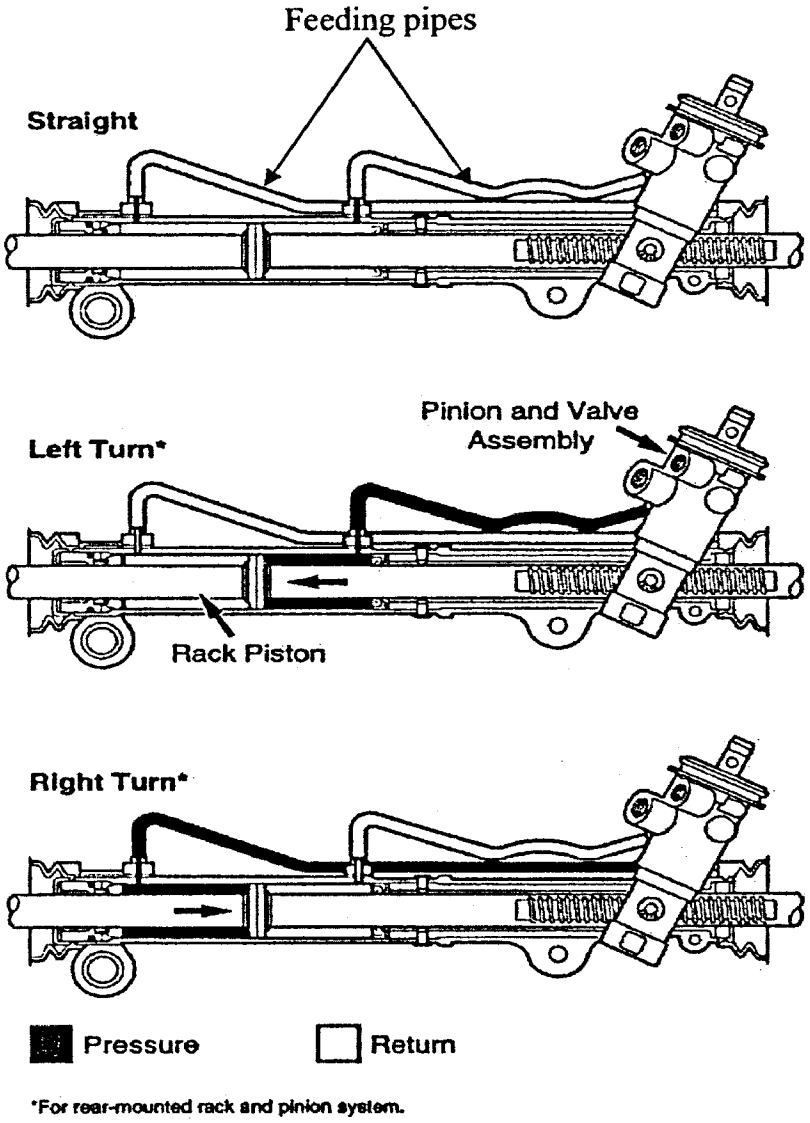

Fig. 2.7 Function of the hydraulic power cylinder [Delphi (2004)]

2.1.4 Steering pump

Steering pump supplies high pressure fluid to the hydraulic power steering system. Vane pumps are widely used in the steering system, and they can provide an approximately constant flow rate to the system within the engine working speed range. Figure 2.8 shows the components of a typical vane steering pump [Website 2]. The main components include the rotor, the pressure plate, the ring and the vanes. The characteristics of the steering pump will be discussed in the context of system modelling which is shown in Chapter 3.

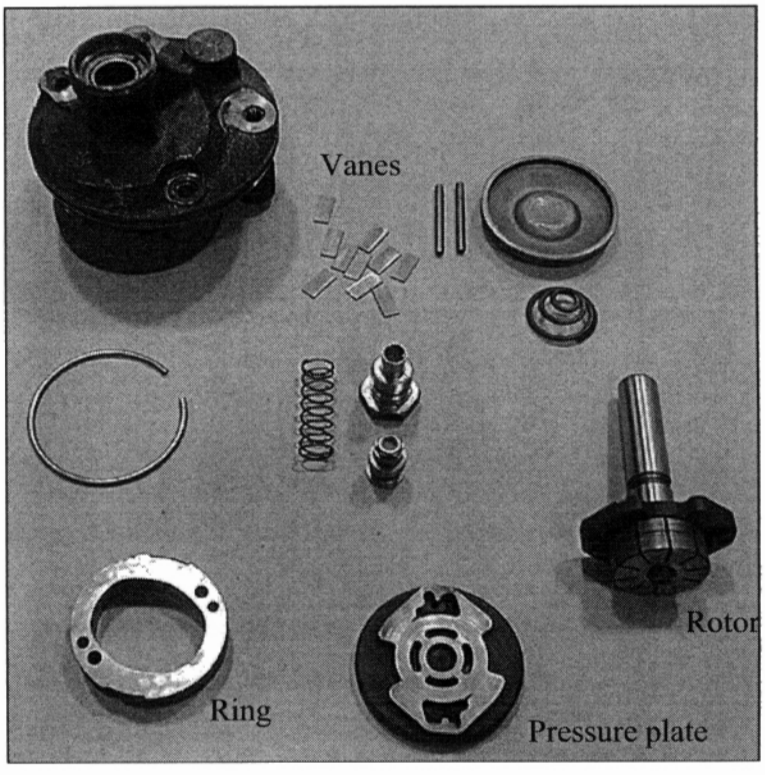

Figure 2.8 Power steering pump components [Website 2].

2.2 Vibration phenomena in hydraulic power steering systems

A hydraulic power steering system consists of hydraulic and mechanical components with a wide variety of characteristics. The interactions of those components, as well as the effects of the engine speed, front suspension and tyres, induce the vibration and noise of steering systems. While the steering system noise, vibration and harshness (NVH) have been noticed for a long time and many problems have been discovered and analysed, the terminology in this field is not clear and some of the phenomena with different names overlap each other. The main reason for this is that many researchers investigated the steering system NVH problems individually with different methods and techniques, and the communications between these investigations are limited due to the consideration of the commercial confidentiality. In this chapter, a wide range of vibration and noise problems, as well as the analysis methods and solutions, are reviewed, discussed and classified with the effort of establishing a clear view of steering system NVH.

Four main phenomena of steering system noise, vibration, and harshness (NVH) were listed and briefly introduced by Wong (2001).

"*Steering Shudder; resulting from the excitation of the fundamental frequency at the frame support by a fluid periodic flow force caused by the engine-driven vane pump.*

"*Steering wheel nibble; resulting from the excitation of the fundamental frequency of the rack and pinion gear mechanism by a periodic rack force induced by brake disk roughness, during braking at highway speeds.*

"*Mechanical front-end noise; resulting from the dynamic interaction between the rack and steering gear housing, caused by tire shock and vibration loads generated by tires riding on the bumps, stones, and pot holes on the road during low speed driving.*

Steering wheel dither; caused by dynamic interaction between the steering gear and front suspension struts subjected to a periodic vertical tire load induced by a tire high spot at a certain highway speed."

A hydraulic power steering model and a four-wheel independent suspension model were developed to simulate the hydraulic power steering model performance and optimise the steering system design [Wong (2001)]. Two examples, which dealt with mechanical front-end noise and steering wheel dither respectively, were used to illustrate the simulation process.

Steering shudder was also observed at the frame support, the pipes and hoses when the steering wheel was turned from lock to lock at low or parking speeds. It was believed by the engineers in Tristar Steering and Suspension, Ltd. Australia that the shudder was caused by an instability in the hydraulic system, which was due to the rapid change of the boost rate, and a combination of other factors, including pump rotation, hose length and compliance, friction between the road and tyres, pump flow rate, etc.

Sahinkaya (1996) indicated that the steering vibration was caused by an interaction of the mechanical components and the periodic high pressure fluid of the steering system. Fluid pressure oscillations in the power cylinder were the main source of two well known vibration phenomena: steering shudder and steering shimmy. Steering shudder occurred when the vehicle was at parking speed, or even stationary and the shudder frequency was from 25 to 200 Hz. The valve and the flow rate oscillations, which were caused by the combination of nature flow rate in the power cylinder and the flow rate changes of pump, were the reasons of the steering shudder. Sahinkaya also argued that the frequency of steering shimmy was from 6 to 15 Hz. Steering shimmy source was also the power cylinder. It was due to the combination of the flow rates in power cylinder and power piston vibration caused by unbalanced tyre and braking forces. A steering vibration stabiliser named Rack And Pinion Stabilizer (RAPS) was designed to reduce the steering shudder and shimmy by Sahinkaya (1996). It consisted of a cylindrical steel housing with an accelerometer, isolation valves, solenoid valves, pressure sensor and a couple of hydraulic hoses. The two sides of the RAPS piston were subjected the same pressure difference as the power cylinder piston of the

steering system. The frequency of RAPS could be tuned to counter the frequency of the unbalanced hydraulic oscillation, so it could reduce the steering vibration caused by hydraulic pulsations.

In the analysis of Smith *et al* (1995) and Ferries *et al* (1997), a power steering system equipped with hydraulic and mechanical components was modelled as a feedback control system, and the steering shudder was analysed as a closed-loop oscillation caused by the interaction of the steering system and the vehicle structure. The load dynamics were included by using a dynamic compliance transfer function which was obtained empirically. Only frequency domain analysis was conducted and linear models were used in the analysis. Different combinations of parameters were tried by the analytical approach, and one of them increased the stability of the steering system. The hydraulic impedance element method was used by Ferries *et al* (1997) in this research.

Matsunaga (2001) addressed the self-excited vibration in hydraulic power steering systems and solved the problem by changing the position and length of the supply line in the system. A simplified mathematical model including the supply line, the cylinder lines, and power cylinder was established. The characteristics method, the vaporous cavities model and three element visco-elastic models were used to calculate the fluid flow in the pipelines. The numerical calculations and experimental results showed that the self-excited vibration occurred at the rack and the supply line, and the frequency of the vibration was about 143 Hz. In fact, the self-excited vibration is the pressure ripple in the steering system. Matsunaga's research mainly focused on the hydraulic components in the power steering system, and it did not include steering wheel, pinion and front wheels.

Phillips (2003) also focused on the self-excited vibration in hydraulic power steering systems, but presented a different opinion and solution to that of Matsunaga. In the paper, the asymmetry in the hydraulic system, including the different lengths of the two cylinder lines of the fluid column and the different volumes of the power cylinder during steering, was the main contributor to the vibration problem. Also, the high gain control valve was an important factor. A mathematical model developed in this paper

consisted of cylinder lines, power cylinder and control valve, and solutions derived from the model included changing the geometry of the cyliner lines and power cylinder, as well as increasing the pipe flow resistance. Some components of the hydraulic power steering system, such as the steering wheel, steering column, steering pump and supply line, were absent in this research, and the coupling between the mechanical and hydraulic components were not investigated.

Steering wheel nibble, the rotational vibration of the steering wheel, was described and investigated by Neureder (2002), and four disturbance factors were found to be the causes: imbalance of the road wheel, the tyre non-uniformity, the run-out of the road wheel and the brake torque variation during braking. Models of the suspension and steering systems were developed and the sensitivities of the suspension and steering parameters were also analysed in the paper.

According to the research of Sciortino and Bamdad-Soofi (1997), the steering system noise or "squawk" could arise when the steering wheel angle suddenly changed during a parking maneuver. This phenomenon is attributed to the hydraulic fluid pressure interaction with the torsional resonance of the torsional bar at a low fluid viscosity during pressure drop, and the low-pressure cylinder lines was identified as the noise source. The transient frequency of squawk was at 125 Hz and the relevant harmonics are about 500 Hz. The solutions of steering system squawk included choosing a proper flat-angle for the valve profiles and decreasing the pressure differential in the low-pressure return line. The research was mainly dependent on experimental approaches, and no mathematical models were established.

Long (1999) mentioned the rattle noise in the rack and pinion power steering system which was approximately 20 Hz. The noise was due to the hydraulic pressure pulse in the return line. A "standpipe" installed on the return line of the hydraulic power steering system was used to isolate hydraulic noise from mechanical noise and to reduce the hydraulic rattle. The standpipe was typically a 250mm length of rubber hose which contained a column of air to damp the pressure pulse of the return line.

Smid *et al.* (1998) discussed the pressure and flow fluctuations of steering pumps and investigated the noise and vibration generated by the pressure ripple and flow pulsation through the fluid lines. The simplified power steering model represented the upstream components of the system, and it consisted of the pump, two pipes and one hose. The rack-and-pinion was modelled as a "point impedance" and the rotary spool valve, power cylinder and return lines were neglected. Frequency domain analysis was used in the simulation and the results of simulation showed that the vibration was attenuated effectively when the hose length at 1/4 of the pressure ripple wavelength.

An unconventional idea to reduce pressure ripple in power steering systems was raised by Kumar *et al.* (1999). By this measure, active and broadband piezoelectric actuators were used in hydraulic circuits of power steering systems to dampen the ripple.

Summarising the literature review, Table 2.1 groups the vibration and noise problems of the steering systems, especially the hydraulic power steering systems. Listed are the main reasons, the situations when certain problems happen, the frequency ranges and the solutions. In this table, the steering shudder and the pressure ripple are the most significant problems of the hydraulic power steering. Therefore, the steering shudder and the pressure ripple problems are the focus of this study which aims to investigate the dynamic characteristics of the steering system, and the interaction of the mechanical components and the hydraulic components of the steering system is emphasised in the research.

Table 2.1 Steering system vibration and noise phenomena

Vibration problem	**Reasons or sources of the excitation**	**Situation**	**Frequency**	**Solution**
Steering shimmy	flow rate oscillations in power cylinder	Driving speed	6-15 Hz	Rack And Pinion Stabilizer
Steering shudder (including rattle, hose vibration and noise)	• fluid periodic flow force caused by vane pump • flow rate oscillations in power cylinder • rotary spool valve • rack and pinion • return line (hose) • vibration of the whole hydraulic system • asymmetrical feature of the system	Parking speed, Stationary vehicle, ramp steering input	20-50 Hz	• Rack And Pinion Stabiliser • Tuning parameters • Standpipe • Changing position and length of supply line • Modifying the asymmetrical design • Turning other parameters
Pressure ripple (including self-excited vibration)	• supply line	Parking speed	100-200 Hz	Tuning other parameters
Squawk	• vibration of the whole hydraulic system • rotary spool valve • return pipe (feed line)	Parking speed	125-500 Hz	Tuning parameters
Mechanical front-end noise	Rack, steering gear housing vibration caused by tyre shock	Low speed driving		
Steering wheel nibble	• Unbalance of the road wheels and tyres • Brake torque variation	Driving speed		Tuning parameters
Steering wheel dither	Dynamic interaction between steering gear and front suspension strut	Highway speed		

2.3 Methods, techniques and models used in the investigation of steering system dynamics

2.3.1 Analytical methods of steering systems

Researchers have adopted and developed many analytical methods to investigate the noise and vibration of steering systems. Adams and Topping (2001) introduced the Steering Characterising Functions (SCFs), to describe the mechanical properties of steering systems. The SCFs included the kinematic function, stiffness function, effort function and hysteresis function. The concept of this method was to get the functional relationships relating input shaft displacement, rack displacement, rack force, and so on. These relationships were represented as a set of performance maps which were obtained by testing. The SCFs supplied some important functions, such as the steering torque gradient (lateral acceleration of vehicle versus steering wheel torque) and they could be used to describe and optimise the steering feel performance of a vehicle. However, the SCFs could not represent the characteristics of the hydraulic circuit and could not be used to investigate the noise and vibration problems of the hydraulic steering system.

The Bond Graph technique was used by Vijayakumar and Barak (2002) to analyse the kinematics and dynamics of a steering system without assisting force. But the Bond Graph was not adopted in this research because of its limits in the transient analysis of the hydraulic components.

CAE (Computer Aided Engineering) methods and the multi-body dynamics software, ADAMS/Car, were applied to investigate the influence of steering and suspension design parameters by Kim *et al.* (2002). In conclusion, steering wheel inertia, pressure area of the hydraulic power cylinder, caster trail and rear torsion beam axle were the important variables for the power steering system's effect on vehicle dynamics.

Takeuchi and Adachi (1995) believed that the bending vibrations of the pump, hoses, control valve, power cylinder and steering column were the main factors of the noise created by hydraulic power steering systems. In the paper, experimental methods, analytical method and Stiffness Optimisation Analysis (SOA) were used to reduce the

power steering noise. The analytical model incorporated 12 masses, 16 springs, 16 dampers and 72 degrees of freedom. The characteristic parameters of the model were identified by experimental processes.

2.3.2. Mathematical models of steering systems

With the rapid growth of low cost and high performance computers, mathematical modelling and computer simulation are widely adopted in the analysis of steering systems and become efficient tools of understanding the vibration issues and improving the systems' performance. A number of power steering system models have been reported in the literature. In a study of the steering torque, a mathematical model including steering and suspension systems was developed by Sharp and Granger (2003). It was concluded that five main factors affected the steering torque at parking speeding. They were tyre-to-road friction force, steering mechanism frictional forces, tyre carcass flexibility, body lifting effect and Hooke joint angle.

Taheri *et al.* (1998) established a ten degree-of-freedom (DOF) model of a rack and pinion steering system without assistant force, and the mechanism of the steering system, a nonlinear tyre model and a suspension model were included.

A hydraulic power steering system equipped with an unconventional control valve (OSPF) was analysed by Andersen *et al.* (2003), and a simplified front wheel model was introduced in the analysis. Ramp inputs of the steering wheel under variable load conditions were conducted to verify the model. Also, the model system stability and parameter sensitivity were investigated.

A model of a rack and pinion steering system was developed by Neureder (2002). The model consisted of steering wheel, the torsion bar, rack-and-pinion gear, the gear housing and the spring/damper elements. The power assist system was represented by a static boost curve, and the hydraulic damping was also taken into account.

A steering system model with the boost torque applied on the steering gear was established by Post and Law (1996). Three equations of motion were used to describe the power steering system.

Lozia and Zardecki (2002) introduced two novel functions, "luz" and "tar" to describe the nonlinear characteristics in the steering systems. The freeplay and dry friction were emphasised in the analysis.

It was noticed that, besides the study of the noise and vibration of steering systems, numerous books and papers were published to discuss the effects of steering systems on vehicle dynamics. Both of the constant ratio [Gillespie (1992) and Milliken (1995)] and variable ratio steering systems [Heathershaw (2000 and 2004)] were researched to improve vehicle handling. However, as the dynamic characteristics of the steering system *itself* were the concerns of this research, the influences of the steering system on vehicle dynamics are not discussed here.

2.3.3 Methods for hydraulic dynamics of steering systems

The theories of hydraulics and fluid dynamics, especially fluid transient, are reviewed and compared in the beginning of this study. The theories includes the method of characteristics [Wylie and Streeter (1993)], the impedance method [Wylie and Streeter (1993)], the different distributed parameter models for fluid transmission lines [Stecki and Davis (1986)] and the fluid-structure interaction in pipes systems [Tijsseling (1996) and Yang *et al.* (2004)]. Some of those theories and methods were adopted in the research of the hydraulic power steering system. Smid *et al* (1998) applied the impedance method and the transfer matrix method to discuss the noise and vibration generated by the pressure ripple and flow pulsation through the fluid lines. The ISO standards [ISO (1996)] recommended the impedance method in the determination of pressure ripples levels generated in systems and components. The noise characteristics and the impedances of some individual components in the hydraulic power steering system, such as the pump and steering gear, were measured and reported by Drew *et al.* (1994) and Qatu *et al.* (2000). In the study of the hydraulic steering system, Chen (2001) considered the fluid structure interaction by adopting four groups of first-order

differential equations and developing a 14×14 matrix for each section of the steering transmission line.

2.3.4 Summary

Based on the previous review, Table 2.2 listed the potential methods for the steering system analysis.

Table 2.2 Methods for steering system analysis

Method/model for mechanical subsystem	**Method for hydraulic subsystem**
• Multiple DOF system model	
• Steering Characterizing Functions (SCFs)	• Impedance method and transfer matrix method
• Bond Graph	• Characteristics method
• Multi-body dynamics software	• Fluid-structure interaction method
• Bending vibration analysis	

2.4 Theories and methods used in this thesis

In this research, multiple degree-of-freedom system model is used to analyse the mechanical subsystem of the steering system; and the impedance method and transfer matrix method are used to model the hydraulic subsystem. This choice is based on the merits of these methods in theoretical analysis of the hydraulic steering systems.

The steering shudder is related to many components of the steering system, so the proposed method should show the dynamic responses of the components individually. A more important requirement of this research is that the mechanical subsystem model could be easily coupled with the hydraulic subsystem to reveal the coupling of the steering system. A multi-DOF steering system model could provide a general tool to simulate the responses of different components, and the sensitivity analysis of some key system parameters could be carried out.

In the following chapters, the mechanical subsystem is modelled as a multi-DOF system with lumped masses connected by springs and dampers. The free vibration analysis of the mechanical subsystem is dealt with as an eigenvalue and eigenvetor problem. In the time domain simulation, numerical method is used. In the numerical calculation process, the second order differential equations of the system, $\ddot{x} = F(t, x, \dot{x})$, are transferred to the first order differential equations, $\dot{u} = f(t, u)$. After setting the initial values of the system, the fourth-order Runge-Kutta method is used to solve the equations step by step. The numerical method is efficient and accurate, but for this research more important advantage of the method is that it can handle the time-variable parameters of the system, such as the opening area of the spool valve and the gear ratio of the variable ratio steering system. By substituting the different values of these parameters into every step of the calculation, the system matrix is updated and the satisfying solution is obtained.

In this research, the hydraulic components of the steering system are analysed by the one dimensional impedance method because the pressure fluctuations in the system are the most important effects on the steering shudder. The transfer matrix method is also adopted because it is suitable to the serially connected transmission lines of the steering system. Furthermore, the hydraulic subsystem model developed by these two

methods can easily be coupled with the mechanical model, and the advantage of the frequency-dependent model is clearly shown in the frequency domain analysis of the coupled steering system.

The impedance method [McCloy and Martin (1980)] is adopted in the analysis of the steering hydraulic circuit in this research and is briefly introduced below.

In this method, the general relationship of the pressure, the fluid impedance and the flow rate is:

$$\text{Pressure} = \text{hydraulic impedance} \times \text{flow rate}$$

$$P = Z_h \times Q \tag{2.1}$$

The fluid impedances of a fluid system include three effects which are fluid resistance, fluid inductance and fluid capacitance. Because of the strong similarity between electrical circuits and linear hydraulic circuits, the electrical analogues are employed to illustrate the hydraulic impedances.

The fluid resistance can be represented and calculated by the following symbol and formula,

$$R_h = \frac{128\mu L}{\pi d^4} \tag{2.2}$$

where μ is the dynamic viscosity, L is the length of the pipe or hose, and d is the inner diameter of the pipe or hose.

The fluid inductance can be represented and calculated by the following symbol and formula,

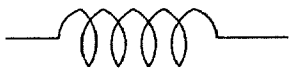

$$L_h = \frac{\rho L}{A} \tag{2.3}$$

where ρ is the density of the fluid, L is the length of the pipe or hose and A is the inner area of the pipe or hose.

Fluid capacitance can be represented and calculated by the following symbol and formula,

$$C_h = \frac{AL}{\beta_e} \tag{2.4}$$

where A is the inner area of the pipe or hose, L is the length of the pipe or hose and β_e is the equivalent bulk modulus.

Fig 2.9 shows an impedance model of a hydraulic pipe element, where Q_u and P_u are the inlet flow rate and pressure respectively, and Q_d and P_d are the outlet flow rate and pressure.

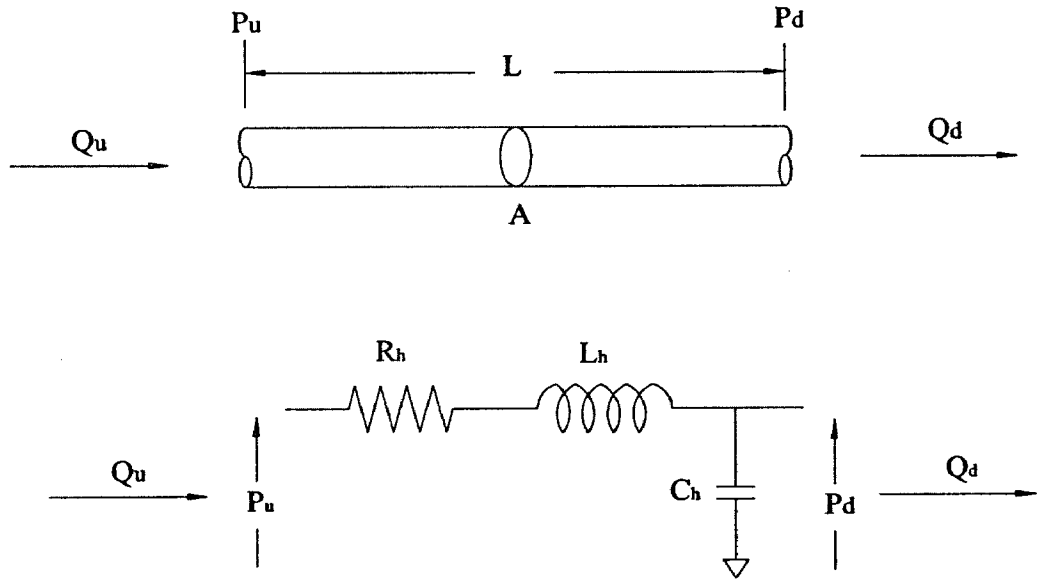

Figure 2.9 Impedance model of a pipe line

There are two models to deal with the hydraulic pipe lines: the lumped parameter model and the distributed parameter model. In the lumped parameter model, the pipe filled with oil is simplified as a single lump and the impedance of the pipe is

$$Z_h = \frac{P_d}{P_u} = \frac{1}{L_h C_h s^2 + R_h C_h s + 1}. \tag{2.5}$$

where, $s = j\omega$.

In this research, the pressure oscillations and flow ripples are investigated by the distributed parameter model which is more accurate than the lumped parameter model in high frequency ranges. The impedance of the pipe in Figure 2.9 can be described by the transfer matrix:

$$\begin{bmatrix} \hat{P}(l) \\ \hat{Q}(l) \end{bmatrix} = [T] \begin{bmatrix} \hat{P}(0) \\ \hat{Q}(0) \end{bmatrix} \tag{2.6}$$

where $\begin{bmatrix} \hat{P}(l) \\ \hat{Q}(l) \end{bmatrix}$ and $\begin{bmatrix} \hat{P}(0) \\ \hat{Q}(0) \end{bmatrix}$ are the ripples of the outlet pressure, flow rate and the inlet pressure, flow rate respectively. The transfer matrix $[T]$ is

$$T = \begin{bmatrix} \cosh(\gamma l) & -Z_c \sinh(\gamma l) \\ -\dfrac{\sinh(\gamma l)}{Z_c} & \cosh(\gamma l) \end{bmatrix} \tag{2.7}$$

where $\gamma = \sqrt{C_h j\omega (L_h j\omega + R_h)}$, $Z_c = \dfrac{\beta_e \gamma}{A \cdot j\omega}$, ω is the frequency and $j = \sqrt{-1}$. The parameters R_h, C_h and L_h in $[T]$ are calculated by Equations (2.2) to (2.4).

Based on the impedance method, other fluid circuit elements, such as branches and valves, can also be represented by their transfer matricies. The details will be explained in the following chapters.

In summary, the combination of the lumped mass multi-DOF model for mechanical components and the distributed parameter impedance model for hydraulic components are the main measures of this research to study vibration problems of hydraulic power steering systems both in the time domain and in the frequency domain.

CHAPTER 3 HYDRAULIC POWER STEERING SYSTEM MODEL

3.1 Introduction

A comprehensive mathematical model of a typical hydraulic power rack and pinion steering system is developed in this chapter, and the dynamic characteristics of the steering system are analysed. The mechanical components, the hydraulic supply lines and the rotary spool valve of a hydraulic power steering system are included in the model.

In this chapter, the mechanical parts of the system are developed as lumped masses interconnected with springs and dampers. The natural frequencies and modes shapes of the mechanical components are obtained by the eigenvalue and eigenvector calculation of the system matrix. By integrating the power cylinder, pump and hoses, a hydraulic circuit model is established where these hydraulic parts are presented as hydraulic impedance elements, and the rotary spool valve, the key part of the system, is modelled as a four-way open centre spool valve. The mathematical model is analysed numerically to obtain the responses of the system in time domain.

As shown in Figure 2.1, the dynamic components of a typical hydraulic power steering system mainly include steering wheel, input shaft, rotary spool valve, rack and pinion, pump, hydraulic cylinder, hydraulic hoses, tie rod linkage, front wheels and tyres.

A schematic of a power steering system is shown in Figure 3.1. The integrated hydraulic power steering system model consists of two subsystems: the mechanical subsystem and the hydraulic subsystem. The mechanical subsystem includes the mechanical components of the steering system and two front wheels, and the hydraulic subsystem included the pump, the hydraulic supply line, the cylinder/piston unit and the rotary spool valve.

The two subsystems are discussed in the following sections separately, and then they are combined in the integrated model by the coupling elements between the two subsystems. The torsional bar in the mechanical subsystem is coupled with the rotary spool valve in the hydraulic subsystem because the twist angle of the torsional bar

determines the opening areas of the orifice of the valve. The rack and pinion gear in the mechanical subsystem is coupled with the cylinder/piston unit in the hydraulic subsystem as the piston is fixed on the rack.

The main boundaries of the system model include the steering wheel, the tyres and the steering pump. The input torque on the steering wheel and the friction forces from the tyres are considered the boundary conditions of the mechanical subsystem and the pressure fluctuation of the pump is the boundary condition of the hydraulic subsystem.

3.2 Mechanical subsystem

As shown in Figure 3.1, the steering column and torsional bar are modelled as springs and dampers, and the stiffness of pinion meshed with the rack and the stiffness of the tie rods are taken account of as well. The twist angle of torsional bar controls the spool valve and this is the key connection between the mechanical and hydraulic subsystems. The translational forces of tie rods produce the rotational torque through the steering arms and steer two front wheels. In this model, not only the rotational degrees of freedom of the front wheels are introduced but the translational movements of front wheels are considered. The translational displacement of the front part of the vehicle body transfers the vibration from the hydraulic cylinder to the tyres through the left and right front suspensions. A simplified tyre model is used, which included both the torsional and lateral stiffness of the tyres.

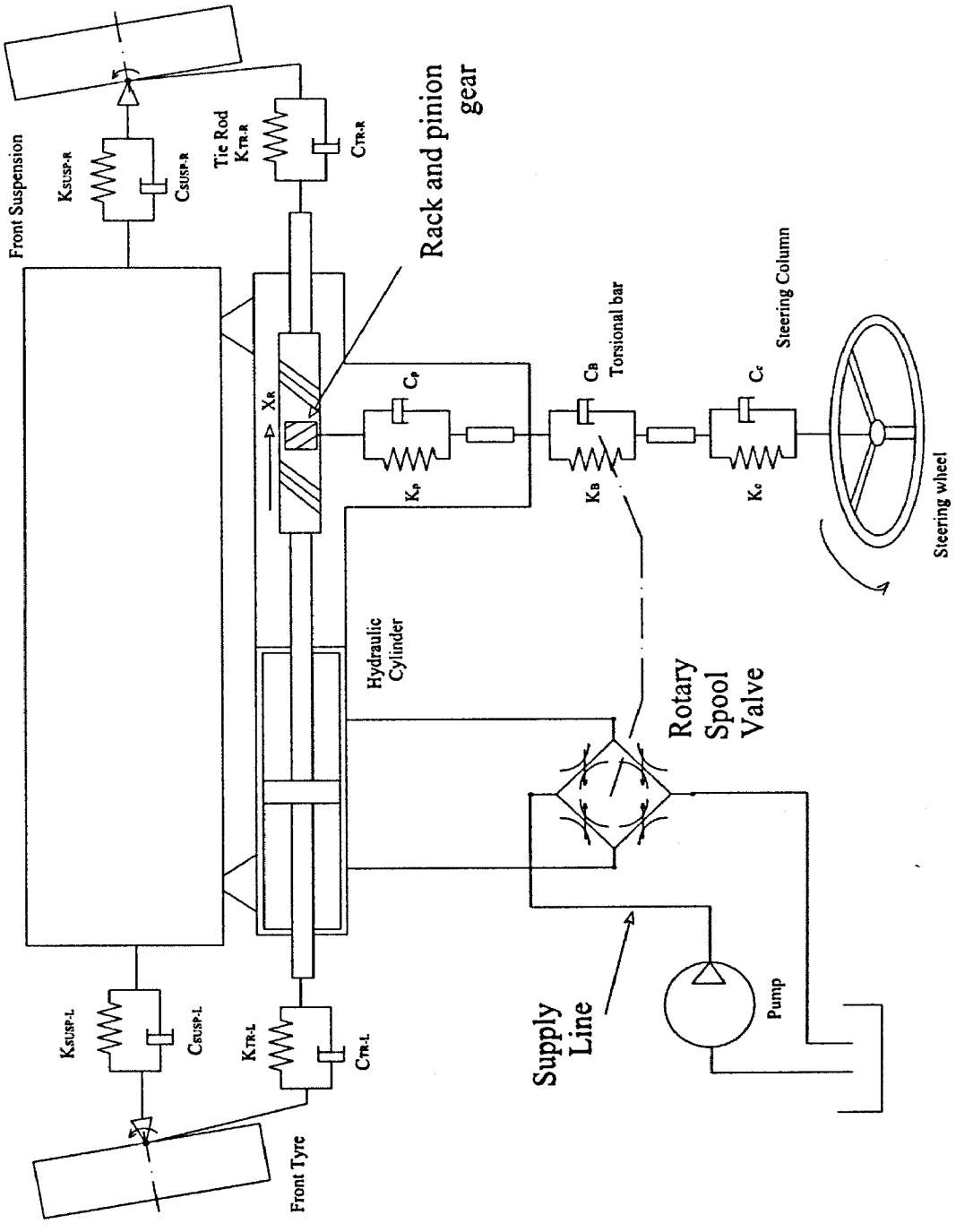

Figure 3.1 Schematic of steering system model, including the connection with front suspensions

Besides the stiffness and damping, the friction forces also greatly affect the dynamic characteristics of the system. The non-linear friction forces in this model include the friction on the steering column, the friction of the kingpins, the friction between pinion and rack, the friction between piston and hydraulic cylinder, and the friction between tyres and the ground. In the numerical analysis, the nonlinear friction forces are represented as hyperbolic tangent functions to reduce the "stiffness" of the calculation. This technique is introduced by Sharp and Granger (2003) in the study of steering torques at parking speeds. The approximate friction model is necessary, because exact dry friction force model, $F = -F_0 \operatorname{sgn}(v)$, brings numerical difficulties in analysis of some "stiff" systems, such as hydraulic steering system.

Figure 3.2 shows the friction force of the rack. The solid line represents the original form of the friction force. The dashed line represents the friction force used in the numerical calculation and it is determined by the following equation,

$$F = -F_0 \times \tanh(\beta \cdot v)$$

where, F is the friction force against the velocity of the rack, F_0 is the amplitude of the original friction force, the coefficient β determines the stiffness of the curve and it is 1000 in this plot and v is the speed of the rack.

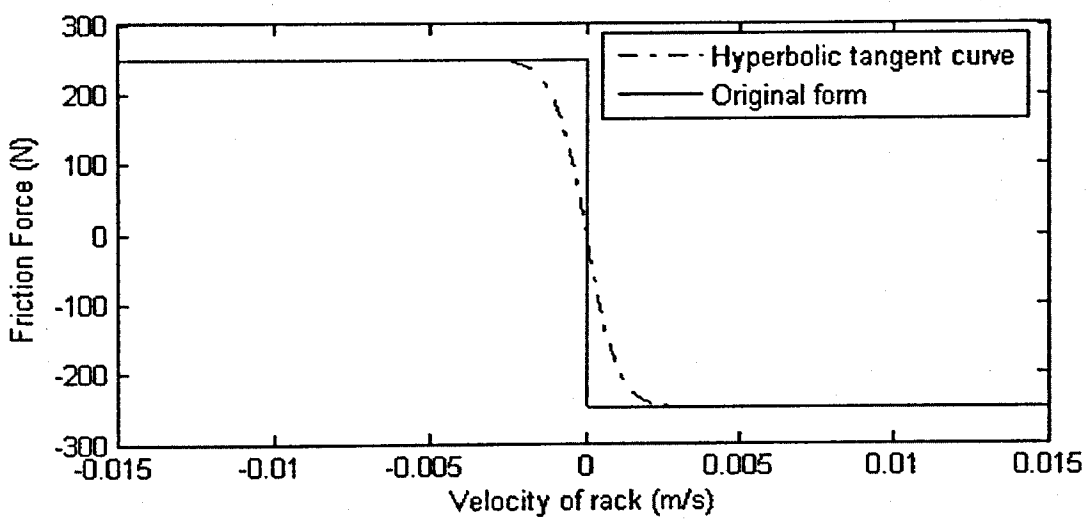

Figure 3.2 Representation of friction force in numerical calculation

The equations for the multi-DOF mechanical subsystem are obtained using the free body diagrams of the mechanical components.

The equation for the steering wheel rotation is

$$I_{SW}\ddot{\theta}_{SW} = T_{SW} - (\dot{\theta}_{SW} - \dot{\theta}_C)C_C - (\theta_{SW} - \theta_C)K_C \tag{3.1}$$

The equation for the steering column rotation is

$$I_C\ddot{\theta}_C = -T_{FR-C} + (\dot{\theta}_{SW} - \dot{\theta}_C)C_C + (\theta_{SW} - \theta_C)K_C - (\dot{\theta}_C - \dot{\theta}_P)C_B - (\theta_C - \theta_P)K_B . \tag{3.2}$$

It is believed that the stiffness of the pinion, meshed with the rack, is one of the main compliances of the mechanical components in a steering system [Baxter (1998)]. The left part of Figure 3.3 shows the stiffness and damping of the rack and pinion gear, and the right part shows the equivalent model developed here for the gear.

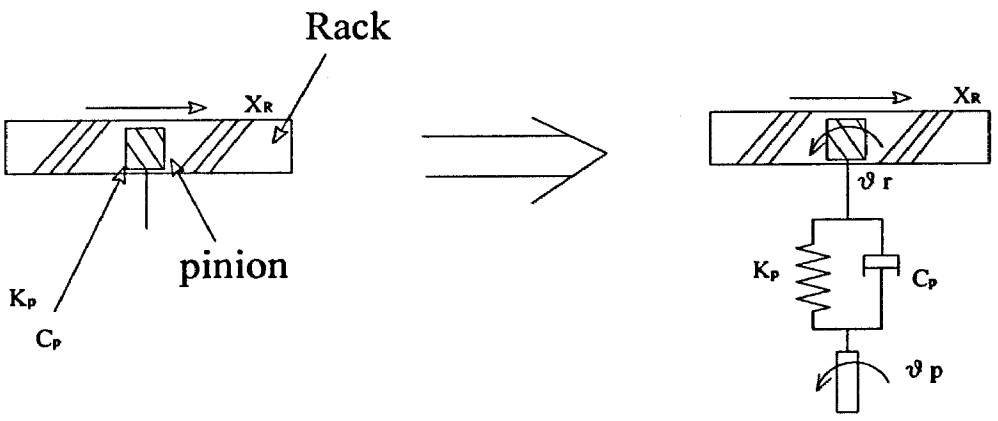

Figure 3.3 Equivalent model of rack and pinion gear

By using the equivalent model, the stiffness and damping coefficient is included in the system. The rotational DOF of the pinion is θ_P and it is connected with a rotational DOF, θ_r, by the stiffness and damping. The θ_r is not an independent DOF. It is rigidly connected with the rack and the relationship can be written as

$$\theta_r = \frac{x_R}{N}$$

where, x_R is the lateral displacement of the rack and N is the ratio between the rack and pinion.

Then, the dynamic equation for the pinion rotation is

$$I_p\ddot{\theta}_p = (\dot{\theta}_C - \dot{\theta}_P)C_B + (\theta_C - \theta_P)K_B - (\dot{\theta}_P - \dot{x}_R / N)C_P - (\theta_P - x_R / N)K_P. \tag{3.3}$$

The equation for the hydraulic cylinder displacement is

$$(m_P + m_H)\ddot{x}_H = -F_B - (\dot{x}_H - \dot{x}_V)C_V - (x_H - x_V)K_V + F_{FR-H}. \tag{3.4}$$

The schematic of the rack and the cylinder/piston unit is shown in Figure 3.4. Since the rack is fixed with the hydraulic piston, the forces applied on the rack include the force from the pinion, the hydraulic boost force, the friction force and the forces from the two tie rods. The boost force is one of the main concerns in the steering system vibration study. In simulation, the boost force is generated by the spool valve model which will be discussed in the next section. The dynamic equation of the rack can be written as,

$$\begin{aligned} m_R\ddot{x}_R = {} & \frac{(\dot{\theta}_P - \dot{x}_R / N)C_P + (\theta_P - x_R / N)K_P}{N} + F_B - F_{FR-H} \\ & - (\dot{x}_R - \dot{x}_{TR-L})C_{TR-L} - (x_R - x_{TR-L})K_{TR-L} - (\dot{x}_R - \dot{x}_{TR-R})C_{TR-R} - (x_R - x_{TR-R})K_{TR-R} \end{aligned} \tag{3.5}$$

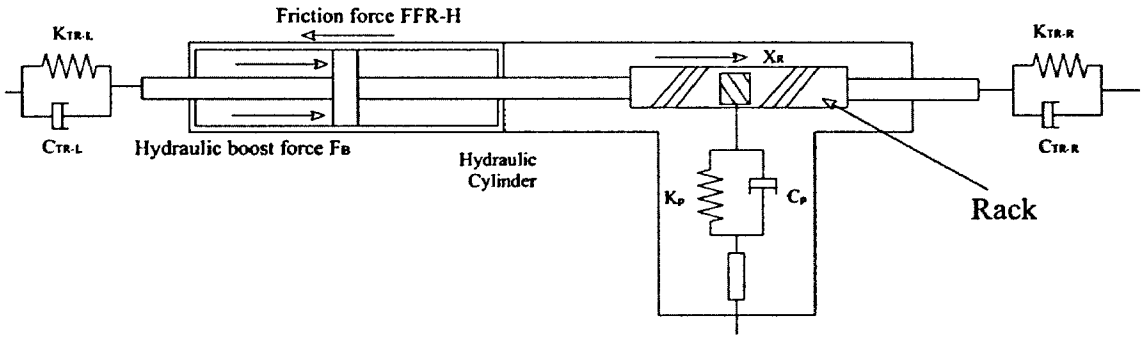

Figure 3.4 Schematic of the rack and the cylinder/piston unit

In the modelling of the front suspension and tyres, the complexity of the systems is noticed. The geometrical parameters of the front suspensions include the kingpin inclination, the camber angle, the toe in/out, the caster, the scrub radius, and etc. The details of the friction force of the tyres on the ground are also complicated [Pacejka (2002)]. These specifications greatly affect the vehicle dynamics as well as the tyres' wearing off. However, for the dynamic characteristics study of hydraulic power steering systems, the friction force between the tyres and the ground have much more significant effect on the steering system than other front suspension parameters, and the friction force can be simplified to a Coulomb friction force [Sharp (2003)].

The tie rods, steering arms, wheels and tyres are simplified in the mathematical models and shown in Figure 3.5. The steering arm transfers the translational displacement of the tie rod to the rotational displacement of the wheel and tyre. The tyre rotates around the centre of the tyre/ground contact patch.

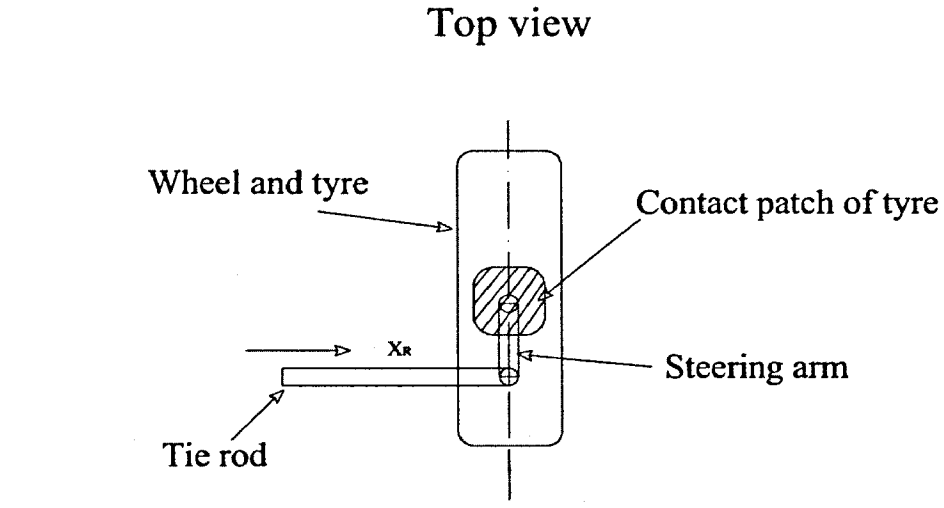

Figure 3.5 Simplified model of the tie rod, steering arm and tyre

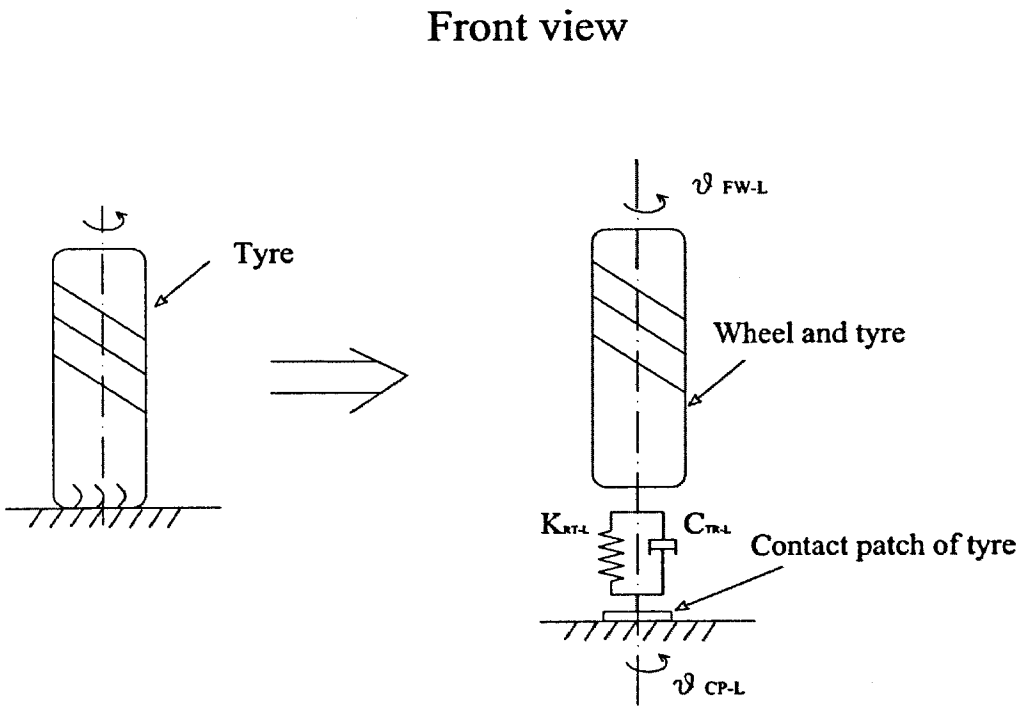

Figure 3.6 Model of wheel and tyre

Figure 3.6 shows a simplified tyre model. In this model, the contact patch of the tyre have one DOF, θ_{CP-L}. The other part of the wheel and tyre are considered as a rigid body and has another DOF, θ_{FW-L}. The rotational stiffness and damping of the tyre connect the contact patch and the rigid wheel. Therefore, the friction force from the ground is applied on the contact patch, and the force affects the system through the stiffness and damping of the tyre. In the numerical simulation, the method shown in Figure 3.1 is used to calculate the friction force from ground.

With the simplified models of front suspensions and tyres, the dynamic equations of other components of the steering system can be obtained by the free body diagram analysis. The equations are shown below.

The equation for the rotary motion of the left front wheel (road wheel) is

$$I_{FW}\ddot{\theta}_{FW-L} = l[(\dot{x}_R - \dot{x}_{TR-L})C_{TR-L} + (x_R - x_{TR-L})K_{RT-L}] - (\dot{\theta}_{FW-L} - \dot{\theta}_{CP-L})C_{TIRE-ROTARY} - (\theta_{FW-L} - \theta_{CP-L})K_{TIRE-ROTARY} - T_{FR-K} \quad (3.6)$$

where, $\frac{x_{TR-L}}{l} = \theta_{FW-L}$.

The equation for the rotary motion of the right front wheel (road wheel) is

$$I_{FW}\ddot{\theta}_{FW-R} = l[(\dot{x}_R - \dot{x}_{TR-R})C_{TR-R} + (x_R - x_{TR-R})K_{RT-R}] - (\dot{\theta}_{FW-R} - \dot{\theta}_{CP-R})C_{TIRE-ROTARY} - (\theta_{FW-R} - \theta_{CP-R})K_{TIRE-ROTARY} - T_{FR-K} \quad (3.7)$$

where, $\frac{x_{TR-R}}{l} = \theta_{FW-R}$.

The equation for the translational motion of the left front wheel (road wheel) is

$$m_{TIRE}\ddot{x}_{FW-L} = (\dot{x}_V - \dot{x}_{FW-L})C_{SUSP-L} + (x_V - x_{FW-L})K_{SUSP-L} - \dot{x}_{FW-L}C_{TIRE-LATERAL} - x_{FW-L}K_{TIRE-LATERAL} \quad (3.8)$$

The equation for the translational motion of the right front wheel (road wheel) is

$$m_{TIRE}\ddot{x}_{FW-R} = (\dot{x}_V - \dot{x}_{FW-R})C_{SUSP-R} + (x_V - x_{FW-R})K_{SUSP-R} - \dot{x}_{FW-R}C_{TIRE-LATERAL} - x_{FW-R}K_{TIRE-LATERAL} \quad (3.9)$$

The equation for the front half body of vehicle is

$$m_V\ddot{x}_V = (\dot{x}_H - \dot{x}_V)C_V + (x_H - x_V)K_V - (\dot{x}_V - \dot{x}_{FW-L})C_{SUSP-L} - (x_V - x_{FW-L})K_{SUSP-L} - (\dot{x}_V - \dot{x}_{FW-R})C_{SUSP-R} - (x_V - x_{FW-R})K_{SUSP-R} \quad (3.10)$$

The equation for the rotary motion of the contact patch of left tyre is

$$I_{CP}\ddot{\theta}_{CP-L} = -T_{FR-G} + (\dot{\theta}_{FW-L} - \dot{\theta}_{CP-L})C_{TIRE-ROTARY} + (\theta_{FW-L} - \theta_{CP-L})K_{TIRE-ROTARY} \quad (3.11)$$

The equation for the rotary motion of the contact patch of right tyre is

$$I_{CP}\ddot{\theta}_{CP-R} = -T_{FR-G} + (\dot{\theta}_{FW-R} - \dot{\theta}_{CP-R})C_{TIRE-ROTARY} + (\theta_{FW-R} - \theta_{CP-R})K_{TIRE-ROTARY} \quad (3.12)$$

Therefore, a 12-DOF system representing the mechanical subsystem can be derived from Equations (3.1) to (3.12) and written in the following form.

$$[I(M)]_{12\times12}\left[\ddot{\theta}(\ddot{x})\right]_{12\times1} + [C]_{12\times12}\left[\dot{\theta}(\dot{x})\right]_{12\times1} + [K]_{12\times12}[\theta(x)]_{12\times1} = [T(F)]_{12\times1} \quad (3.13)$$

where, θ and x are the rotational and translational displacements, I and M denote the moments of inertia and masses of the elements, respectively. C and K represent the damping and stiffness coefficient matrices, and T and F are the external torque and forces respectively. The mechanical ratios between pinion and rack, and between the translational displacement of tie rods and the rotational displacement of the steering arms are considered in the formulation. For example, in $[K]_{12\times12}$, several elements include N and l, such as "$K_P/N^2 + K_{TR-L} + K_{TR-R}$" and "$-l \cdot K_{TR-L}$", where N is the ratio of rack and pinion gear and l is the distance between the centre of the front wheel and the tie rod end. The l transfers the translational displacement of tie rod to the

rotational displacement of the steering arm. A constant ratio rack and pinion gear is analysed in the model, thus N is a constant in the simulation. The details of the stiffness matrix $[K]_{12\times12}$ are shown in Table 3.1. The 12 DOF model covers all the important mechanical components in a typical hydraulic power steering system. Less number of DOF model could neglect some components. More number of DOF model could not only increase calculation load but also lose the focuses on the important components.

The stiffness coefficients are supplied by the manufacturer of the steering systems. The system damping coefficients are assumed zero except the twist damping coefficient of the tyre is taken as 25 Nm/rad, adopted from tyre model for steering system reported by Sharp and Granger (2003). The frictional forces are important parameters in the dynamics of the system, and therefore the nonlinear frictional forces on the steering column, the kingpins, between pinion and rack, between piston and hydraulic cylinder, and between tyres and the ground are included.

Equation 3.13 can be written in a simplified form for further calculation,

$$[M]_{12\times12}[\ddot{u}]_{12\times1}+[C]_{12\times12}[\dot{u}]_{12\times1}+[K]_{12\times12}[u]_{12\times1}=[F]_{12\times1}. \tag{3.14}$$

Table 3.1 Stiffness matrix of the mechanical subsystem of the hydraulic power steering system

$$\begin{bmatrix}
K_C & -K_C & 0 & 0 & 0 & 0 & 0 & 0 & 0 & 0 & 0 & 0 \\
-K_C & K_C+K_B & -K_B & 0 & 0 & 0 & 0 & 0 & 0 & 0 & 0 & 0 \\
0 & -K_B & K_B+K_P & 0 & -\frac{K_P}{N} & 0 & 0 & 0 & 0 & 0 & 0 & 0 \\
0 & 0 & 0 & K_V & 0 & 0 & 0 & 0 & 0 & 0 & 0 & -K_V \\
0 & 0 & -\frac{K_P}{N} & 0 & \frac{K_P}{N^2}+K_{TR\text{-}L}+K_{TR\text{-}R} & -l\cdot K_{TR\text{-}L} & -l\cdot K_{TR\text{-}R} & 0 & 0 & 0 & 0 & 0 \\
0 & 0 & 0 & 0 & -l\cdot K_{TR\text{-}L} & l^2\cdot K_{TR\text{-}L}+K_{T\text{-}RO} & 0 & -K_{T\text{-}RO} & 0 & 0 & 0 & 0 \\
0 & 0 & 0 & 0 & -l\cdot K_{TR\text{-}R} & 0 & l^2\cdot K_{TR\text{-}R}+K_{T\text{-}RO} & 0 & -K_{T\text{-}RO} & 0 & 0 & 0 \\
0 & 0 & 0 & 0 & 0 & -K_{T\text{-}RO} & 0 & K_{T\text{-}RO} & 0 & 0 & 0 & 0 \\
0 & 0 & 0 & 0 & 0 & 0 & -K_{T\text{-}RO} & 0 & K_{T\text{-}RO} & 0 & 0 & 0 \\
0 & 0 & 0 & 0 & 0 & 0 & 0 & 0 & 0 & K_{S\text{-}L}+K_{T\text{-}LA} & 0 & -K_{S\text{-}L} \\
0 & 0 & 0 & 0 & 0 & 0 & 0 & 0 & 0 & 0 & K_{S\text{-}R}+K_{T\text{-}LA} & -K_{S\text{-}R} \\
0 & 0 & 0 & -K_V & 0 & 0 & 0 & 0 & 0 & -K_{S\text{-}L} & -K_{S\text{-}R} & K_{S\text{-}L}+K_{S\text{-}R}+K_V
\end{bmatrix}$$

3.3 Hydraulic subsystem

The hydraulic subsystem of the hydraulic power steering system includes pump, supply line, rotary spool valve, hydraulic power cylinder, return line and reservoir. In this section, these components are divided into three groups: the pump, the hoses and the control valve/cylinder. Based on their different features, the three groups are discussed by different measures.

3.3.1 Steering pump

The steering pump is driven by the engine and supplies the power for steering fluid to circulate in the system and to push the piston to assist the steering process. While the vane steering pump satisfies the steering requirement in general, the rotation of the vanes in a steering pump generates a pressure ripple and affects the output characteristics of the pump. It was believed that the steering pump was one of the major source of the noise and vibration of the hydraulic power steering system [Chen (2001), Drew et al. (1995 and 1994)]. The characteristics of steering pumps have been investigated experimentally. The dynamic pressure of a ten-vane steering pump was shown in Figure 3.7 [Chen (2001)]. It was found that the frequencies of the pressure ripple were multiples of the rotational speed of the vane, and the largest peak of the pressure ripple occurred at its fundamental frequency although the characteristics of the pressure ripple included a large number of harmonic components. In the figure, the rotational speed of the pump is 1500 rpm. Therefore, the dominant frequency of the pressure ripple is 250 Hz.

In this research, the pump is modelled as an input to the hydraulic power steering system with pressure ripples. The pressure of the pump can be represented as a mean pressure superimposed with a fluctuating component and it can be shown in the following form,

$$P = \overline{P} + \alpha \cdot \overline{P} \cdot \sin(2\pi \cdot \frac{N_v \cdot R}{60} \cdot t). \tag{3.15}$$

P is the output pressure of the pump, $\overline{P}$ is the mean pressure and $\alpha \cdot \overline{P} \cdot \sin(2\pi \cdot \frac{N_v \cdot R}{60} \cdot t)$ is the ripple component. α is the coefficient of the pressure ripple which is 1.7% in this research based on the literature [Chen (2001), Smid et al. (1998)]. N_v is the number of vanes in the pump which is 10 in this research, R is the rotational speed of the pump (rpm) and t is the time. It can be seen that $\frac{N_v \cdot R}{60}$ is the frequency of pressure ripple (Hz). The pressure ripple at the fundamental frequency has the largest effect on the system and ripples at the higher order frequencies are beyond the concern of this research. Therefore, the fluctuating component of Equation 3.15 only contains the pressure ripple at the fundamental frequency. This assumption is validated by calculation and experimental results of this research.

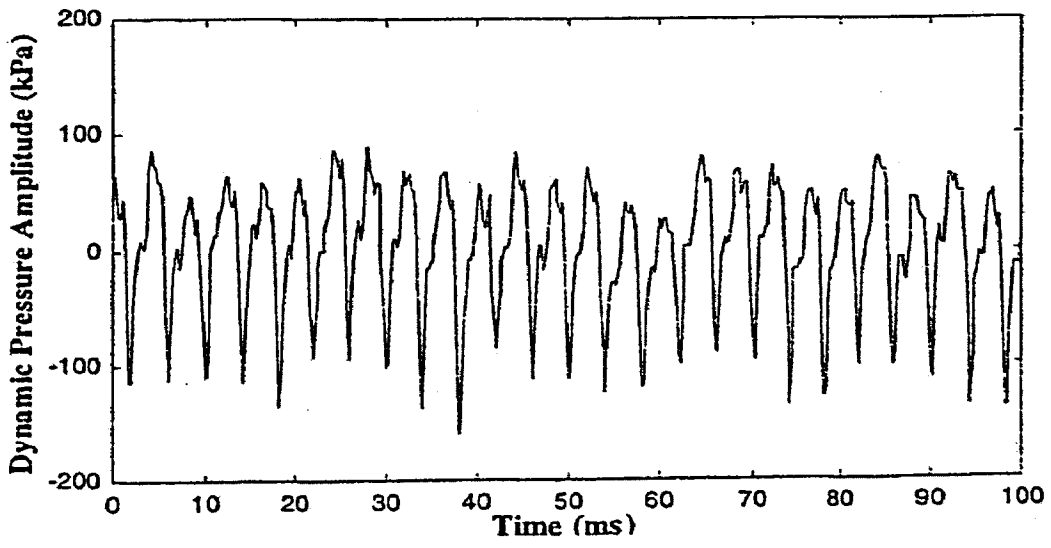

Figure 3.7 Pressure waveform of steering pump [Chen (2001)]

3.3.2 Hydraulic hoses

Hydraulic power steering systems comprise a number of tubes and hoses connecting the pump, the valve and the reservoir. Matsunaga *et al.* (2001) showed that the return line and the cylinder on the lower pressure side had very little effect on the vibration characteristics. This was supported by the experimental investigation reported by Drew et al (1995) that the return line impedance can be neglected if the supply pressure exceeds about 10 bar. This is also confirmed by the testing results of this research. For simplicity, the return line is not included in this steering system model, and only the high pressure supply line is considered.

In the steering system, the steering pump driven by the engine continuously supplies the energy not only to push the piston in the hydraulic cylinder but also to supplement the power loss in the hydraulic circuit, and the temperature of the steering fluid is stable in most situations. The efficiency of the hydraulic steering system depends on the throttling and heat losses when fluid passes through valves, hoses and orifices. Detailed investigation on the efficiency of the steering system is beyond the scope of this study. Rather, I focus on the dynamic characteristics of the steering system.

Usually the supply line consists of three elements, a steel tube connecting the pump, a tube connecting the spool valve, and a hose between them which is fabricated from wire braid and synthetic rubber. They are shown as Tube 1, Tube 2 and Hose respectively in Figure 3.8. The calculations for the supply line take into account the compressibility of the steering fluid and the elasticity of hose and tubes which are essential for the hydraulic dynamics of the system.

Three main steps are used to develop the model of the supply line. At first, a tube or a hose is modelled as a single hydraulic element, and using fluid impedance method a lumped parameter model is applied to derive the impedance parameters. Then, a distributed parameter model generates a dynamic relation of the inlet pressure, inlet flow rate, outlet pressure, and outlet flow rate. Finally, three transfer matrices of the

three elements produce a total transfer matrix of the supply line and the dynamic feature is obtained.

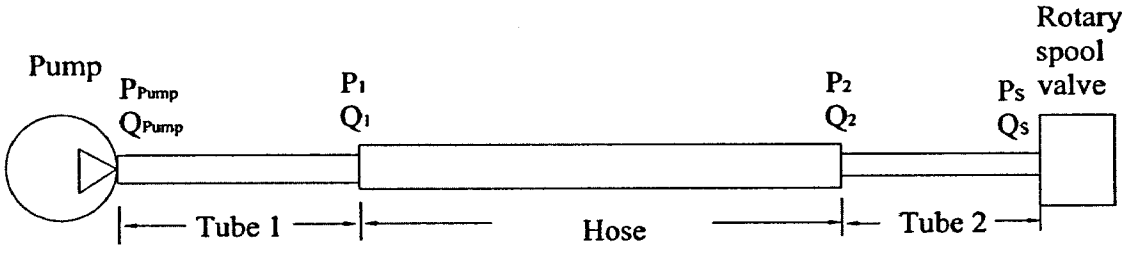

Figure 3.8 Schematic of supply line

For the Tube 1, the parameters R_h, C_h and L_h are based on the characteristics of the tube and the working fluid, and are calculated by Equations (2.1) to (2.3).

Then, a transfer matrix could be developed by the equation,

$$T_{Tube-1} = \begin{bmatrix} \cosh(\gamma l) & -Z_c \sinh(\gamma l) \\ -\dfrac{\sinh(\gamma l)}{Z_c} & \cosh(\gamma l) \end{bmatrix}$$

where the propagation constant $\gamma = \sqrt{C_h j\omega (L_h j\omega + R_h)}$, the characteristic impedance $Z_c = \dfrac{\beta_e \gamma}{A \cdot j\omega}$, A is the inner area of the pipe or hose, β_e is the equivalent

bulk modulus, ω is the frequency of the excitation, l is the length of the tube and $j = \sqrt{-1}$.

So, the pressure and flow rate at the two ends of Tube 1 can be written as,

$$\begin{bmatrix} P_1 \\ Q_1 \end{bmatrix} = [T_{Tube-1}] \begin{bmatrix} P_{pump} \\ Q_{pump} \end{bmatrix} \tag{3.16}$$

After applying the same procedures on the hose and Tube 2, it leads to the following equations,

$$\begin{bmatrix} P_2 \\ Q_2 \end{bmatrix} = [T_{Hose}] \begin{bmatrix} P_1 \\ Q_1 \end{bmatrix} \tag{3.17}$$

where $[T_{Hose}]$ is the transfer matrix of the hose.

$$\begin{bmatrix} P_S \\ Q_S \end{bmatrix} = [T_{Tube-2}] \begin{bmatrix} P_2 \\ Q_2 \end{bmatrix} \tag{3.18}$$

where $[T_{Tube-2}]$ is the transfer matrix of the Tube 2.

For the whole supply line model, where the outlet of Tube 1 is the inlet of the hose, and the outlet of hose is the inlet of Tube 2, hence the transfer matrix of the whole supply line is obtained by multiplying the three transfer matrices of the three elements.

As a result, the dynamic hydraulic response of the supply line is shown in Equation (3.19),

$$\begin{bmatrix} P_S \\ Q_S \end{bmatrix} = [T_{Supply}] \begin{bmatrix} P_{pump} \\ Q_{pump} \end{bmatrix} \tag{3.19}$$

where $T_{Supply} = T_{Tube-2} \cdot T_{Hose} \cdot T_{Tube-1}$, $\begin{bmatrix} P_{pump} \\ Q_{pump} \end{bmatrix}$ and $\begin{bmatrix} P_S \\ Q_S \end{bmatrix}$ are the pressure, flow rate of the pump and the pressure, flow rate of the inlet of spool valve respectively. The output of the supply line model supplies the input to the rotary spool valve subsystem.

3.3.3 Rotary spool valve and hydraulic power cylinder

The rotary spool valve used in this hydraulic power steering system can be modelled as a four-way open centre valve, in which the fluid passes through four opening areas simultaneously. During a steering manoeuvre, two opening areas of the valve increase, whilst the other two opening areas decrease. These changes of the opening areas increase the pressure of the fluid in the supply line, since the steering pump can be regarded as a constant flow rate pump. Consequently, the pressure difference between the two sides of the hydraulic cylinder increases. The standard turbulent-flow orifice Equation (3.20) is used to describe the function of the valve:

$$Q = C_d A \sqrt{\frac{2}{\rho}(P_1 - P_2)} \tag{3.20}$$

where Q is the flow rate, C_d is the discharge coefficient, A is the orifice area, ρ is the density of the fluid, and $(P_1 - P_2)$ is the pressure difference.

Figure 3.9 is the schematic of the rotary spool valve and the hydraulic power cylinder. As a four-way open centre valve, the spool valve has the following relationships of the flow rates.

$$Q_S = q_1 + q_2 \tag{3.21}$$

$$Q_L = q_1 - q_4 \tag{3.22}$$

Combining Equations (3.20) to (3.22), the governing equations of the rotary spool valve are:

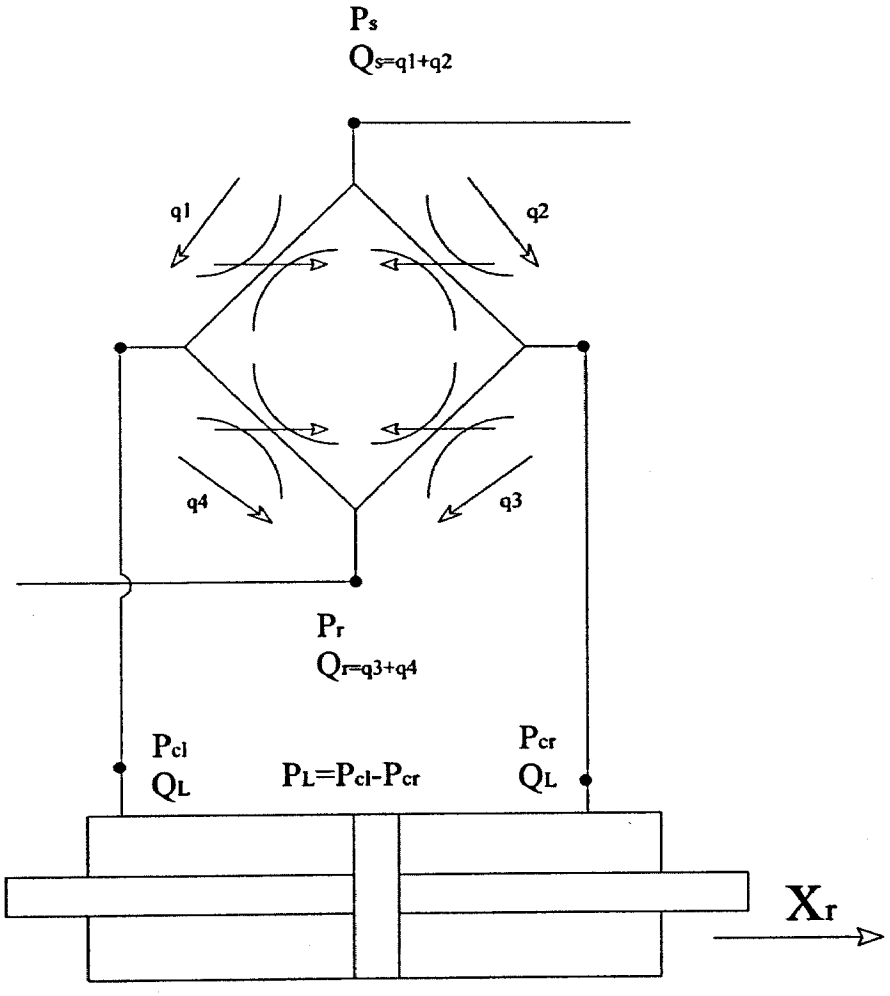

Figure 3.9 Rotary spool valve and hydraulic power cylinder

$$Q_S = C_d A_1 \sqrt{\frac{1}{\rho}(P_S - P_L)} + C_d A_2 \sqrt{\frac{1}{\rho}(P_S + P_L)} \tag{3.23}$$

$$Q_L = C_d A_1 \sqrt{\frac{1}{\rho}(P_S - P_L)} - C_d A_2 \sqrt{\frac{1}{\rho}(P_S + P_L)} \tag{3.24}$$

where Q_S is the supply flow rate, A_1 and A_2 are the opening and closing areas of the orifices of the valve respectively, P_S and P_L are the pressure of supply flow and the pressure drop across the load, and Q_L is the load flow rate. ρ is the density of the fluid.

As same as the steering fluid in the supply line, the fluid in the chamber of the hydraulic power cylinder is also considered compressible. Since the power cylinder is a double-rod linear actuator controlled by the spool valve, the flow rate and the pressure change of the cylinder has the following relationship [Merritt (1967)].

$$Q_L = A_P \dot{x}_P + \frac{V}{2\beta} \dot{P}_L \tag{3.25}$$

where the V is the volume of the chamber, the β is the bulk modulus of the fluid, A_P is the area of piston and $\dot{x}_P$ is the velocity of piston. The leakage through the seal between the two sides of the piston is ignored in this equation.

Rearranging it, the governing equation for the pressure change, $\dot{P}_L$, can be obtained.

$$\dot{P}_L = \frac{2\beta(Q_L - A_P \dot{x}_P)}{V} \tag{3.26}$$

The numerical calculation is adopted to solve Equations 3.23, 3.24 and 3.26 step by step. Figure 3.10 shows the procedure of the calculation. The twisting degree of the torsional bar determines the open areas of the rotary spool valve. P_S is solved from Equation 3.23 and is substituted into Equation 3.24. Then, P_L is obtained and substituted into Equation 3.26 and the $\dot{P}_L$ is calculated. Therefore the P_L of the next step, $P_L(i+1)$, is obtained and it is applied on the mechanical subsystem to get a new twisting degree of the torsional bar.

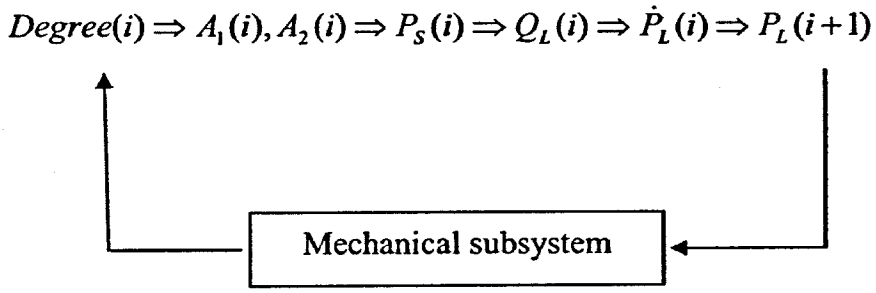

Figure 3.10 Numerical calculation procedure of hydraulic subsystem

In this study, A_1 and A_2 in Equations 3.23 and 3.24 are given special attention. Unlike usual lateral spool valves and rotary spool valves, the valves used in steering systems have more complicated orifice shapes. The reason is that the valves with simply shaped orifices will suddenly shut the outlets, and as a result this kind of valve will not satisfy the requirement of the vehicle steering feel and may induce steering system vibration. So the edges of rotary spool slots used in steering systems are designed and manufactured with primary and secondary edges to obtain suitable hydraulic boost characteristics. Figure 3.11 is a top view schematic of the open area. When the spool rotates relative to the sleeve, one side of orifice is opened and the other side is closed. At first, the width of B_2 of the long open edge, W_2, decreases,

and after a certain angular displacement, the W_2 closes totally and the short open edge, W_1, becomes the only open area. It is evident that the closing area of the orifice is nonlinear against the relative rotation between spool and sleeve.

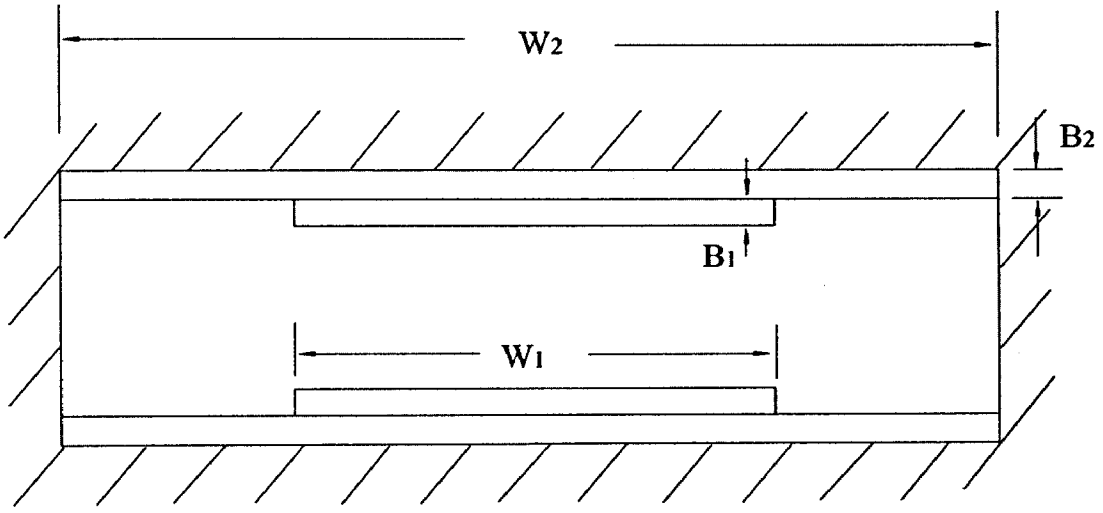

Figure 3.11 Schematic of open area of steering control valve

Equation 3.27 shows the nonlinearity of the closing area, where R is the radius of spool, φ is the rotation, and φ_{key} is the angle at which the long open edge closes.

$$\text{Open area} = \begin{cases} B_1 W_1 + (B_2 - R\varphi)W_2 & \text{if } \varphi <= \varphi_{key} \\ (B_1 + B_2 - R\varphi)W_1 & \text{if } \varphi > \varphi_{key} \end{cases} \tag{3.27}$$

The nonlinearity of the open area is integrated in the numerical simulation.

After the model of the hydraulic subsystem is completed, it is included into the steering system by the interactions between the mechanical and the hydraulic subsystems, such as the torsional bar and rotary spool valve.

In summary, a comprehensive mathematical model of the rack and pinion hydraulic power steering system is developed in this chapter. The mechanical and hydraulic components of the system are integrated in the model by adopting different measures and techniques. In chapter 4, the mechanical components of the steering system are studied by free vibration analysis, and the transient responses of the steering system are investigated by numerical calculation. The model introduced in this chapter was also used as a general hydraulic steering system model. In Chapter 6 the variable ratio and speed sensitive steering systems models are developed on the base of the general model.

CHAPTER 4 FREE AND FORCED VIBRATION ANALYSIS

4.1 Introduction

In this chapter, a typical rack-pinion hydraulic power steering system is used to validate the developed model in both the time domain and frequency domain. Firstly, free vibration analysis of the mechanical subsystem is conducted to obtain the natural frequencies and mode shapes of the subsystem. Then, based on the time domain steering system model, the system responses, such as the angular displacement of the tyres and the operating pressure in the hydraulic cylinder, are obtained by a numerical integration scheme.

It should be noticed that the while the time domain analysis integrates the mechanical and hydraulic subsystems, the free vibration analysis discussed here is only for the mechanical subsystem of the steering system. The frequency domain analysis of the *whole* power steering system will be performed in the next chapter. The comparison of the results of the time domain analysis and frequency domain analysis will also be discussed and compared in the next chapter.

The parameters of a typical rack and pinion hydraulic power steering system are used in both the time domain analysis and the frequency domain analysis. Most of the parameters are obtained from the steering system manufacturer or the car specifications, and the others are from the literature review. The key parameters of the system are listed in Table 4.1.

Table 4.1 Parameters of a typical rack and pinion hydraulic power steering system

Parameter	Value
Moment of inertia of steering wheel	0.03 kg·m^2
Ratio between rack and pinion	1.04×10^{-4} m/rad
Torsional bar stiffness	95 Nm/rad
Rack mass	4.5 kg
Length of the hose 1 in the supply line	0.4 m
Length of the pipe in the supply line	0.4 m
Length of the hose 2 in the supply line	0.13 m
Inner radius of the hose	0.005 m
Outer radius of the hose	0.009 m
Length of the long feed pipe of the cylinder	0.55 m
Length of the short feed pipe of the cylinder	0.32 m
Inner radius of the feed pipe	0.004 m
Outer radius of the feed pipe	0.006 m
Elastic modulus for steel pipe	2.1×10^{11} Pa
Pump discharge flow rate	1.33×10^{-4} m^3/s
Number of vanes in the pump	10
Discharge coefficient of rotary spool valve	0.7
Density of the fluid	816 kg/m^3
Bulk modulus of the fluid	1.613×10^9 N/m^2
Kinematic viscosity of the fluid	7×10^{-6} m^2/s

4.2 Free vibration analysis of mechanical subsystem

Based on the mechanical subsystem model introduced in the last chapter, free vibration analysis is performed to determine the natural frequencies and the corresponding mode shapes of the mechanical subsystem. Since in this analysis the interactions between the mechanical components and the hydraulic components are modelled as the applied external forces only, the dynamics of the fluid circuits are not included in the free vibration analysis of the mechanical subsystem.

The second order differential equations of the mechanical subsystem, Equation 3.14, could be rewritten as first order differential equations,

$$[\dot{X}] = [A][X] + [B][F] \tag{4.1}$$

where,

$$[\dot{X}] = \begin{bmatrix} \dot{u} \\ \ddot{u} \end{bmatrix}_{24\times 1},$$

$$[A] = \begin{bmatrix} 0 & I \\ -M^{-1}K & -M^{-1}C \end{bmatrix}_{24\times 24},$$

$$[X] = \begin{bmatrix} u \\ \dot{u} \end{bmatrix}_{24\times 1},$$

$$[B] = \begin{bmatrix} 0 \\ -M^{-1} \end{bmatrix}_{24\times 12},$$

and $[F]_{12\times 1}$ is the vector of external forces and torques. In system matrix $[A]$, I is an identity matrix. The natural frequencies, damping ratios and mode shapes can be obtained by performing the eigenvalue and eigenvector analysis of the system matrix $[A]$.

The 12 DOF mechanical subsystem has 12 natural frequencies and corresponding mode shapes, including one 0 Hz rigid body motion mode. Figures 4.1 to 4.11 show the 11 non-rigid body motion natural frequencies and the corresponding mode shapes. The 12 points in these figures represent the 12 DOFs of the mechanical subsystem, and the lengths of the vertical lines on the 12 points show the normalised modal

coefficients at certain natural frequency. The symbol θ represents the angular displacement and x represents the translational displacement. The point θ_{SW} represents the angular displacement of steering wheel, the point θ_C is the steering column, the point θ_P is the pinion, the point x_R is the rack, the points θ_{FW-L} and θ_{FW-R} are the angular displacements of the left and right front wheels (road wheels) respectively, the θ_{CP-L} and θ_{CP-R} are the angular displacements of the contact patches of the front tyres respectively, the x_H is the hydraulic cylinder, the x_V is the displacement of the front half of the vehicle, and the x_{FW-L} and x_{FW-R} are the translational displacements of the two front wheels.

Figure 4.1 shows a low natural frequency that is mainly due to the large mass of the front half vehicle. In Figure 4.2, the normalised modal coefficient of the pinion is the largest among the 12 components. Compared to the pinion, the modal coefficients of other components are too small to be shown in this figure. It can be found that the pinion is the main vibration component, called the dominant component, at this natural frequency (21.02 Hz), and it affects this natural frequency much greater than other components. The twist effects of the front wheels and the contact patches of the front tyres are significant at the 21.24 Hz natural frequency which is shown in Figure 4.3. The rotational movements of the contact patches of the front tyres are obvious in Figures 4.4 and 4.5. It can be found in Figures 4.6 and 4.7 that the translational vibrations of the front wheels dominate the 72.85 Hz and 74.42 Hz in this mathematical model. It can be seen that the modes shown in Figures 4.4 to 4.7 are local modes and have limited effects to the system. According to Figures 4.8 and 4.9, the steering column and the pinion are the dominant components in 137.31 Hz and 175.57 Hz respectively. There are two high natural frequencies in the 12 DOF model and they are shown in Figures 4.10 and 4.11. The 221.38 Hz natural frequency is because the hydraulic power cylinder is almost rigidly fixed on the frame of the vehicle body. The effect of this vibration mode to the system is quite limited. The 1472.05 Hz natural frequency in Figure 4.11 is due to the small moment of inertia of the pinion in the model. It is a local mode and this frequency is also not important for the hydraulic power steering system.

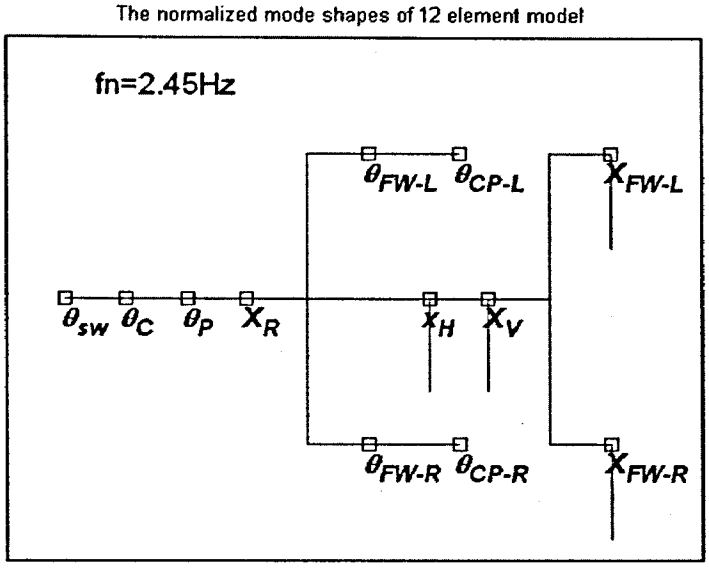

Figure 4.1 Natural frequency (2.45 Hz) and mode shapes of the mechanical subsystem

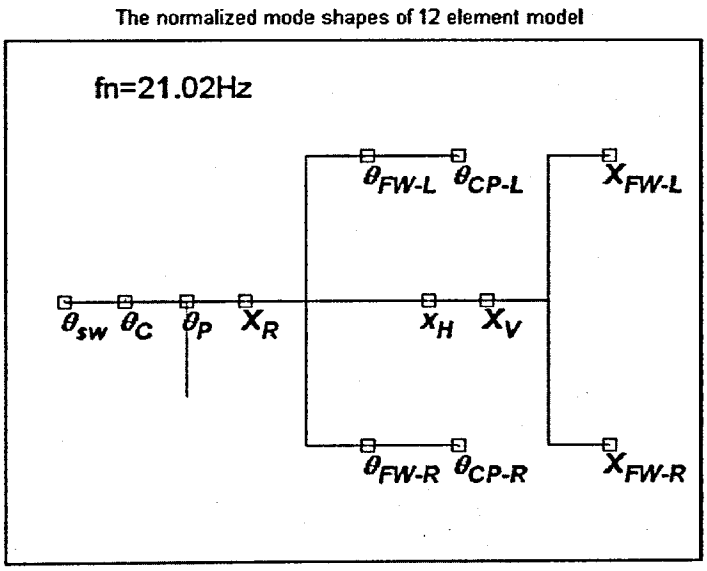

Figure 4.2 Natural frequency (21.02 Hz) and mode shapes of the mechanical subsystem

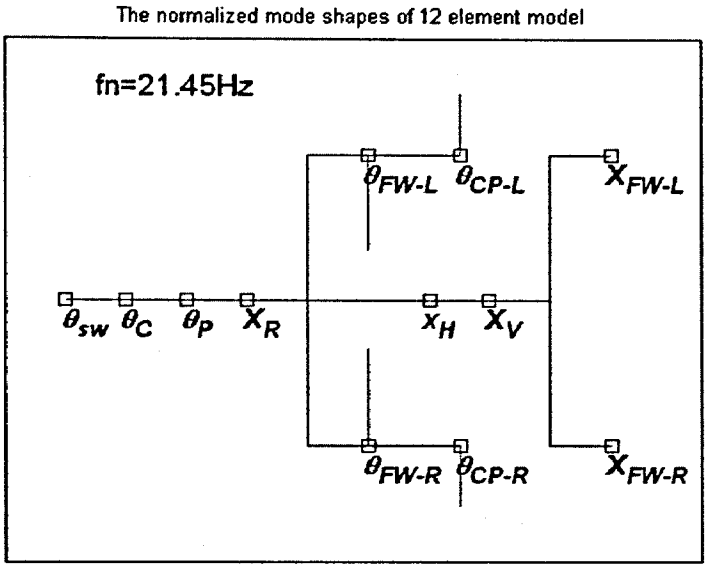

Figure 4.3 Natural frequency (21.45 Hz) and mode shapes of the mechanical subsystem

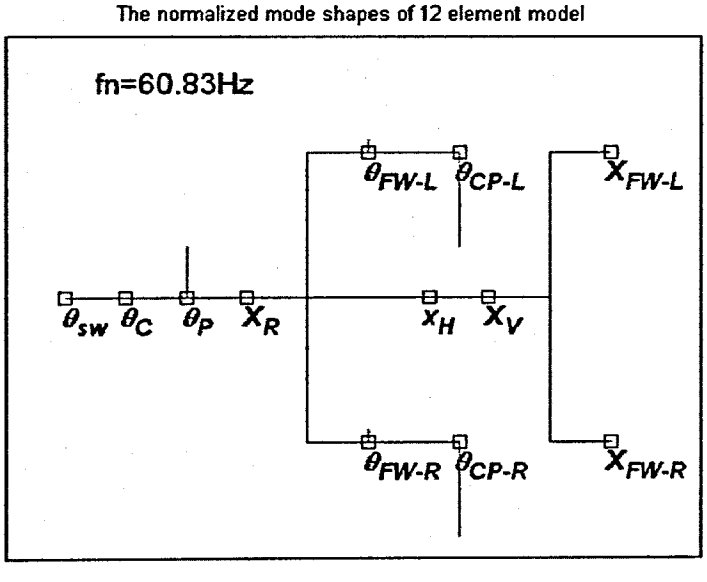

Figure 4.4 Natural frequency (60.83 Hz) and mode shapes of the mechanical subsystem

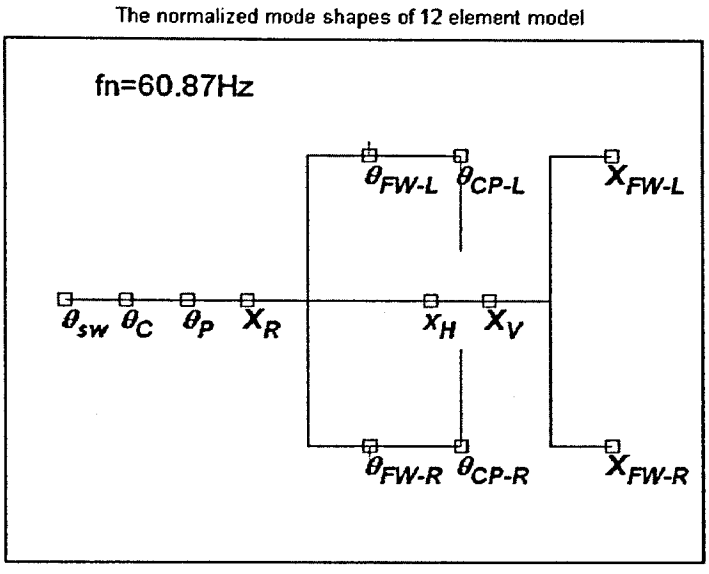

Figure 4.5 Natural frequency (60.87 Hz) and mode shapes of the mechanical subsystem

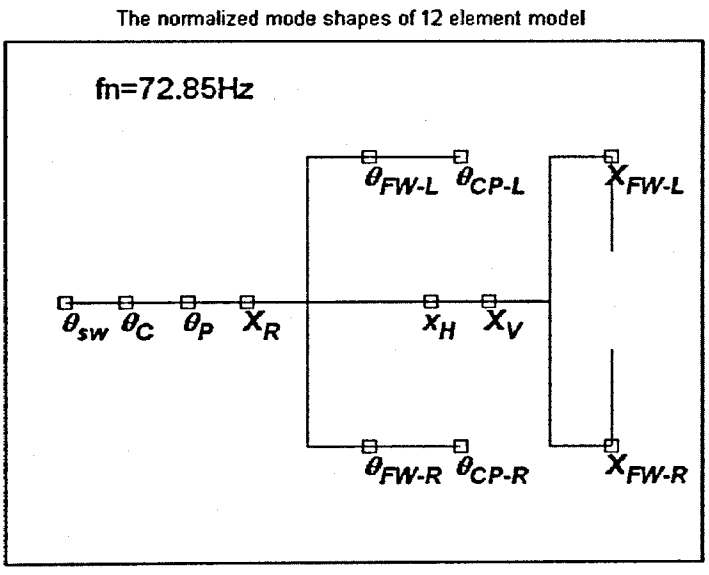

Figure 4.6 Natural frequency (72.85 Hz) and mode shapes of the mechanical subsystem

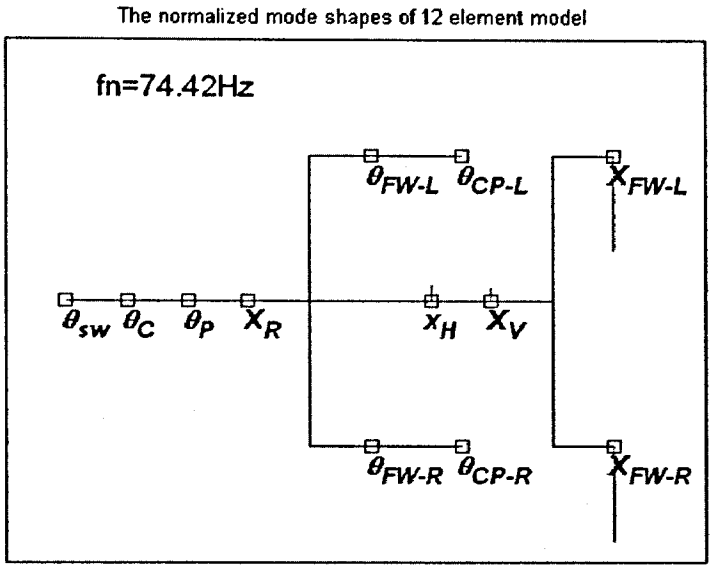

Figure 4.7 Natural frequency (74.42 Hz) and mode shapes of the mechanical subsystem

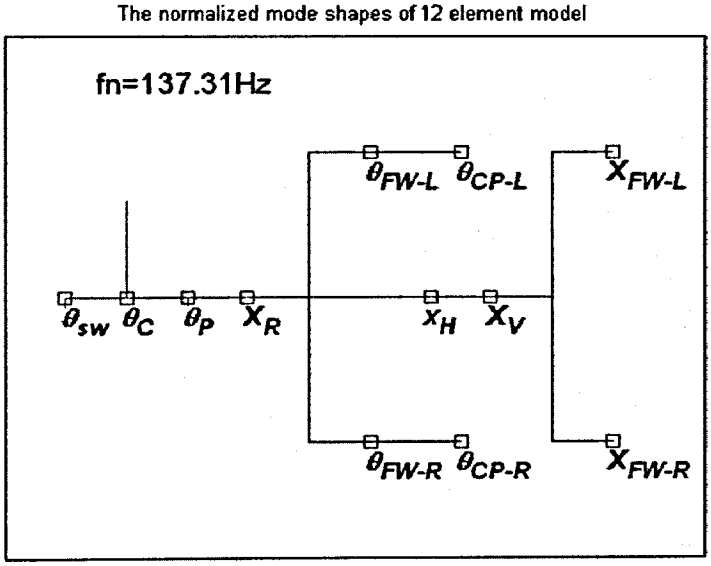

Figure 4.8 Natural frequency (137.31 Hz) and mode shapes of the mechanical subsystem

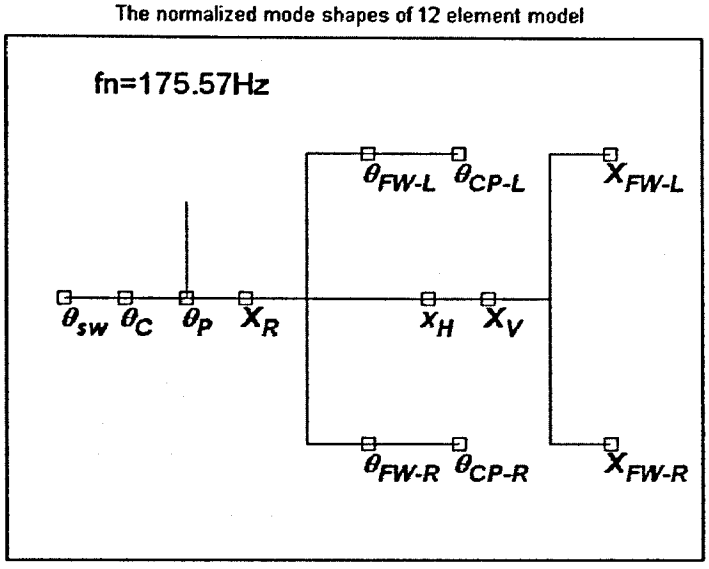

Figure 4.9 Natural frequency (175.57 Hz) and mode shapes of the mechanical subsystem

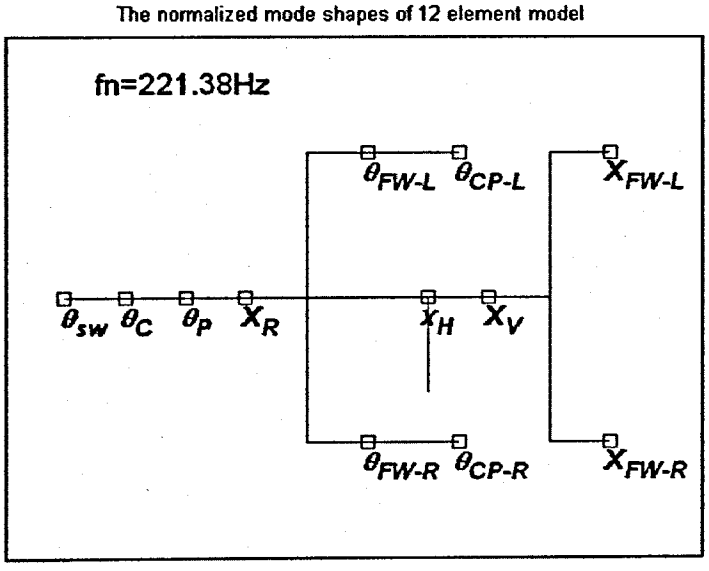

Figure 4.10 Natural frequency (221.38 Hz) and mode shapes of the mechanical subsystem

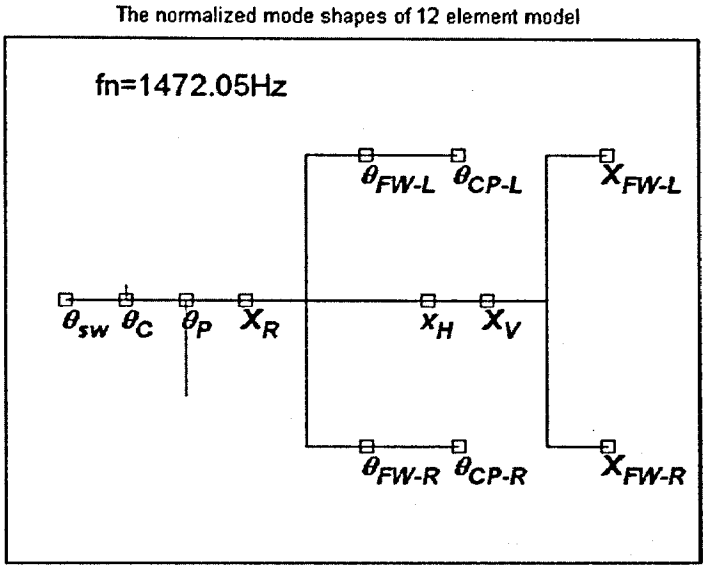

Figure 4.11 Natural frequency (1472.05 Hz) and mode shapes of the mechanical subsystem

In Figures 4.1 to 4.11, no displacement is shown on some nodes. This is because the lengths of the vertical lines on the 12 points are normalised and some displacements are too small to be shown graphically.

Table 4.2 lists these 11 natural frequencies of the mechanical subsystem, as well as the responding dominant vibration components at each natural frequency. The second and third natural frequencies are given more attention here because they are in the typical steering shudder frequency range. These two natural frequencies of the mechanical subsystem are between 21 and 22 Hz and the different components, including the pinion, the front wheels and the contact patches of tyres are the dominant components of the two frequencies respectively.

Table 4.2 shows that the pinion is the dominant component in the 21.02 Hz natural frequency. The effect of the vibration of the pinion to the steering shudder is apparent because the twist angle between the pinion and the steering column, which is actually the twist angle of the torsional bar, controls the high pressure fluid in the cylinder and the vibration of the pinion directly affects the twist angle.

The front wheels and the contact patches of the tyres have the largest influence at the natural frequency at 21.45 Hz shown in Figure 4.3. The opposite signs of the model coefficients of the wheels and the contact patches indicate that it is the twist of the tyres that affects this natural frequency. This mode also has significant effect on the steering shudder because the vibration of the front wheels can be translated to the hydraulic piston through the tie rods and the rack.

In summary, the shudder frequency is located by the free vibration analysis and the pinion, the front wheels and tyres are the main components contributing the steering shudder. The following time domain analysis corroborates the free vibration analysis, and the experiments of steering shudder also verify the natural frequency analysis here and will be discussed in Chapter 8.

Table 4.2 Mechanical subsystem natural frequencies and dominant components

No.	Natural Frequency (Hz)	Dominant Components
1	2.45	Hydraulic cylinder, vehicle body and translational movement of two wheels
2	21.02	Pinion
3	21.45	Two wheels and the contact patches of the tyres
4	60.83	Contact patches of tyres
5	60.87	Contact patches of tyres
6	72.85	Translational movement of two front wheels
7	74.42	Translational movement of two front wheels
8	137.31	Steering column
9	175.57	Pinion
10	221.38	Hydraulic cylinder
11	1472.05	Pinion

4.3 Forced vibration analysis

4.3.1 Steering shudder

Based on the models developed in the last chapter, the mechanical subsystem and the hydraulic subsystem, are integrated into a hydraulic power steering system model in the time domain. The effects of the hydraulic subsystem on the mechanical subsystem are taken into account as an applied external force. One of the main interactions of the two subsystems is that the twist angle of the torsional bar in the mechanical subsystem controls the opening angle of the rotary spool valve in the hydraulic subsystem. Another interaction is that the pressure fluctuations in the supply line alter the operating pressure inside the hydraulic cylinder, and therefore alter the external force of the mechanical subsystem. In the calculation, the responses of the mechanical subsystem determine the operating conditions for the hydraulic subsystem and the hydraulic boost force generated by the hydraulic subsystem is in turn applied to the mechanical subsystem. For instance, a torque applied to the steering wheel generates a twist angle of the rotary spool valve, and the twist angle then discharges high pressure fluid into one side of the hydraulic cylinder. When the sum of the hydraulic boost force and the driving force from the pinion overcomes the friction against the ground of the two front tyres, the rack moves and the pinion rotates accordingly. Consequently, a new twist angle state is generated and new state of the hydraulic system is created.

Using numerical integration, the transient responses of the translational and angular displacements of the mechanical parts and the fluid states in terms of flow rate and pressure of the fluid circuit can be determined based on the integrated steering model under various operating conditions. The Runge-Kutta method is used in the numerical calculation to analyse the model in the time domain.

In this section, the focus is on the low frequency vibration of the steering system: the steering shudder. The high frequency vibration, the pressure ripple in the system will be discussed in Section 4.3.2.

Figure 4.12 shows a typical steering system's response in the first 2 seconds when the vehicle is at parking speed. At time 0, the steering system is at the neutral position and the displacements and velocities of all the steering components are zero. From time

zero, a slow angular velocity input, which is 0.2 rad/s (11.46 deg/s), is applied on the steering wheel.

The top graph of Figure 4.12 is the angular displacement of the steering wheel and the pinion. A dashed line and a solid line represent these displacements respectively. It can be seen the difference between the two angular displacements due to the compliance of the steering column and the torsional bar. Under the constant angular velocity input, the steering wheel has about 23 degrees angular displacement after 2 seconds, and the pinion rotates about 21.6 degrees.

The second graph displays the angular displacement of the front wheels and tyres. At this situation, although a dash line and a solid line are used to plot the displacements of the wheel and the contact patch of the tyre respectively, they overlap each other because the small angular input can not generate enough displacement difference between the two elements in the first 2 seconds. The two elements have about 0.68 degrees displacement after the steering wheel turns 23 degrees. This is due to the ratios and the compliance of the system.

The third top graph shows the twist angle of the torsional bar. The twist angle quickly increases to about 1.1 degrees from 0 deg within 0.2 second, and it continues to increase to about 1.3 degrees at 0.8 second. Then it almost keeps this value after the first 0.8 second. There is no evident vibration on the twist angle at this situation.

The boost force in the hydraulic chamber is shown in the bottom graph of Figure 4.12. The force increases to 160 N after 0.2 second, and it reaches 290 N at 0.8 second. It is found, in the first 0.8 second, that the slope of the boost force is less that the slope of the twist angle. But the small change of the twist angle at about 1.2 seconds maximises the boost force. This clearly shows the effect of the nonlinearity of the rotary spool valve on the system, especially to the boost force.

Figure 4.13 shows the system's response under a quicker angular velocity input, 3 rad/s (171.7 deg/s). Naturally, the steering wheel rotates about 340 degrees after 2

seconds. The difference of the displacements of the steering wheel and the pinion is generated although it cannot be seen in Figure 4.13 due to scale of the graph.

The second graph of Figure 4.13 clearly shows the angular difference between the wheel and the contact patch of the tyre. After 2 seconds, the wheel rotates about 14.9 degrees while the contact patch of the tyre turns about 9.1 degrees because of the twist stiffness of the tyres.

According to the plot of the twist angle of the torsional bar, the twist angle rapidly increases to 1.5 degrees at 0.2 second, and keeps increasing until the 1.0 second mark. After 1.0 second, an obvious vibration occurs on the twist angle of the torsional bar. Corresponding to this plot, the bottom plot of Figure 4.13 also shows the vibration of the boost force and the frequency of the vibration is about 20.90 Hz which is very close to the shudder natural frequency obtained from the free vibration analysis. At this situation, the effect of the twist angle of the torsional bar on the shudder is clear, and it agrees the free vibration analysis on the effect of the pinion. The twist effect of the tyres is not so obvious although the vibration of the tyre could be observed after the second graph of Figure 4.13 is enlarged.

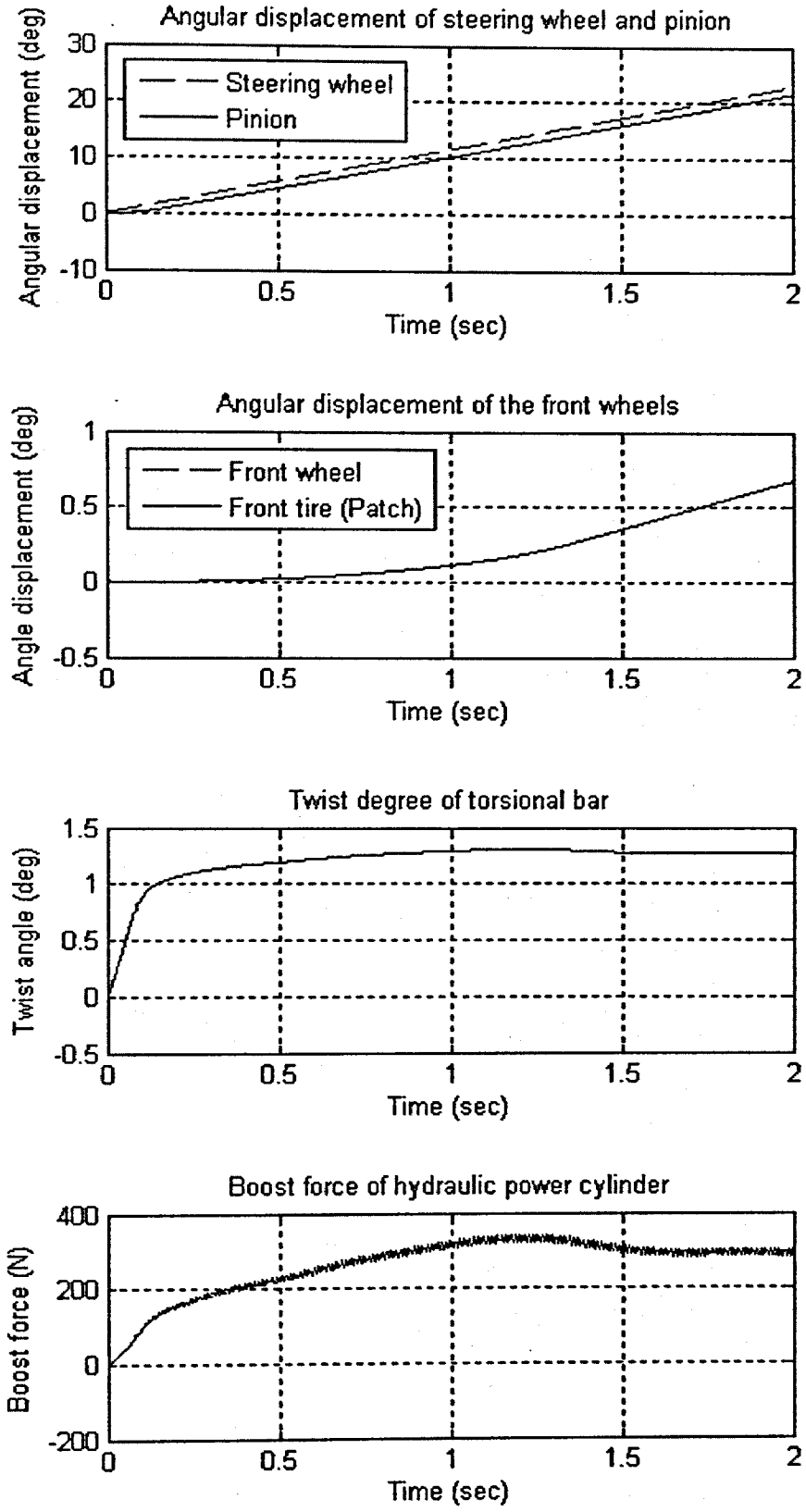

Figure 4.12 Responses of hydraulic power steering system to 0.2 rad/s steering input

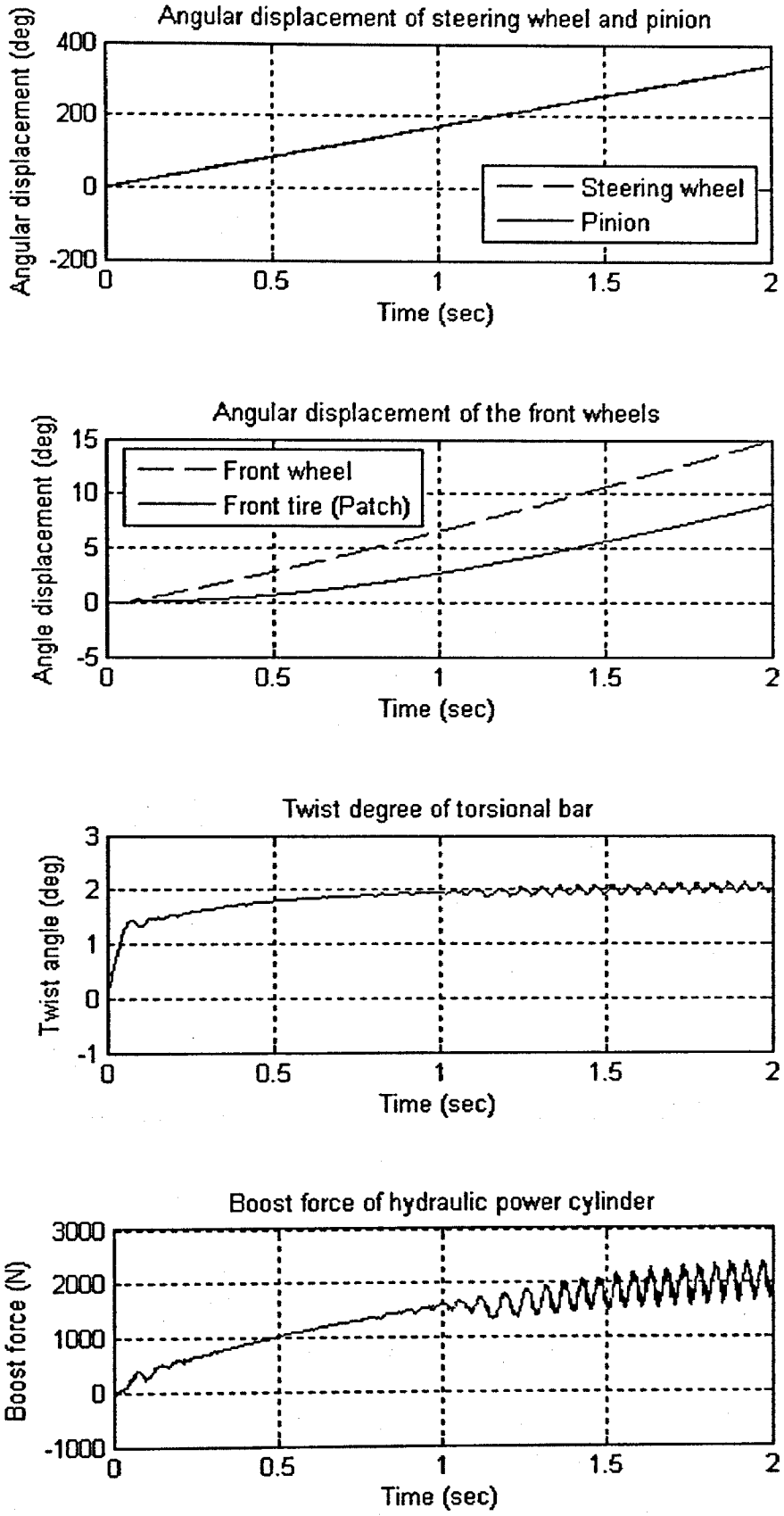

Figure 4.13 Responses of hydraulic power steering system to 3 rad/s steering input

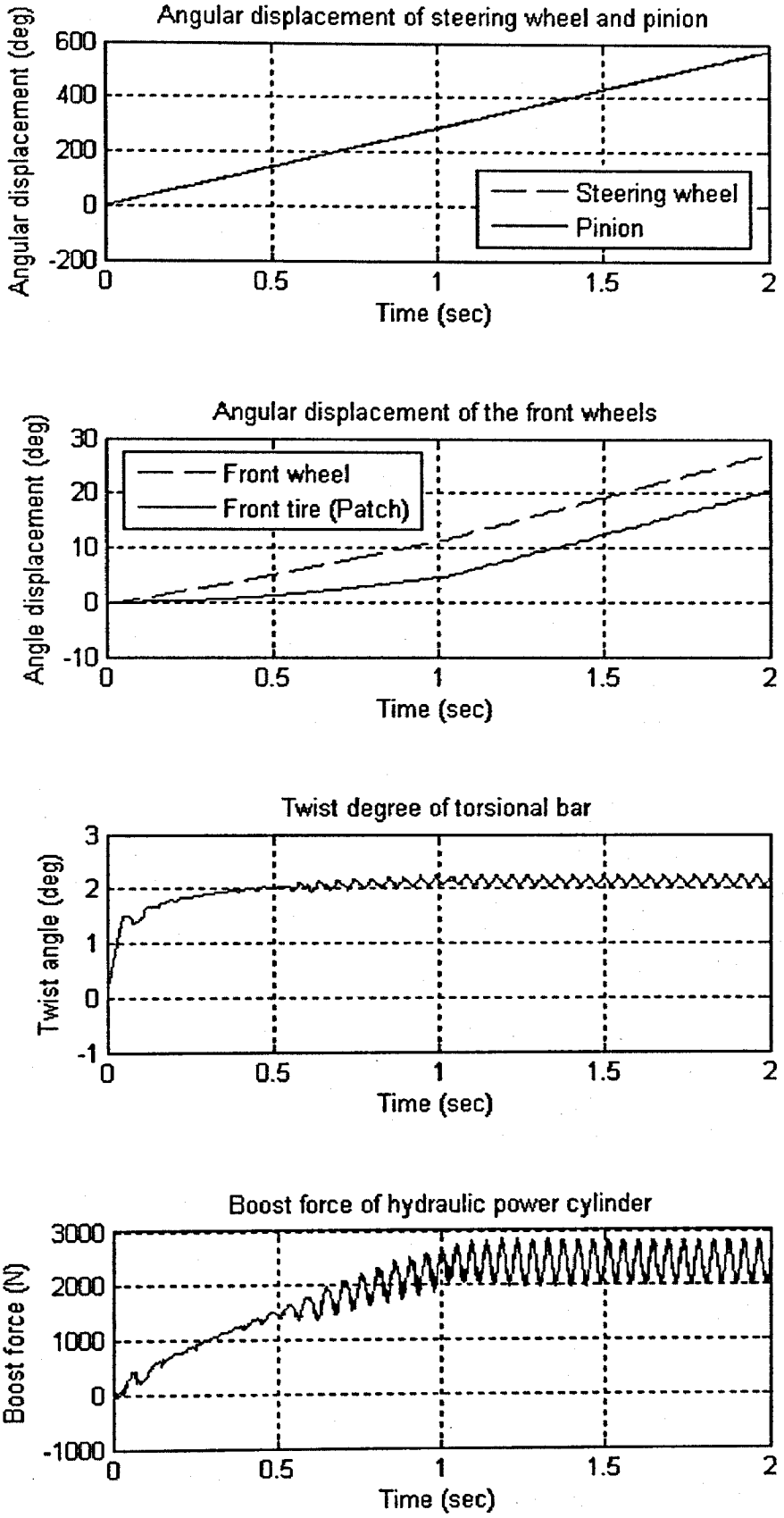

Figure 4.14 Responses of hydraulic power steering system to 4 rad/s steering input

The response of the steering system after a 4 rad/s (229.2 deg/s) input is applied on the steering wheel is shown in Figure 4.14. While this quick input is not usual in driving, it is helpful in the study of the dynamic characteristics of the steering system. Under this input, the vibrations of the wheel and the tyre are noticeable in the second graph of Figure 4.14. The frequencies of the vibrations of the wheel and the tyre are about 21.74 Hz which confirms the free vibration analysis in Figure 4.3.

Similar to the graph in Figure 4.13, the plot of the twist angle of the torsional bar in Figure 4.14 illustrates the vibration. But the vibration in Figure 4.13 starts from about 1.0 second, whereas the vibration in Figure 4.14 starts from about 0.5 second. It is believed that this is because the 4 rad/s input generates the high twist angle degree quicker than the 3 rad/s input does. In the bottom graph of Figure 4.14, a shudder starts from about 0.5 second, and the frequency of it is about 21.69 Hz which is also close to the result of the free vibration analysis.

In summary, Figures 4.12, 4.13 and 4.14 show the time domain responses of the hydraulic power steering system under various inputs. When a small angular velocity input is applied on the steering wheel, the twist angle of the torsional bar has a smaller value and the steering system does not show the steering shudder. When a relatively quicker angular velocity input is applied, the twist angle of the torsional bar is larger and has the vibration. The vibration affects the boost force in the hydraulic power cylinder and generates the boost force vibration. In the shudder situation, the dominant components and the frequencies obtained from the time domain analysis are same as the results of the free vibration analysis of the mechanical subsystems.

The rotary spool valve is the key component of the hydraulic power steering system, and its operating characteristics have significant influences on the performance of the whole steering system. By using the mathematical model developed in this research, the valve characteristics could be conveniently obtained by comparing the responses of the twist angle of the torsional bar and the boost pressure.

Figure 4.15 shows the testing results and simulation results of the characteristics of the rotary spool valve, which is presented by the relationship between the twist angle of

the torsional bar and the working pressure of the hydraulic cylinder. The test was conducted by Tristar Steering and Suspension Australia Ltd., one of the main steering system manufacturers in Australia. The cylinder pressure was measured over a range of torsonal bar twist angles.

In the simulation of this research, a high friction force is applied to the tyre model in order to provide enough load for high twist angles. The twist angle and the working pressure are calculated separately in time domain, and then they are combined to obtain the continuous valve characteristics. From the figure, the simulated result which is from the mathematical model is in good agreement with the testing results, and the nonlinearity of the valve characteristics is illustrated by the simulation results. Moreover, the vibration signal in the simulated result captures the dynamic relationship between the twist angle and the pressure which is mainly caused by the compressibility of working fluid and the elasticity of supply line.

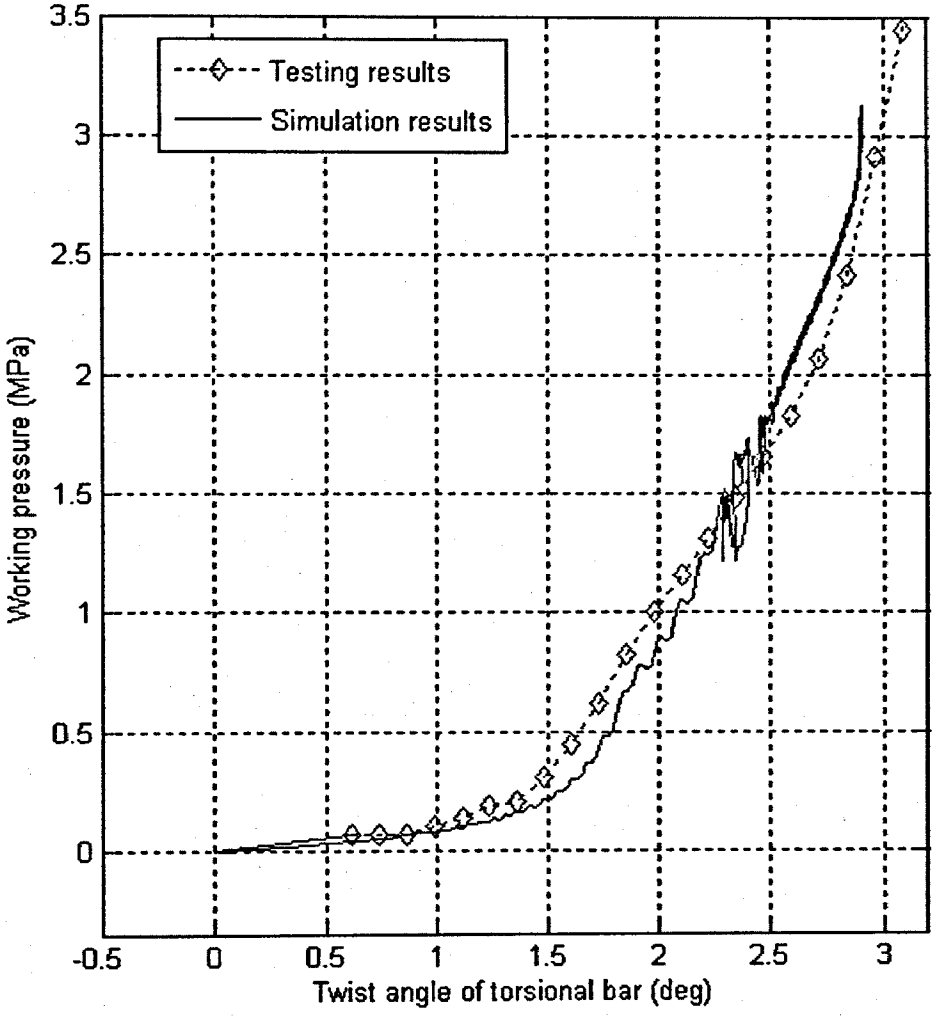

Figure 4.15 Simulation and testing results of characteristics of rotary spool valve

4.3.2 Effects of the pressure ripple

According to the literature review, the high frequency pressure ripple in the steering system is mainly generated by the steering vane pump. Since a ten vane pump is fitted in the steering system, the fundamental frequency of the pressure ripple of the pump is ten times of the rotary speed of the pump which can be calculated by Equation 3.15. The high pressure ripple also affects the dynamic characteristics of the steering system although it is not as significant as the steering shudder in practice. In this section, the dynamic performances of some key steering components are studied.

From the bottom plot of the Figure 4.12, the high frequency boost force vibration caused by the pressure ripple is detectable, while this high frequency vibration in Figures 4.13 and 4.14 is not obvious because of the scale of the plots. Figures 4.16 and 4.17 also illustrate the pressure ripple.

Owing to the flexibility of the mathematical steering system developed here, different kinds of steering efforts can be input to the model and the different responses can be obtained and compared. Figure 4.17 shows the responses of the steering system when a ramp torque input is applied on the steering wheel. At time zero, the steering system is neutral and the displacements and velocities of all the steering components are zeros. From time zero to 0.8 second, the torque on the steering wheel increases from 2 Nm to 4 Nm, and the torque is kept at 4 Nm after that. The rotational velocity of the ten vane steering pump is 1200 rpm (20 Hz).

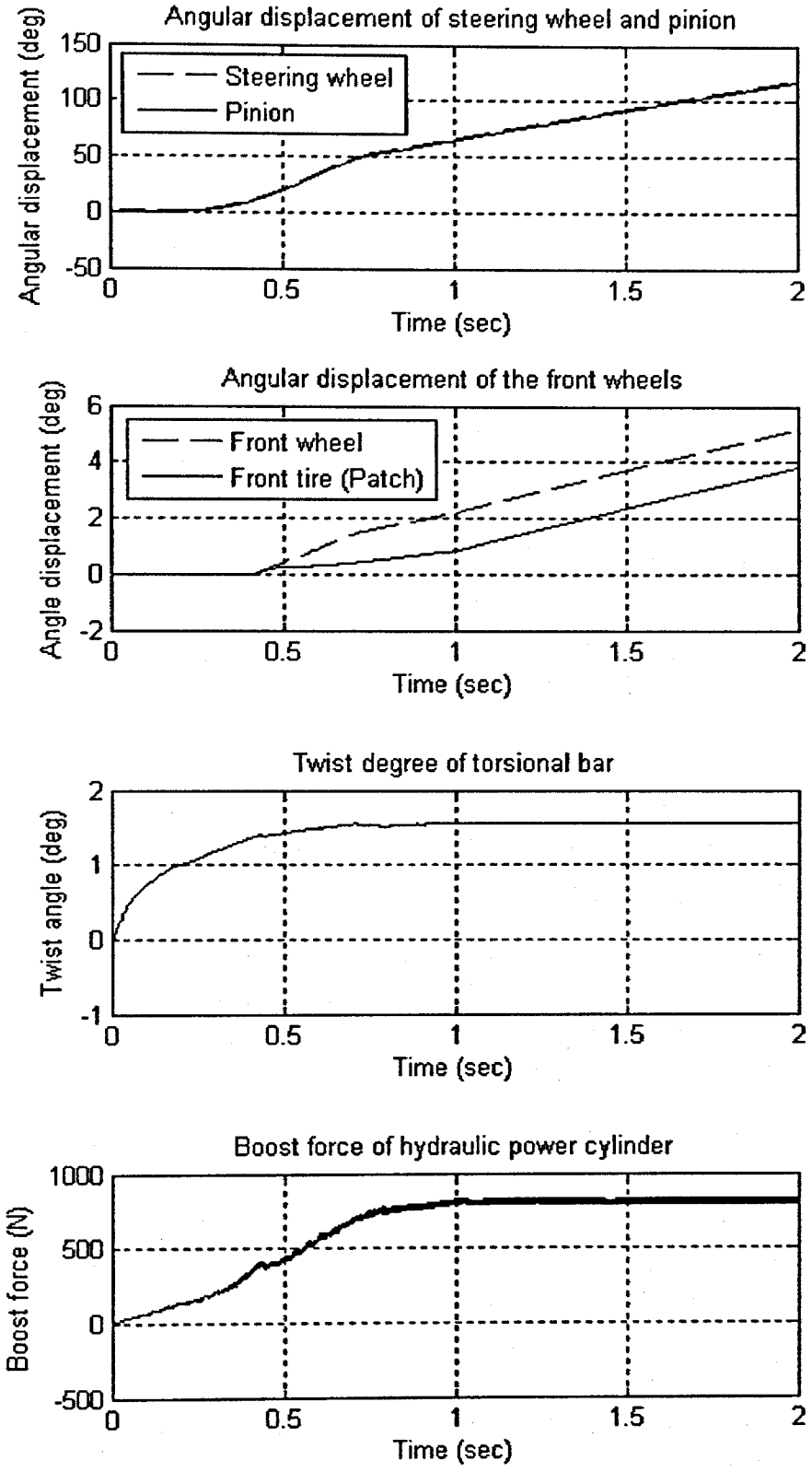

Figure 4.16 Responses of hydraulic power steering system

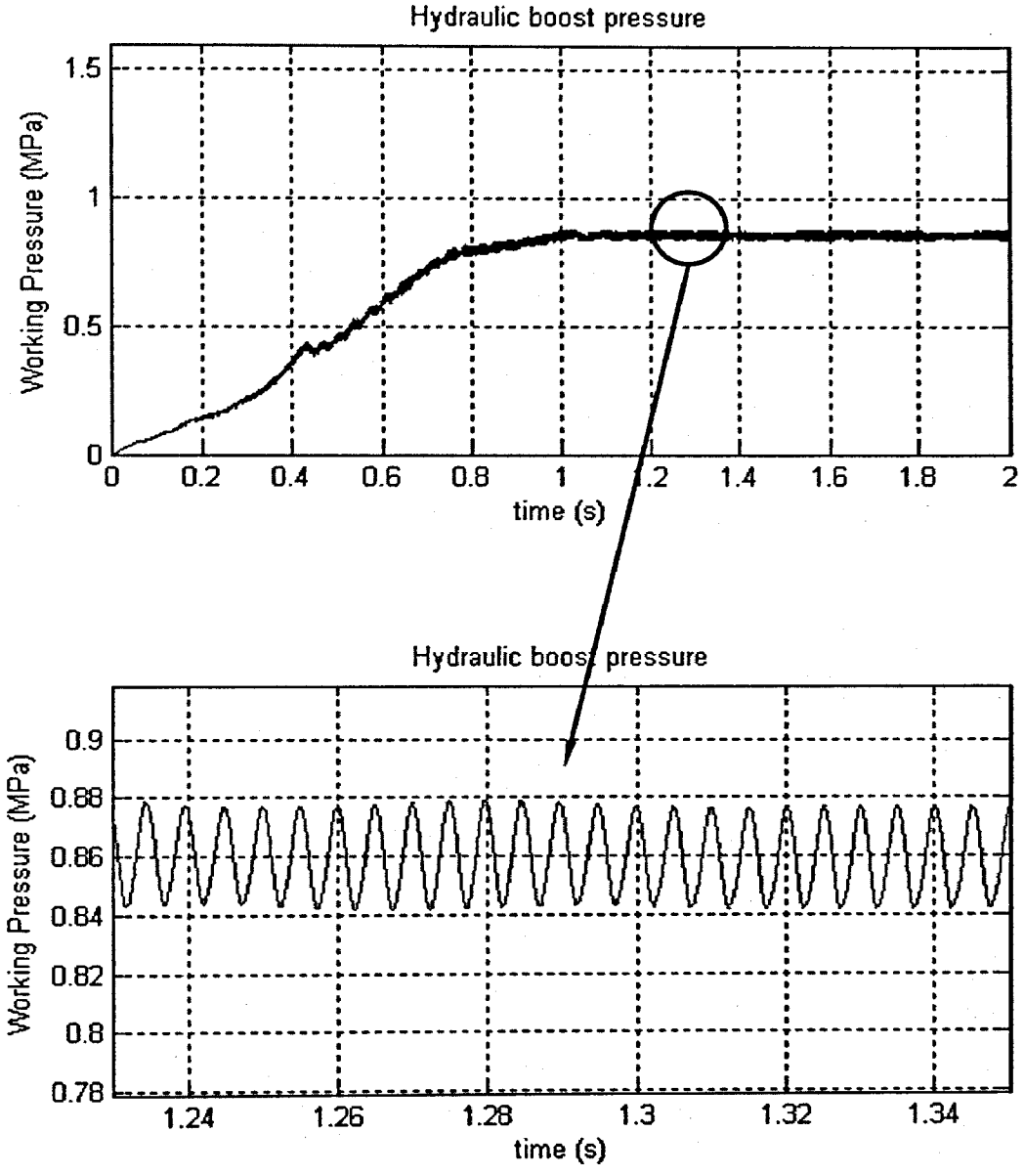

Figure 4.17 Pressure ripple in hydraulic power cylinder

Different from the top plots of Figures 4.12, 4.13 and 4.14, the top plot of Figure 4.16 shows that the angular velocities of the steering wheel and the pinion are not constants under the ramp torque input. According to Figure 4.16, the rise of the twist angle of the torsional bar is slower and smoother than that when there is a constant angular velocity steering input. Therefore, it takes a longer time for the cylinder pressure to build up enough to overcome the friction forces, and the front wheels only have noticeable movement after about 0.44 second. The bottom graph of Figure 4.16 does not show the low frequency steering shudder as the twist angle of the torsional bar is still at a low value. But the plot shows the high frequency boost force vibration.

In order to illustrate the pressure ripple more clearly, Figure 4.17 is used to show the pressure change in the hydraulic cylinder. From time zero to 1 second, the pressure increases from zero to about 0.86 MPa, and then remains constant. This response provides a better chance to observe the high frequency pressure ripple than the response under a quick angular velocity input which incurs the steering shudder. One part of the steady response of the pressure is enlarged in Figure 4.17 and the high frequency pressure ripple is clearly visible.

In this research, the characteristics and the effects of the high frequency pressure ripple are paid attention. Based on the above mentioned numerical solution, the simulation is carried out to obtain the transient response of the power steering system under a ramp steering input and different steering pump speeds. As in the previous analysis, the torque on the steering wheel increases from 2 to 4 Nm in the first 0-0.8 second and the responses of the system, such as boost force fluctuations and vibrations of the mechanical components, are obtained.

Figure 4.18 shows the dynamic boost force in the hydraulic cylinder resulting from the steering input with respect to pressure ripple frequencies. The plot is a three-dimension mapping. One of the dimensions is time. The other is the pressure ripple frequency, which is ten times of the pump speed because the ten vane steering pump is used in the system. The remaining dimension is the vibration amplitude of the boot force. In this simulation, the system responses within a 0.1 second time period are plotted to show the ripple clearly, and the responses from 1.6 to 1.7 second are chosen to avoid the rise

of the boost force before 1.0 second and to get the steady state response of the system. The frequencies of the pressure ripple from the pump are swept from 700 rad/s (111.41Hz) to 1200 rad/s (191.99Hz) to detect if resonant vibration occurs.

It can be noticed in the figure that the frequency of the dynamic boost force increases with the increase of the pressure ripple frequency. The amplitude of the dynamic boost force fluctuation reaches the maximum when the pressure ripple frequency is about 970 rad/s (154.38 Hz). In the previous free vibration analysis of the mechanical subsystem, the natural frequencies and the corresponding dominant components have been found. As the twist angle of the torsional bar is generated by the angular displacement difference of the pinion and the steering column and the angle controls the pressure fluid, the rotational displacements of the pinion and the steering column have the direct effects on the boost force. Shown in Figure 4.9, the pinion is the dominant component in the 175.57 Hz natural frequency, and in Figure 4.8, the steering column is the dominant component in the 137.31 Hz natural frequency. However, in Figure 4.18, there is no significant response either at 1103 rad/s (175.57 Hz) frequency or at 863 rad/s (137.31 Hz).

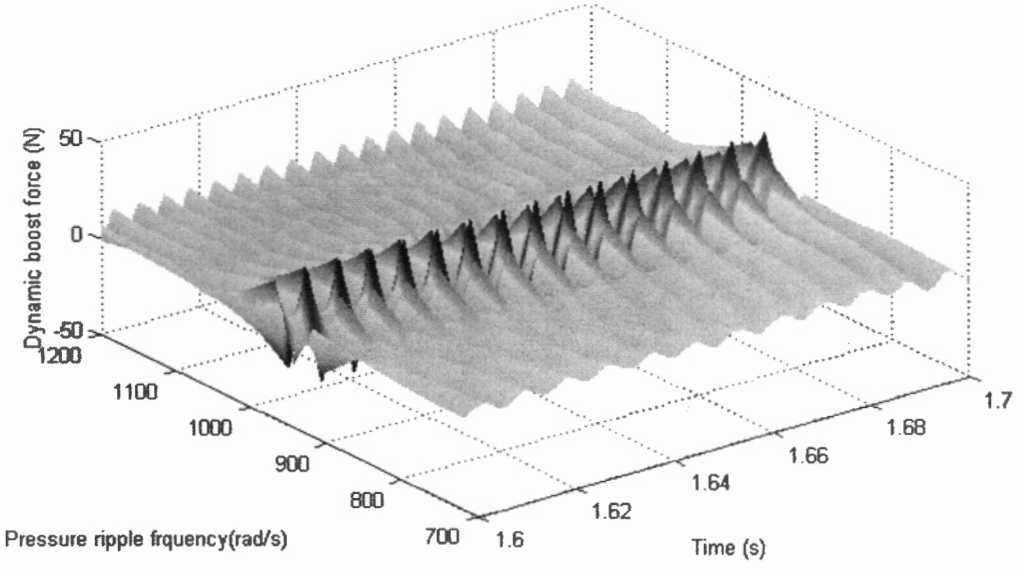

Figure 4.18 Dynamic boost force of the steering system

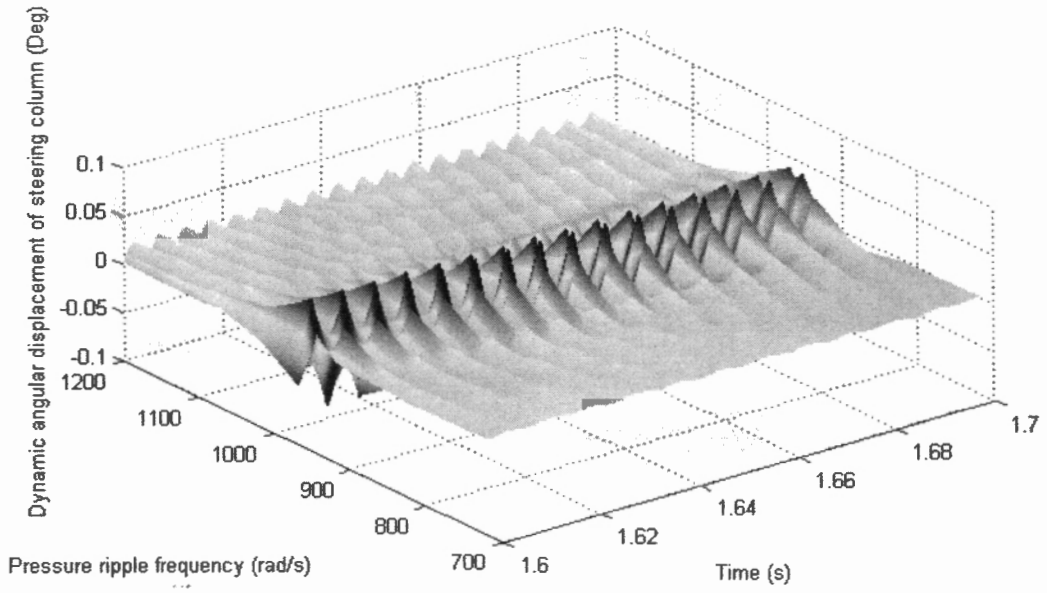

Figure 4.19 Dynamic angular displacement of the steering column

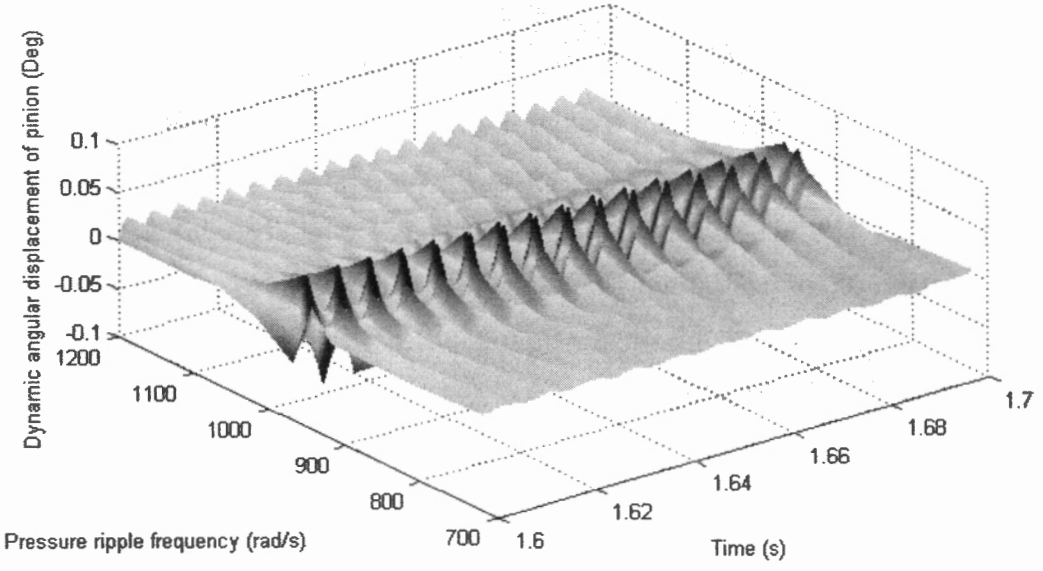

Figure 4.20 Dynamic angular displacement of pinion

To check the response of the steering column, the Figure 4.19 is obtained by the time domain calculation. The vertical axis of the plot shows the instantaneous angular displacement of the steering column under the same operating condition mentioned above. Similar to Figure 4.18, it shows that severe vibration of the steering column occurs at frequency about 970 rad/s (154.38 Hz). The steering column has no obvious vibration at about 137.31 Hz, although in the mechanical subsystem the steering column is the dominant component at 137.31 Hz natural frequency.

The response of the pinion is also calculated by the same method and is illustrated in Figure 4.20. It also shows that the resonance occurs at frequency about 970 rad/s (154.38 Hz) and there is no evident of vibration at the natural frequency, 175.57 Hz, of the mechanical subsystem to which the pinion is the dominant component.

Both the transient boost force in the hydraulic cylinder and the angular displacements of the steering column and the pinion under a ramp steer input show that resonant vibration occurs when the pressure ripple frequency is about 154.38 Hz. This clearly indicates that the nature of the dynamics in the hydraulic system and the mechanical subsystem are very similar, if indeed the same. On the other hand, from the free vibration analysis of the mechanical subsystem, there is no natural frequency at 154.38 Hz. This leads to the conclusion that while the frequency of the shudder phenomenon is correctly found by the free vibration analysis of the mechanical subsystem, the model of the mechanical subsystem does not represent the dynamic coupling between itself and the hydraulic subsystem in the free vibration analysis. Nevertheless, the transient responses of the mechanical and the hydraulic subsystems can be obtained to some extent through a numerical solution scheme in which the dynamic coupling between the two subsystems are taken into account as changing operating conditions and applied external forces respectively.

4.3.3 Summary

Based on the mathematical model introduced in the last chapter, the free vibration analysis of the mechanical subsystem and the transient vibration analysis of the whole steering system are conducted in this chapter.

In the free vibration analysis of the mechanical subsystem, the natural frequencies and their corresponding dominant components are found. Also, the time domain response of the steering system under different inputs are obtained and analysed. The steering shudder phenomenon is captured by the time domain calculation scheme. Compared to the free vibration analysis, it shows that while the steering shudder problem is the pressure vibration of the working fluid, the mechanical components are the main sources of the vibration and the free vibration of the mechanical subsystem can capture the frequency of the shudder.

The high frequency pressure ripple is also represented by the time domain calculation. However, a resonance of the pressure ripple occurs at frequency about 154.38 Hz which is neither the natural frequency of the steering column nor the natural frequency of the pinion. Furthermore, both the responses of the steering column and the pinion show the resonance at 154.38 Hz despite their natural frequencies being 137.31 Hz and 175.57 Hz respectively. Therefore, it is believed that the coupling of the mechanical and hydraulic subsystems generates the frequency offset.

This research includes all the important components of the steering system and it provides a more comprehensive and accurate model than previous ones [Ferries et al (1997), Neureder (2002)]. Owing to the model developed here, the dynamic characteristics of the mechanical subsystem of the steering system, such as the natural frequencies and the corresponding mode shapes, are investigated for the first time. In the time domain analysis, this research also obtains more detailed responses of the system than the previous investigation [Matsunaga et al (2001)]. The effects of the frequencies of the pressure ripple are presented. Furthermore, the comparison of the free vibration analysis of the mechanical subsystem and the time domain analysis discovers the existence of the coupling effect between the mechanical and hydraulic subsystems, which has not been clearly studied before.

The limitation of the mechanical subsystem model developed in this chapter is that it could not investigate the dynamic characteristics of the whole hydraulic steering system, hence the coupled frequencies and mode shapes of the system could not be presented. The work in the next chapter overcomes this shortcoming.

CHAPTER 5 FREQUENCY DOMAIN ANALYSIS

5.1 Introduction

In last chapter, free vibration analysis of the mechanical subsystem is conducted. The transient responses of the steering system under a ramp steer input with a pump speed varying within a range are obtained through the numerical integration, and the critical pump speeds, at which significant vibration (such as pressure ripple) takes place and have been identified. While the outcome of last chapter helps the understanding of the dynamics of the hydraulic power steering system, a more thorough investigation for the coupling effect in the system is needed.

In this chapter, an innovative study of the dynamics of an integrated power steering system that consists of both the mechanical and hydraulic components is presented. The frequency domain analysis firstly divides the hydraulic power steering system into two subsystems, i.e., the mechanical subsystem and the hydraulic subsystem, and then the two subsystems are integrated together into a complete model of the whole steering system.

By adopting the transfer matrix method for modelling the hydraulic subsystem and including the pressures of the fluid circuits into the state vector, the boundary conditions are applied at the cylinder/piston unit and the spool valve to determine the model of the integrated system. The state space system model developed here clearly presents the coupling of the mechanical subsystem and hydraulic subsystem. The natural frequencies and modal shapes of the complete steering system are then determined using a root searching numerical scheme. The results obtained from transient analysis in both time domain and frequency domain analyses are discussed and the dynamic coupling effect of the mechanical and hydraulic subsystems is illustrated. Conclusions are given in the end of the chapter.

5.2 Mathematical model of the mechanical subsystem for frequency domain analysis

The mechanical subsystem model used for the frequency domain analysis is basically the same as that presented in Section 4.2. The equations of motion in the form of second order differential equations are transformed to a state space representation form shown below;

$$[\dot{X}]=[A][X]+[B][F] \tag{5.1}$$

where,

$$[\dot{X}]=\begin{bmatrix}\dot{u}\\ \ddot{u}\end{bmatrix}_{24\times 1},$$

$$[A]=\begin{bmatrix}0 & I\\ -M^{-1}K & -M^{-1}C\end{bmatrix}_{24\times 24},$$

$$[X]=\begin{bmatrix}u\\ \dot{u}\end{bmatrix}_{24\times 1},$$

$$[B]=\begin{bmatrix}0\\ -M^{-1}\end{bmatrix}_{24\times 12},$$

and $[F]_{12\times 1}$ is the vector of external forces and torques. In matrix $[A]$, I is an identity matrix.

In the calculation of the coupled system matrix of the whole steering system, the system matrix of the mechanical subsystem $[A]$ will be combined with the transfer matrix of the hydraulic subsystem.

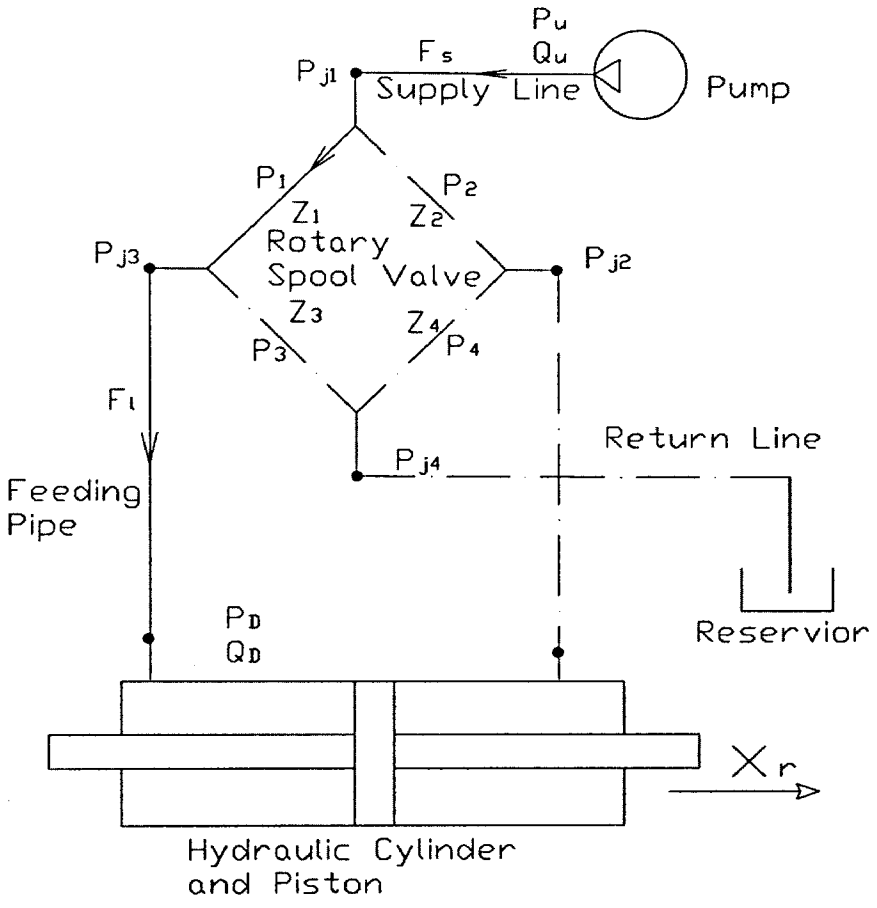

Fig. 5.1 Schematic of fluid circuit of hydraulic power steering system

5.3 Mathematical model of the hydraulic subsystem for frequency domain analysis

Figure 5.1 shows the schematic of the fluid circuit of the hydraulic steering system, including pump, supply line, rotary spool valve, feeding pipes, hydraulic cylinder and piston. The solid lines and arrows show the high pressure circuit and the flow direction

respectively. The dashed line shows the low pressure circuit. With the same reasons in the time domain simulation, only the high pressure line is considered in this analysis.

The one-dimensional linear resistance compressible flow model [Stecki and Davis (1986)] is adopted to obtain the transfer matrix of the individual hydraulic components. In Figure 5.1, F_S is the field matrix of the supply line, which consists of three components, including two steel pipes and a flexible hose,

$$F_S = T_3 \cdot T_2 \cdot T_1 \tag{5.2}$$

where T_1, T_2 and T_3 are the transfer matrixes of the steel pipe connecting the pump, the flexible hose and the steel pipe connecting the valve respectively. It should be noted that F_S is same as T_{Supply} in Equation (3.19).

In order to analyse the impedance characteristics of the four-way open centre control valve, point joint matrix is calculated.

The analysis method for branching hydraulic systems developed by Wylie and Streeter (1993) is adopted to obtain the transfer matrixes of the rotary spool valve. In Figure 5.2, the junction of the valve is enlarged and the three junctions are named as Di, Uk and Dj respectively.

Due to continuity of the fluid,

$$Q_{Uk} = Q_{Di} - Q_{Dj} \tag{5.3}$$

where, Q is the flow rate. The above equation can be written as

$$Q_{Uk} = Q_{Di} - \frac{P_{Dj}}{Z_2} \tag{5.4}$$

where P_{Dj} is the pressure at Dj, and Z_2 is the impedance of orifice 2.

At this junction, the pressures at the three branches are the same:

$$P_{Uk} = P_{Di} = P_{Dj}. \tag{5.5}$$

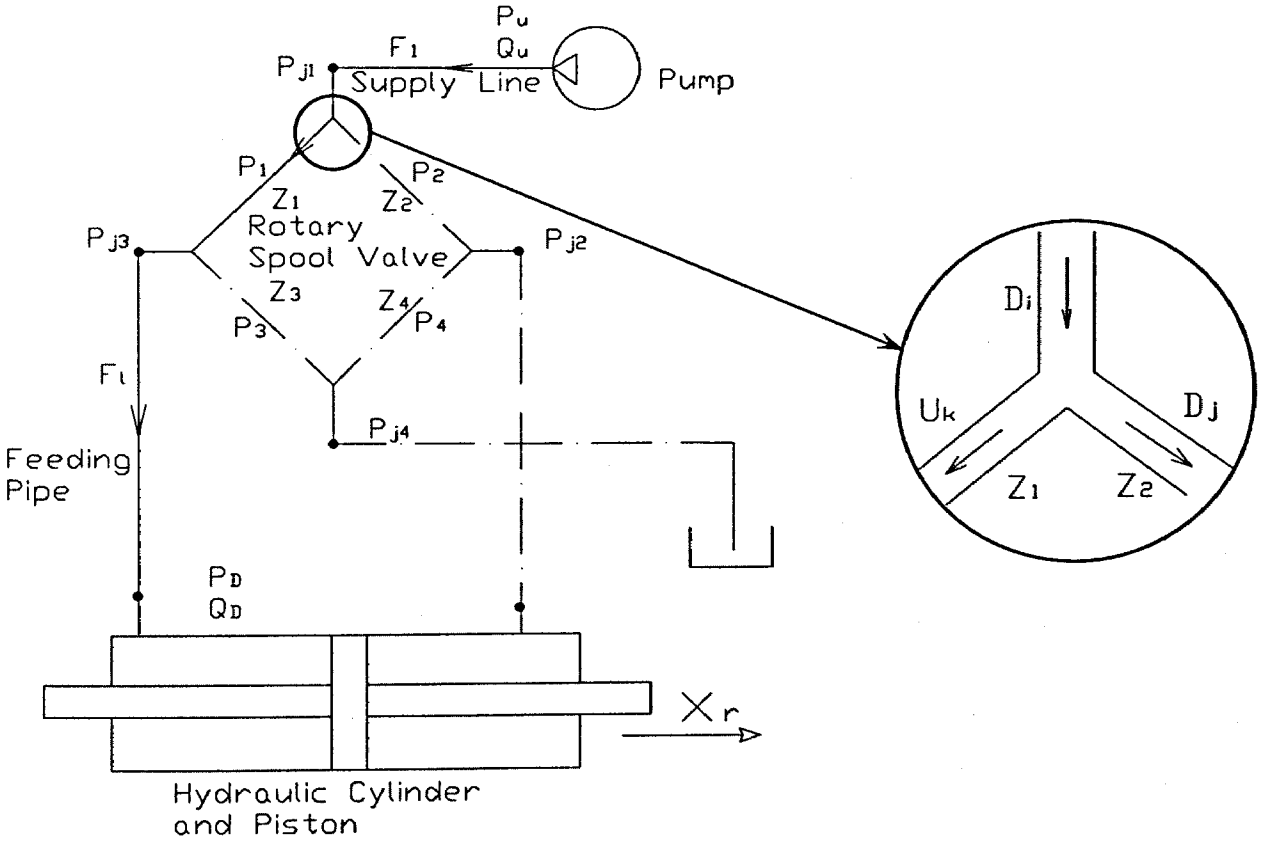

Figure 5.2 Junction of the rotary spool valve.

Substituting Equation (5.5) into Equation (5.4), we have

$$Q_{Uk} = -\frac{P_{Di}}{Z_2} + Q_{Di} \tag{5.6}$$

Combining Equations (5.5) and (5.6) obtains

$$\begin{Bmatrix} P \\ Q \end{Bmatrix}_{Uk} = \begin{bmatrix} 1 & 0 \\ -\frac{1}{Z_2} & 1 \end{bmatrix} \begin{Bmatrix} P \\ Q \end{Bmatrix}_{Di} \tag{5.7}$$

This process is used to obtain the joint transfer matrixes of the valve, such as Equations (5.8) and (5.10).

Therefore, the joint point matrix of the valve is

$$P_{j1} = \begin{bmatrix} 1 & 0 \\ -\frac{1}{Z_2} & 1 \end{bmatrix} \tag{5.8}$$

where the Z_2 is the impedance of orifice 2.

Using the valve and orifice transfer matrix, P_1 is the point matrix of the valve,

$$P_1 = \begin{bmatrix} 1 & -\frac{2\overline{P}_0}{\overline{Q}} \\ 0 & 1 \end{bmatrix} \tag{5.9}$$

where $\overline{P}_0$ and $\overline{Q}$ are the average pressure and flow rate passing through orifice 1, respectively.

In Figure 5.2, P_{j3} is the joint point matrix of the valve and Z_3 is the impedance of orifice 3.

$$P_{j3} = \begin{bmatrix} 1 & 0 \\ -\dfrac{1}{Z_3} & 1 \end{bmatrix} \tag{5.10}$$

F_l is the field matrix of the left feeding pipe to the hydraulic cylinder.

$$F_l = T_l \tag{5.11}$$

where T_l is calculated using the general equation for a hydraulic pipe.

$$T_l = \begin{bmatrix} \cosh(rl) & -Z_c \sinh(rl) \\ -\dfrac{\sinh(rl)}{Z_c} & \cosh(rl) \end{bmatrix} \tag{5.12}$$

Since the hydraulic components which include the supply line, valve and feeding pipes, are connected serially, the output of one component is the input to the next component. Therefore, the transfer matrix method could be used in the study of the dynamic characteristics of the whole fluid circuit.

Combining Equations (5.2) to (5.11), it is shown,

$$\begin{Bmatrix} P_D \\ Q_D \end{Bmatrix} = F_l P_{j3} P_l P_{j1} F_S \begin{Bmatrix} P_U \\ Q_U \end{Bmatrix} \tag{5.13}$$

where, P_U and Q_U are the pressure ripple and flow ripple at the upstream end, and P_D and Q_U are pressure ripple and flow ripple at the downstream end respectively. In Equation 5.13, the impedance of the valve is constant, because at normal working conditions the change of the opening orifice areas is small and the calculation of the equation also shows that the effect of the variation of the valve impedance is limited.

Equation. (5.13) can be presented as transfer matrix form.

$$\begin{Bmatrix} P_D \\ Q_D \end{Bmatrix} = \begin{bmatrix} T_{11} & T_{12} \\ T_{21} & T_{22} \end{bmatrix} \begin{Bmatrix} P_U \\ Q_U \end{Bmatrix} \tag{5.14}$$

The hydraulic cylinder can be considered as an accumulator in the hydraulic system. Therefore the downstream pressure and flow rate has the following feature,

$$\frac{P_D}{Q_D} = Z_A \tag{5.15}$$

where Z_A is the impedance of the hydraulic power cylinder and it equals $\frac{j\beta}{V\omega}$.

For free vibration, $P_U = 0$. Therefore, the boundary conditions of the hydraulic system are determined and the downstream and upstream situations of the system can be written in the following form after combining Equations 5.14 and 5.15.

$$\begin{bmatrix} 1 & 0 & -T_{11} & -T_{12} \\ 0 & 1 & -T_{21} & -T_{22} \\ 1 & -Z_A & 0 & 0 \\ 0 & 0 & 1 & 0 \end{bmatrix} \begin{bmatrix} P_D \\ Q_D \\ P_U \\ Q_U \end{bmatrix} = 0 \tag{5.16}$$

Equation 5.16 can be written in general form.

$$[G][X] = 0 \tag{5.17}$$

where $[G]$ is the global matrix of the hydraulic subsystem and $[X]$ is the system variables.

$$[G]=\begin{bmatrix} 1 & 0 & -T_{11} & -T_{12} \\ 0 & 1 & -T_{21} & -T_{22} \\ 1 & -Z_A & 0 & 0 \\ 0 & 0 & 1 & 0 \end{bmatrix} \text{ and } [X]=\begin{bmatrix} P_D \\ Q_D \\ P_U \\ Q_U \end{bmatrix}.$$

To find the natural frequencies of the hydraulic subsystem in free vibration analysis, the determinant of the global matrix $[G]$ must be zero.

$$|G|=0 \tag{5.18}$$

Equation 5.18 is the characteristic equation of the hydraulic subsystem. If the complex root of the characteristic equation is called S_k, according to the concepts of the oscillatory flow, the real part of each S_k represents the decay factor, and the imaginary part of the root is the damped natural frequency.

During the calculation of Equation 5.18, two conditions are considered. First, it is obvious that there are an infinite number of roots for Equation 5.18 as the continuous hydraulic system has an infinite number degrees of freedom. This study only solved limited roots which are in the operating frequency range of a hydraulic power steering system. Second, the exact solution of Equation 5.18 has a numerical difficulty, and it is hard to obtain the exact roots to satisfy the equation. As a consequence, a root searching technique is employed to locate the roots of the equation.

In the locating process, a large range of decaying factors and natural frequencies are searched by using large steps at first. After the rough solutions are found, smaller steps are used to refine S_k.

Figure 5.3 shows that the roots of Equation 5.18 in real and imaginary areas, where the real value is from -400 to 400 and the imaginary value is from -3000 to 3000. The vertical axis is the absolute value of the determinant of G. It can be seen that the value of $\log(|\det(G)|)$ are minimal at positions of the 3 pairs of the conjugate roots. The

searching steps are refined to search every root in the local area. Details of the searching process are introduced in Subsection 5.5.1 .Figure 5.4 shows one local area, and the root of $S_k = -150.79 - 597.14j$.

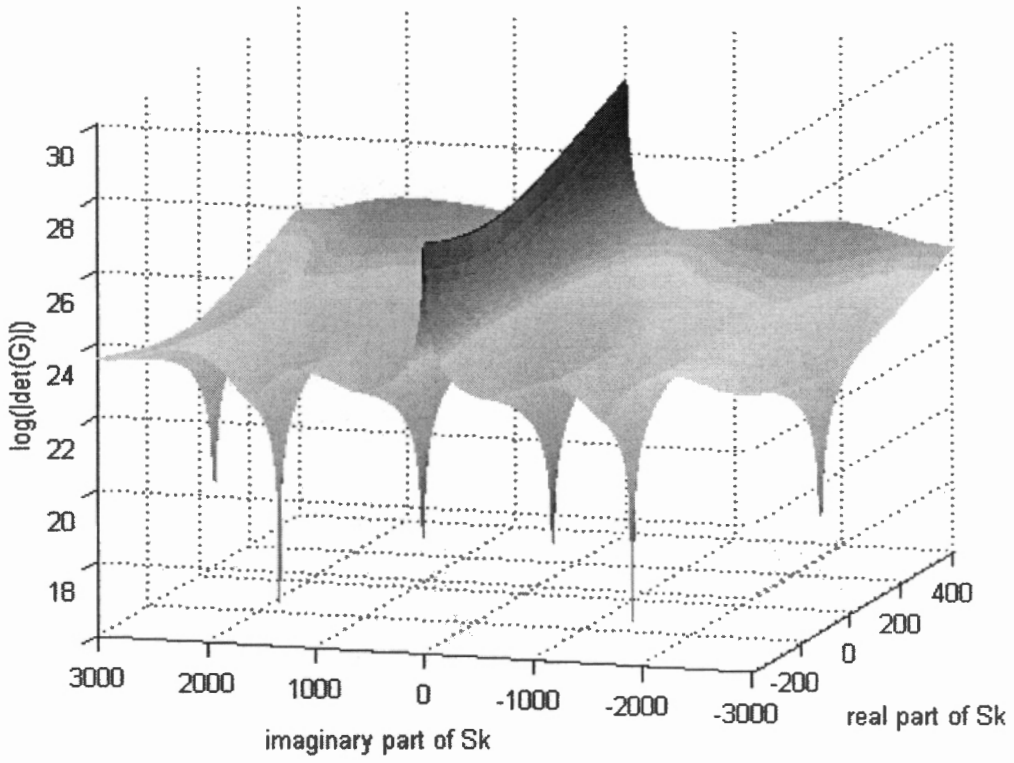

Figure 5.3 Root searching for the characteristic equation of the hydraulic subsystem

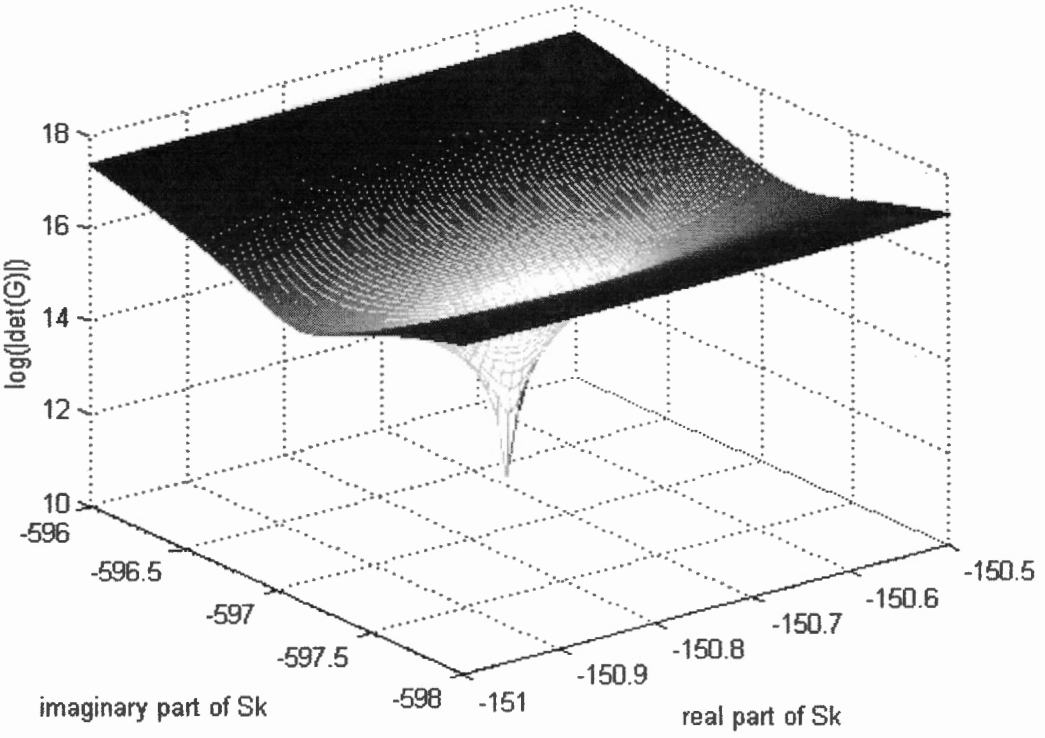

Figure 5.4 Detail of root searching for the characteristic equation of the hydraulic subsystem

Table 5.1 lists the 3 pairs of conjugate complex roots of the characteristics equation of the hydraulic subsystem. It is found that the natural frequencies of the hydraulic subsystem (154.38 Hz) do not include the resonance frequency of the whole system obtained by the transient analysis. Therefore, it excludes the possibility that this resonance frequency is the natural frequency of the hydraulic subsystem. It reconfirms the claim in the last chapter that the coupling effect of the two subsystems generates the coupled frequency of the system (154.38 Hz). And this coupled frequency is different from the natural frequencies of the individual mechanical or hydraulic subsystems, which are shown in Table 4.2 and Table 5.1 respectively.

No.	$s_k = \sigma_k + \omega_k \cdot j$ in $\det\|G\| \approx 0$	Frequency (Hz) $\omega_k / 2\pi$
1	-150.79 ± 597.14j	95.04
2	-279.80 ± 1619.8j	257.80
3	-36.8 ± 2777.1j	441.99

Table 5.1 Complex roots of the characteristic equation of the hydraulic subsystem

5.4 Mathematical model of the whole steering system for frequency domain analysis

5.4.1 State space form of the hydraulic subsystem

To characterise the dynamics of the integrated power steering system, frequency domain analysis of the whole system needs to be carried out to determine the natural frequencies and their corresponding modes. In this section, a dynamic model coupling the mechanical subsystem and the fluid circuit and its solution are developed for the frequency domain analysis.

The state space form equations of the mechanical subsystem are obtained in Section 5.2; and the transfer matrix method has been adopted to develop a global matrix to represent the hydraulic subsystem in frequency domain in Section 5.3. In this section, an innovative solution transforming the global matrix of the hydraulic subsystem to the state equation form is developed and it paves the way to couple the hydraulic subsystem with the mechanical subsystem in the frequency domain analysis.

Equation (5.14) can be shown in impedance matrix form:

$$\begin{Bmatrix} P_D \\ P_U \end{Bmatrix} = \begin{bmatrix} Z_{11} & Z_{12} \\ Z_{21} & Z_{22} \end{bmatrix} \begin{Bmatrix} Q_D \\ Q_U \end{Bmatrix} \tag{5.19}$$

The relationship of pressure and flow rate in the cylinder is governed by the following equation,

$$\dot{P}_D = \frac{2\beta(Q_D - A_P\dot{x}_P)}{V} \tag{5.20}$$

Rearranging Equation (5.20) obtains

$$Q_D = \frac{V}{2\beta}\dot{P}_D + A_P\dot{x}_P \tag{5.21}$$

Substituting Equations (5.21) into (5.19), we get

$$\begin{Bmatrix} P_D \\ P_U \end{Bmatrix} = \begin{bmatrix} Z_{11} & Z_{12} \\ Z_{21} & Z_{22} \end{bmatrix} \begin{Bmatrix} \frac{V}{2\beta}\dot{P}_D + A_P\dot{x}_P \\ Q_U \end{Bmatrix} \tag{5.22}$$

Therefore from Equation (5.22), we have

$$P_D = Z_{11}\frac{V}{2\beta}\dot{P}_D + Z_{11}A_P\dot{x}_P + Z_{12}Q_U \tag{5.23}$$

After rearranging Equation (5.23), we have

$$\dot{P}_D = \frac{2\beta}{Z_{11}V}P_D - \frac{2\beta}{V}A_P\dot{x}_P - \frac{Z_{12}}{Z_{11}}\frac{2\beta}{V}Q_U \tag{5.24}$$

From Equation (5.22), we also have

$$P_U = Z_{21}\left(\frac{V}{2\beta}\dot{P}_D + A_P\dot{x}_P\right) + Z_{22}Q_U \tag{5.25}$$

and from Equation (5.14), it can be obtained

$$P_D = T_{11}P_U + T_{12}Q_U \tag{5.26}$$

Differentiating Equation (5.26) obtains

$$\dot{P}_D = T_{11}\dot{P}_U + T_{12}\dot{Q}_U \tag{5.27}$$

Substituting Equation (5.27) into Equation (5.25), we have

$$P_U = Z_{21}\left[\frac{V}{2\beta}(T_{11}\dot{P}_U + T_{12}\dot{Q}_U) + A_P\dot{x}_P\right] + Z_{22}Q_U \tag{5.28}$$

Rearranging Equation (5.28), we have

$$\dot{P}_U = \frac{2\beta}{V}\frac{1}{T_{11}Z_{21}}P_U - \frac{2\beta}{V}\frac{A_P}{T_{11}}\dot{x}_P - \frac{T_{12}}{T_{11}}\dot{Q}_U - \frac{2\beta}{V}\frac{Z_{22}}{T_{11}Z_{21}}Q_U \tag{5.29}$$

In summary, Equations (5.24) and (5.29) can be written in the following simplified form, and the state space equation form of the pressures in the hydraulic circuit is then obtained.

$$\dot{P}_D = C_1P_D + C_2\dot{x}_P + C_3 \tag{5.30}$$

$$\dot{P}_U = C_4P_U + C_5\dot{x}_P + C_6 \tag{5.31}$$

where, $C_1 = \frac{2\beta}{V}\frac{1}{Z_{11}}$,

$$C_2 = -\frac{2\beta}{V} A_P,$$

$$C_3 = -\frac{2\beta}{V}\frac{Z_{12}}{Z_{11}} Q_U,$$

$$C_4 = \frac{2\beta}{V}\frac{1}{T_{11}Z_{21}},$$

$$C_5 = -\frac{2\beta}{V}\frac{A_P}{T_{11}}$$

and $C_6 = -\frac{T_{12}}{T_{11}}\dot{Q}_U - \frac{2\beta}{V}\frac{Z_{22}}{T_{11}Z_{21}} Q_U$.

5.4.2 Coupled system matrix of the whole steering system

It can be noticed that the piston velocity $\dot{x}_P$ in Equations (5.30) and (5.31) is one of the state variables defined in Equation (5.1), and the force applied to the piston can be represented by the product of the operating pressure P_D and the area of the piston A_P.

In order to obtain a clear form of the coupled system matrix, four sub-matrices are developed initially:

$$S1 = \begin{bmatrix} 0_{3\times1} & 0_{3\times1} \\ -A_P & 0 \\ A_P & 0 \\ 0_{7\times1} & 0_{7\times1} \end{bmatrix}_{12\times2},$$

$$S2 = \begin{bmatrix} 0_{1\times4} & C_2 & 0_{1\times7} \\ 0_{1\times4} & C_5 & 0_{1\times7} \end{bmatrix}_{2\times12},$$

$$S3 = \begin{bmatrix} C_1 & 0 \\ 0 & C_4 \end{bmatrix}_{2\times2},$$

and $S4 = \begin{bmatrix} C_3 \\ C_6 \end{bmatrix}_{2\times1}$,

where C_1, C_2,..., C_6 have been shown in Equations (5.30) and (5.31).

Therefore, the state space form of the equations of motion for the integrated hydraulic power steering system can be obtained by combining Equations (5.1), (5.30) and (5.31). It results in

$$[\dot{Y}] = [J][Y] + [W][D], \tag{5.32}$$

where

$$[\dot{Y}] = \begin{bmatrix} \dot{X} \\ \dot{P}_D \\ \dot{P}_U \end{bmatrix}_{26\times1},$$

$$[J] = \begin{bmatrix} 0 & I & 0 \\ -M^{-1}K & -M^{-1}C & S1 \\ 0 & S2 & S3 \end{bmatrix}_{26\times26},$$

$$[Y] = \begin{bmatrix} X \\ P_D \\ P_U \end{bmatrix}_{26\times1},$$

$$[W] = \begin{bmatrix} 0 & 0 & 0 \\ 0 & M^{-1} & 0 \\ 0 & 0 & I \end{bmatrix}_{26\times26},$$

and $[D] = \begin{bmatrix} 0 \\ F \\ S4 \end{bmatrix}_{26\times1}$.

Equation (5.32) governs the dynamics of the integrated power steering system consisting of both the mechanical and hydraulic subsystems. The system matrix $[J]$ includes the dynamic coupling between the two subsystems. In the following section, the dynamic characteristics of the steering system are obtained from matrix $[J]$.

5.5 Frequency domain analysis of the whole system

5.5.1 Analysis of the integrated system matrix

The frequency domain analysis is conducted in this part using the coupled system matrix developed in the last section. Also, for designing a vibration free hydraulic power steering system, frequency domain analysis of the whole system needs to be carried out to optimise the system parameters within the specified operating range. The sensitivity analysis of certain key elements may need to be performed to tune the system for achieving best performance.

Keeping the parameters of the typical power steering system used in Chapter 4 unchanged, the natural frequencies and corresponding modes of the hydraulic power steering system are determined and discussed in this section. Based on the one-dimensional linear resistance compressible flow model adopted in Chapter 3, the hydraulic circuit is a pump speed dependent system and the coefficients in Equations (5.30) and (5.31) include complex frequencies. Therefore, the system matrix $[J]$ in Equation (5.32) is also a pump speed-dependent matrix and the eigenvalues and eigenvectors of the integral system can not be determined using the usual eigen analysis method from the system matrix directly. A root searching technique is therefore developed for this analysis and described in detail as follows.

Theoretically, the system natural frequency is a complex number, i.e., $\lambda = \sigma + \omega \cdot j$, which satisfies Equation (5.33). The real part σ relates to the energy dissipation level and the imaginary part ω is the circular natural frequency [Wylie and Streeter (1993)].

$$\det|J - \lambda \cdot I| = 0 \tag{5.33}$$

'det' means the determinant, J is the system matrix and I is an identity matrix with the same dimension as matrix $[J]$.

To display the minima of $\det|J-\lambda\cdot I|$, the determinant values are computed and plotted against the real and imaginary parts of λ in a 3D coordinate system. Since the exact roots of Equation (5.33) are difficult to obtain numerically, the approximate eigen frequencies are acceptable if their corresponding values of $\det|S-\lambda\cdot I|$ approach a minimum value in the vicinity of λ. Also, only limited ranges of real and imaginary parts of λ are searched in the computation. Although the number of the theoretical roots of Equation (5.33) is infinite as the steering system consists of the continuous hydraulic circuit subsystem, Drew *et al.* (1994) have suggested that the frequencies of detectable noise in hydraulic steering systems are lower than 1000 Hz.

In the root searching process, at first, the approximate values of σ and ω are substituted into Equation (5.33), the values of $\det|J-\lambda\cdot I|$ are plotted, and the approximate locations of λ are found. Then, based on the inital searching, the roots are further refined by searching in a small area and with higher solutions of σ and ω.

In the inital searching, the real part of the root is searched from -200 to 200 with a step length of 1, and the imaginary part of the root is searched from -2000 to 2000 with a step length of 1. The values of $\log(|\det(S-\lambda\cdot I)|)$ are determined and the approxmiate values of the roots can be found.

Then, the rough results can be searched in local areas with higher resolutions one by one. Figure 5.5 is a 3D plot showing one complex eigen value within a limited area. In this plot, the real parts of λ range from -6.0 to -5.2 with a resolution of 0.01, and imaginary parts range from -970 and -968 with 0.01 resolution. The vertical axis is the value of $\log|\det(J-\lambda\cdot I)|$. The minimum value corresponds to frequencies λ= -5.62 - 969.09j. (There is also a conjugated complex root of -5.62 + 969.09j in the area where the real parts of λ ranges from -6.0 to -5.2 and the imaginary parts ranges from 968 to

970.) This indicates one natural vibration frequency of the coupled steering system at 969.09 rad/s (154.24 Hz).

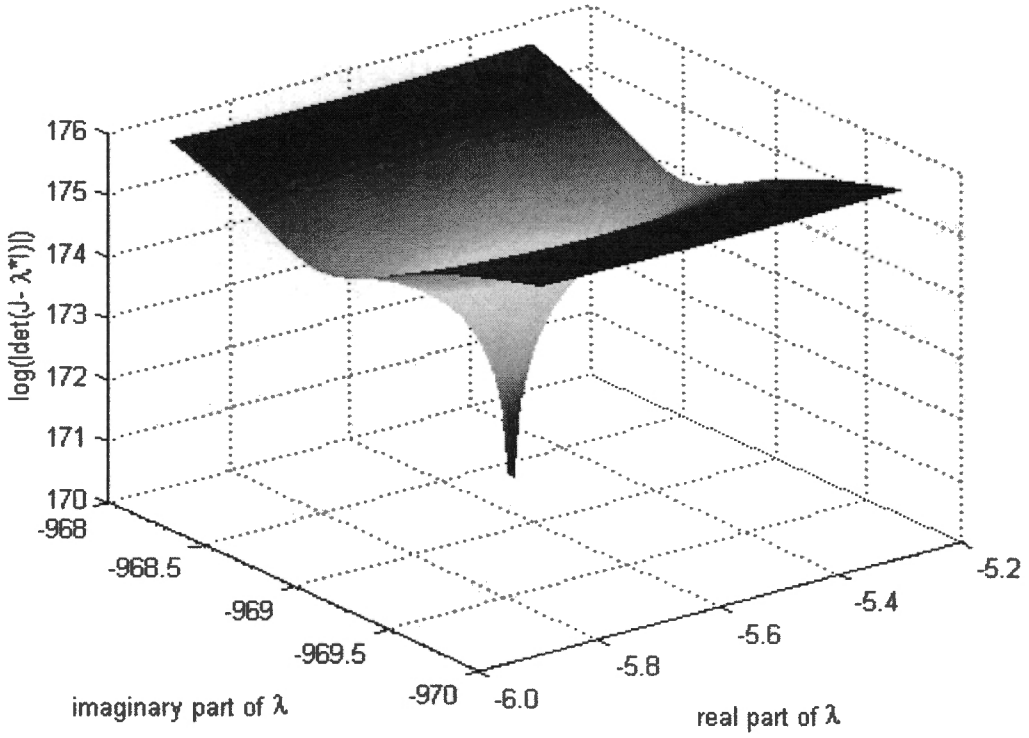

Figure 5.5 3D plot of values of $\det|J-\lambda\cdot I|$ in a limited search area

Table 5.2 Roots of $\det|J-\lambda\cdot I|=0$

No.	$\lambda=\sigma+\omega\cdot j$ in $\det\|J-\lambda\cdot I\|\approx 0$	Frequency (Hz) $\omega/2\pi$
1	-0.01 ± 15.37j	2.45
2	-0.18 ± 134.80j	21.45
3	-13.80 ± 382.11j	60.81
4	-0.01 ± 457.71j	72.85
5	-0.01 ± 467.60j	74.42
6	-75.13 ± 688.43j	109.57
7	-5.62 ± 969.09j	154.24
8	-105.54 ± 1683.04j	267.86
9	-45.35 ± 3169.79j	504.49

Table 5.2 shows the roots of $\det|J-\lambda\cdot I|=0$. In this table, the frequencies lower than 100 Hz are very close to the mechanical subsystem's natural frequencies in Table 4.2. This indicates that these system frequencies are dominated by the dynamics of the mechanical subsystem. The frequencies at No. 6-9 in Table 5.2 are the frequencies coupled by the hydraulic subsystems dynamics and are much higher than most of the frequencies of the mechanical subsystem.

The positions of the roots on the complex plane are shown in Figure 5.6. The horizontal axis is the value of the real part, and the vertical axis is the value of the imaginary part. From the figure, it can be seen that all the roots are on the left side of $x=0$ line because all the real parts of the roots are negative. This indicates the system is a stable system.

The different characteristics of these roots are also found in the figure. Three coupled frequencies, which are No. 6, 8 and 9 frequencies in Table 5.2, are far from the vertical axis of the coordinates whereas the other frequencies are relatively close to the origin. The details around the origin which is enclosed by an ellipse in Figure 5.6 is enlarged and shown in Figure 5.7. As can be seen in Figure 5.7, most of the frequencies dominated by the mechanical components are very close to the $x=0$ line due to the small absolute values of the real parts which indicate small damping effects of the mechanical components.

It is interesting that the resonance frequency of the time domain simulation (about 154 Hz) is found in the natural frequencies of the coupled steering system. In fact, the two natural frequencies of 127.31 Hz and 175.57 Hz at which the steering column and the pinion are the dominant components are given special attention in the root searching process. But, it is found that $\det|J-\lambda\cdot I|$ does not show local minimum values around these two mechanical subsystem natural frequencies no matter how small the search steps are. This result totally supports the analysis in the last chapter. In the time domain simulation, a resonance occurs at a frequency of about 154 Hz, which is neither the frequency of the mechanical component nor the frequency of the hydraulic

subsystem. It is believed that this is a natural frequency of the system which couples the mechanical and hydraulic subsystem.

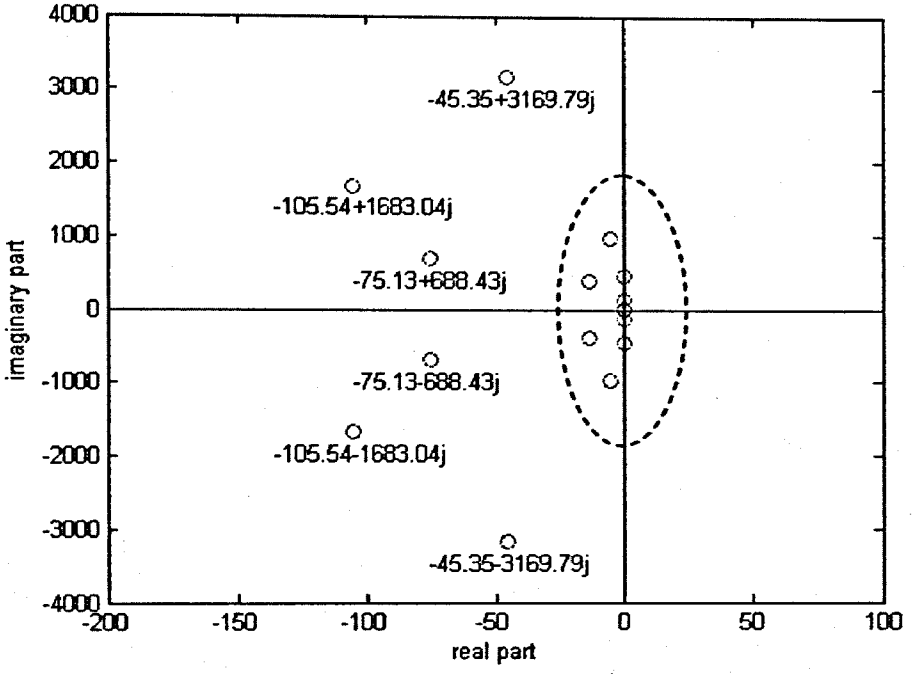

Figure 5.6 Roots of $\det|J-\lambda\cdot I|=0$

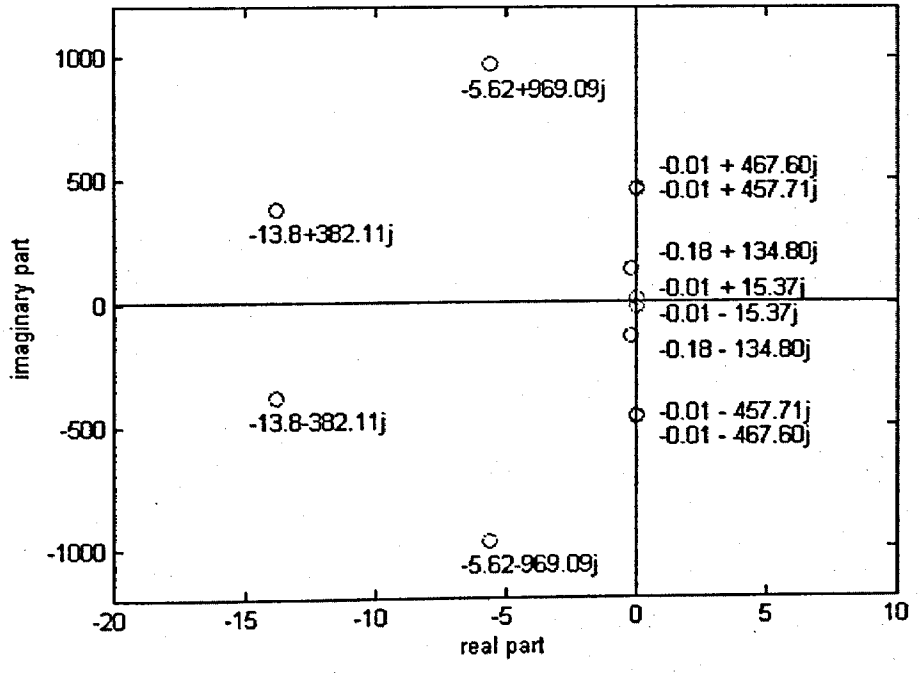

Figure 5.7 Roots of $\det|J-\lambda\cdot I|=0$

In order to investigate the system's characteristics further, each root of the $\det|J-\lambda\cdot I|=0$ is substituted to the system matrix $[J]$. Then all the parameters in $[J]$ are determined and the eigenvalues and eigenvectors can be obtained and checked.

For example, if one of the roots, say λ = -5.62 - 969.09j, is substituted into Equation 5.32, the system matrix $[J]$ is a determined matrix and is not a frequency-dependent matrix any more. Then the normal eigen calculation can be carried out and the eigenvalues and eigenvectors can be obtained. It is found that one of the eigenvalues of the determined system matrix is about -5.62 - 969.09j which confirms the calculation of the root searching scheme, whereas other eigenvalues are different from the values in Table 5.2 because only the characteristics of -5.62 - 969.09j is brought into the determined matrix.

The normalised eigenvectors are also obtained from the determined system matrix. Figure 5.8 shows the mode shapes of the steering system corresponding to the natural frequency of 154.28 Hz (969.37 rad/s). This natural frequency is obtained from the determined system matrix and is very close to the root searching result of 969.09 rad/s. The eigenvectors of matrix $[J]$ include the displacement vectors of the mechanical components and the pressure ripple vectors, but only the mode shapes of the mechanical components are shown in Figure 5.8 as the responses of the pressure ripples can not be compared to the displacements.

It must be noted that the meaning of Figure 5.8 is different to the meanings of Figures 4.1 to 4.11 although they appear to be the same. The mode shapes in Figure 5.8 are of the whole steering system which couples the mechanical and hydraulic subsystems, whereas Figures 4.1 to 4.11 only show the dynamic characteristics of the mechanical subsystem itself. In Figure 5.8, the steering column and pinion are the dominant components at the same time. This is different from the results of Figures 4.8 and 4.9. Compared to the mode shape figures of the mechanical subsystem, Figure 5.8 clearly illustrates the characteristics of the whole steering system and shows the coupling effects of the mechanical subsystem and the hydraulic subsystem. It also agrees with the time domain analysis.

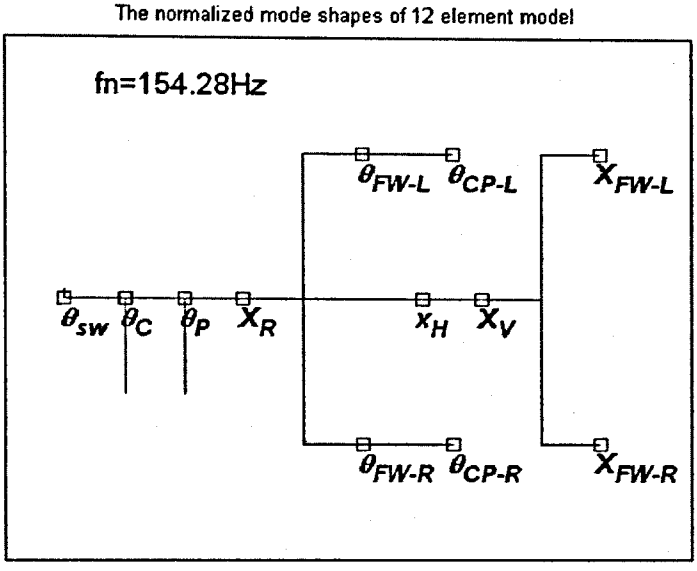

Figure 5.8 Mode shapes at 154.28 Hz of the whole steering system

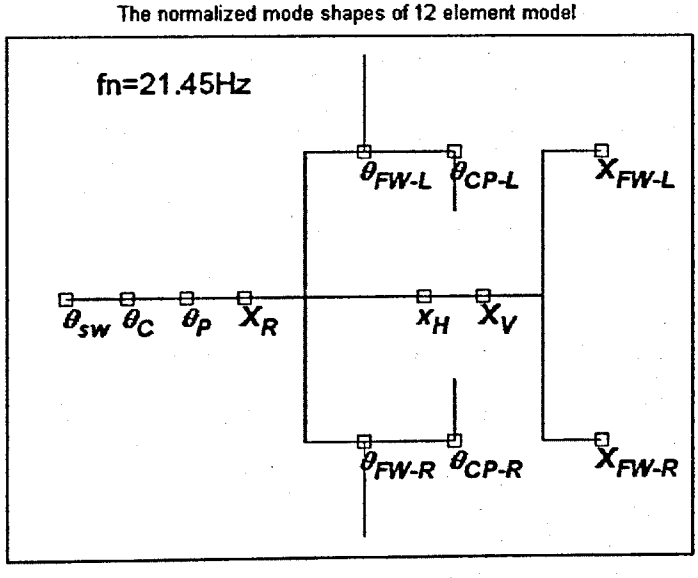

Figure 5.9 Mode shapes at 21.45 Hz of the whole steering system

As another example, the root of λ= -0.18 + 134.80j is substituted into Equation 5.32 to calculate the natural frequency and the mode shape of the system matrix. The results are similar to the previous analysis. One of the eigenvalues of the system matrix is same as the root -0.18 + 134.80j while others are different. Also the mode shapes are obtained and shown in Figure 5.9. Although this figure is generated from the whole system matrix $[J]$, it is same as Figure 4.3 showing the mode shapes of mechanical subsystem natural frequency of 21.45 Hz. This is because the mechanical components are the dominant components at this natural frequency, and the coupling effect of the hydraulic subsystem is negligible here.

5.5.2 Sensitivity study of the system matrix

The effects of some parameters of the system are investigated and the volume of the hydraulic cylinder and the area of the piston are discussed in this section as examples.

Keeping other parameters unchanged, the volume of the hydraulic cylinder is multiplied by the following factors: 0.7, 0.8, 0.9, 1.0, 1.1, 1.2 and 1.3. It means the volume of the cylinder changes from the 70% of the standard volume to the 130% of the standard volume. In a practical system, it could represent different lengths of the cylinder. For each of the seven different situations, the roots of $\det|J-\lambda\cdot I|=0$ are searched by the previous calculation method one by one. The values of the roots are listed in Table 5.3.

In the table, the numbers in the first row are the factors of the volume of the cylinder. The column under each number lists the first nine pairs of roots of the characteristic equation when the volume of the cylinder is multiplied by that factor. Naturally, the column under the factor 1.0 is same as that in Table 5.2 because the roots are obtained from the benchmark parameters.

As shown in the table, the first 5 pairs of roots are unchanged when the factor increases from 0.7 to 1.3. This is expected because the first pairs of roots show the frequencies dominated by the mechanical components. The variation of the volume of the hydraulic cylinder does not affect the dynamic characteristics of the mechanical

subsystem. It is also found that values of the 6th to 9th roots change. It indicates that the variation of the cylinder volume affects the characteristics of the hydraulic subsystem, therefore the variation has the influence on the coupling frequencies of the steering system.

Figure 5.10 shows the locus of the 6th root of Table 5.3 in the complex plane where the horizontal axis is the real part and the vertical axis is the imaginary part. Figure 5.11 shows the locus of the 8th roots and the locus of the 9th roots in the table are plotted in Figure 5.12. It can be seen from these three figures that all the imaginary parts of the roots, which represents the natural frequencies of the coupled system, decrease with the increase of the volume of the cylinder. The explanation of it is that the hydraulic cylinder in the steering system is basically a Helmholtz resonator which can be visualised as a spring-mass system. The natural frequency of the Helmholtz resonator can be calculated by the following formula [Wylie and Streeter (1993)].

$$\omega_n = \sqrt{\frac{\beta A}{\rho V L}} \tag{5.34}$$

where β is the effective bulk modulus of the fluid, A is the cross section area of the pipe of the resonator, ρ is the density of the fluid, V is the volume of the chamber and L is the length of the pipe of the resonator.

It is evident that the increase in the volume of the cylinder incurs decrease of the natural frequencies. Therefore, the variation of the volume of the cylinder has a negative correlation relationship with the natural frequencies of the system. On the other hand, the variations of the real parts of the roots in Figures 5.10 to 5.12 are not the same. It indicates the energy dissipation effects of the volume change on different natural frequencies are complex. It may increase the energy dissipation level at some system frequencies and decrease the level at other frequencies.

The variation of the piston area also influences the system. By performing a similar procedure of the volume of the cylinder, the piston area is multiplied by a factor ranging from 0.7 to 1.3. It means the piston area increases from 70% of the standard

value to 130% of the standard value. It must be noticed that, different in the volume of the cylinder, the change of the piston area brings two effects to the steering system. Firstly, the volume of the hydraulic cylinder changes since the piston area times the length of the cylinder equals to the volume of the cylinder. Second, the sub-matrix $[S1]$ in Equation 5.23 changes because $[S1]$ contains the piston area, A_p. In fact, the variation of piston area changes the interaction between the mechanical and hydraulic subsystems, as the boost force for the mechanical subsystem equals the working pressure times the piston area, A_p.

For each of the seven different piston areas, the roots of $\det|J-\lambda\cdot I|=0$ are calculated and listed in Table 5.4. Similar to Table 5.3, the first 5 pairs of roots in Table 5.4 have the same values as the roots of the benchmark system. Again, it confirms the dominance of the mechanical components on these natural frequencies.

It has been mentioned that the variation of the piston area changes the interaction between the mechanical subsystem and the hydraulic subsystem. But, it can be found that the roots of Numbers 6, 8 and 9 in Table 5.4 are same as the roots on the corresponding rows in Table 5.3. It means the effect of piston area on these frequencies is as same as the cylinder volume. In other words, these system frequencies are mainly influenced by the hydraulic parameters and dominated by the hydraulic subsystem in certain conditions, although they are different from the natural frequencies of the hydraulic subsystem.

As shown in Table 5.4, the 7th root is different from the 7th root in Table 5.3. This shows that these roots are affected by the interaction of the two subsystems and are the frequencies which demonstrate the coupling in the steering system. It also agrees with the results of the time domain simulation in last chapter and the frequency domain analysis in this chapter.

Table 5.3 Roots of the system matrix against the changes of the volume of the hydraulic cylinder

Factor of Volume of hydraulic power cylinder	*0.7*	*0.8*	*0.9*	*1.0*	*1.1*	*1.2*	*1.3*
1	-0.01 ± 15.37j	-0.01 ± 15.37j	-0.01 ± 15.37j	-0.01 ± 15.37j	-0.01 ± 15.37j	-0.01 ± 15.37j	-0.01 ± 15.37j
2	-0.18 ± 134.80j	-0.18 ± 134.80j	-0.18 ± 134.80j	-0.18 ± 134.80j	-0.18 ± 134.80j	-0.18 ± 134.80j	-0.18 ± 134.80j
3	-13.80 ± 382.11j	-13.80 ± 382.11j	-13.80 ± 382.11j	-13.80 ± 382.11j	-13.80 ± 382.11j	-13.80 ± 382.11j	-13.80 ± 382.11j
4	-0.01 ± 457.71j	-0.01 ± 457.71j	-0.01 ± 457.71j	-0.01 ± 457.71j	-0.01 ± 457.71j	-0.01 ± 457.71j	-0.01 ± 457.71j
5	-0.01 ± 467.60j	-0.01 ± 467.60j	-0.01 ± 467.60j	-0.01 ± 467.60j	-0.01 ± 467.60j	-0.01 ± 467.60j	-0.01 ± 467.60j
6	-78.77 ± 731.68j	-77.07 ± 715.64j	-75.90 ± 701.30j	-75.13 ± 688.43j	-74.66 ± 676.82j	-74.42 ± 666.29j	-74.36 ± 656.72j
7	-5.37 ± 971.25j	-5.45 ± 970.53j	-5.54 ± 969.81j	-5.62 ± 969.09j	-5.71 ± 968.37j	-5.80 ± 967.66j	-5.88 ± 966.95j
8	-84.98 ± 1693.24j	-92.28 ± 1689.42j	-99.13 ± 1686.06j	-105.54 ± 1683.04j	-111.53 ± 1680.29j	-117.13 ± 1677.74j	-122.35 ± 1675.35j
9	-41.53 ± 3178.11j	-43.00 ± 3174.69j	-44.26 ± 3171.98j	-45.35 ± 3169.79j	-46.30 ± 3167.99j	-47.13 ± 3166.47j	-47.86 ± 3165.18j

Table 5.4 Roots of the system matrix against the changes of the area of the piston

Factor of area of piston	*0.7*	*0.8*	*0.9*	*1.0*	*1.1*	*1.2*	*1.3*
1	-0.01 ± 15.37j	-0.01 ± 15.37j	-0.01 ± 15.37j	-0.01 ± 15.37j	-0.01 ± 15.37j	-0.01 ± 15.37j	-0.01 ± 15.37j
2	-0.18 ± 134.80j	-0.18 ± 134.80j	-0.18 ± 134.80j	-0.18 ± 134.80j	-0.18 ± 134.80j	-0.18 ± 134.80j	-0.18 ± 134.80j
3	-13.80 ± 382.11j	-13.80 ± 382.11j	-13.80 ± 382.11j	-13.80 ± 382.11j	-13.80 ± 382.11j	-13.80 ± 382.11j	-13.80 ± 382.11j
4	-0.01 ± 457.71j	-0.01 ± 457.71j	-0.01 ± 457.71j	-0.01 ± 457.71j	-0.01 ± 457.71j	-0.01 ± 457.71j	-0.01 ± 457.71j
5	-0.01 ± 467.60j	-0.01 ± 467.60j	-0.01 ± 467.60j	-0.01 ± 467.60j	-0.01 ± 467.60j	-0.01 ± 467.60j	-0.01 ± 467.60j
6	-78.77 ± 731.68j	-77.07 ± 715.64j	-75.90 ± 701.30j	-75.13 ± 688.43j	-74.66 ± 676.82j	-74.42 ± 666.29j	-74.36 ± 656.72j
7	-8.62 ± 966.57j	-7.27 ± 967.59j	-6.32 ± 968.41j	-5.62 ± 969.09j	-5.09 ± 969.65j	-4.68 ± 970.13j	-4.35 ± 970.55j
8	-84.98 ± 1693.24j	-92.28 ± 1689.42j	-99.13 ± 1686.06j	-105.54 ± 1683.04j	-111.53 ± 1680.29j	-117.13 ± 1677.74j	-122.35 ± 1675.35j
9	-41.53 ± 3178.11j	-43.00 ± 3174.69j	-44.26 ± 3171.98j	-45.35 ± 3169.79j	-46.30 ± 3167.99j	-47.13 ± 3166.47j	-47.86 ± 3165.18j

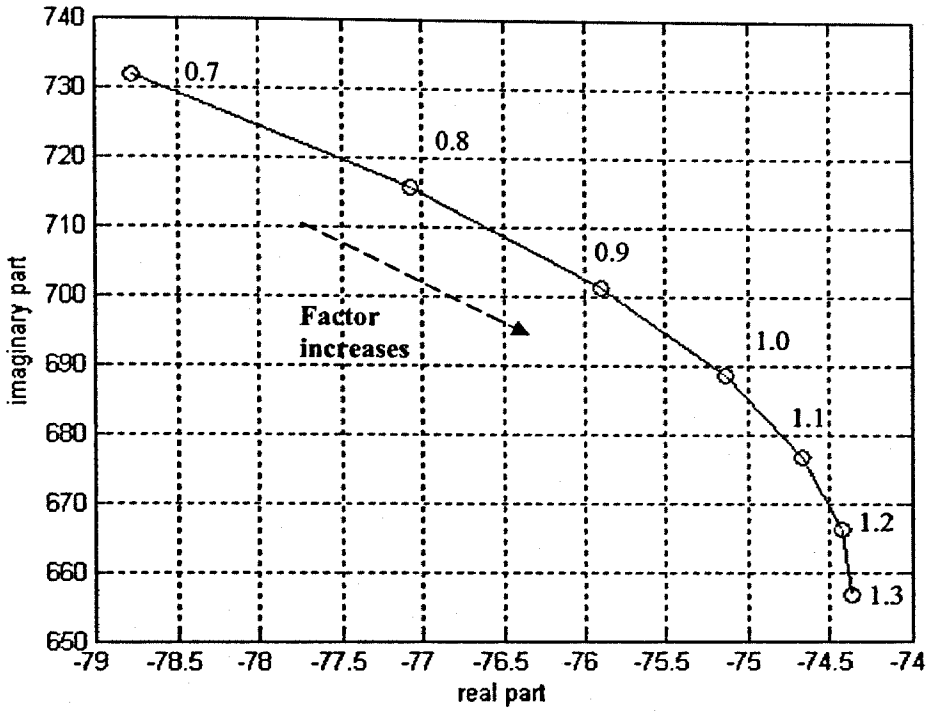

Figure 5.10 Locus of the 6th root of Table 5.3

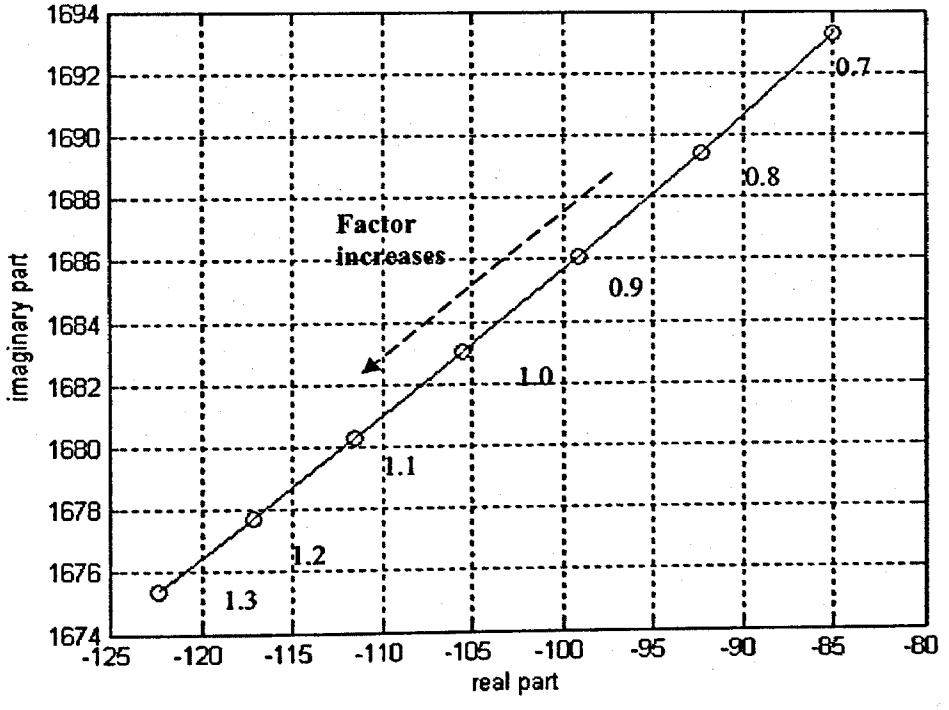

Figure 5.11 Locus of the 8th root of Table 5.3

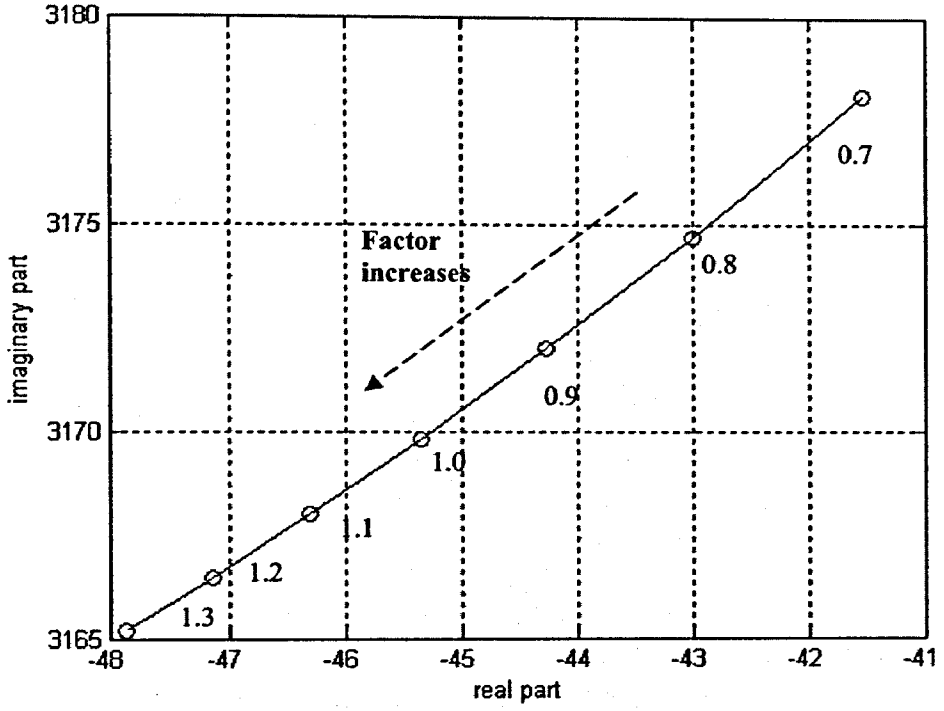

Figure 5.12 Locus of the 9th root of Table 5.3

The two loci of the 7th root in Table 5.3 and Table 5.4 are plotted in Figure 5.13. In the figure, the circles and the solid line show the locus of the root against the change of cylinder volume. The triangle marks and the dash line illustrate the locus of the root against the change of piston area.

Similar to Figures 5.10 to 12, the imaginary part of the solid line decreases when the volume factor increases. It shows the reduction of the system frequencies due to the larger cylinder volume. Meanwhile, the increase of the absolute values of the real part of the solid part indicates that the larger cylinder volume results in a larger decay factor at this natural frequency.

In Figure 5.13, the dashed line shows totally different characteristics to the solid line. The rise of the piston factor leads to the increase of the imaginary part of the dashed line, and it also causes the decrease of the absolute value of the real part of the dash line. As mentioned in the previous discussion, the increase of the piston area includes the effect of the increase of the cylinder volume. Therefore, the opposite appearances of the dash line and the solid line show that the second effect of the piston area changing overwhelms the first effect. In other words, the variation of the interaction between the mechanical and hydraulic subsystems, A_P, has more influence on this frequency.

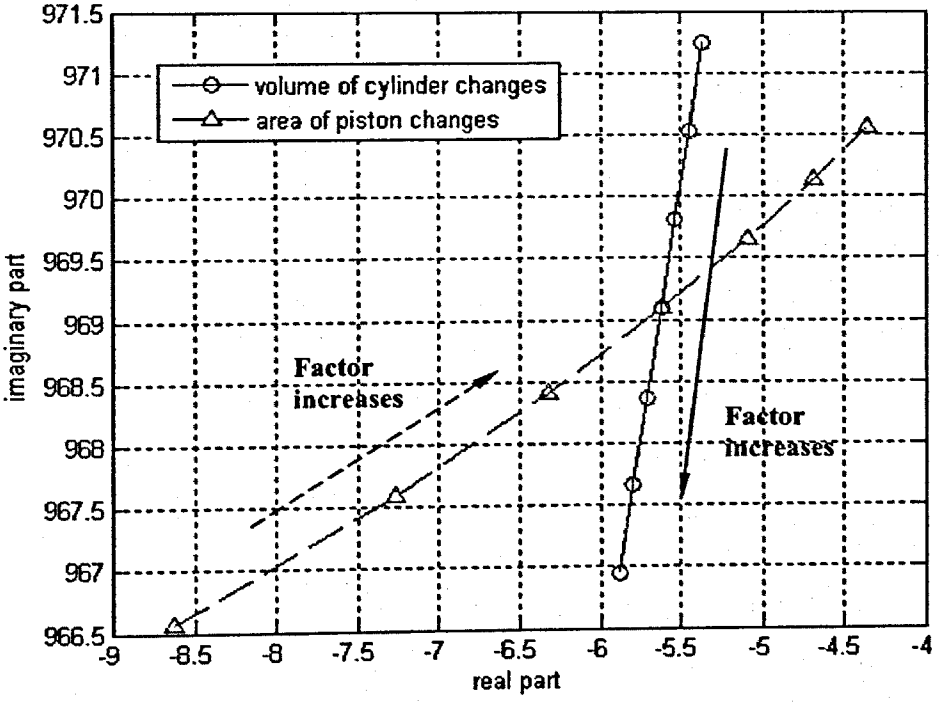

Figure 5.13 Loci of the 7th roots of Table 5.3 and 5.4

According to the dashed line in Figure 5.13, the frequencies of the system increase when the piston area increases. It is believed that larger piston area produces greater boosting force to the mechanical subsystem. The influence of the hydraulic subsystem on the whole system increases, therefore the system frequency is driven higher. It also can be seen from Figure 5.13, the energy dissipation level at this frequency decreases when A_p increases. The explanation is that the higher boosting force results in more external effects on the mechanical subsystem, thus the system inclines to the direction of instability although the change is not so significant.

In summary, the sensitivity analysis of the cylinder volume and piston area clearly demonstrates the coupling between the mechanical and hydraulic subsystems, especially at the 7th frequency in Tables 5.3 and 5.4. The variation of cylinder volume changes the parameter of the hydraulic subsystem, and its effect is limited at the hydraulic dominant system natural frequencies.

The variation of the piston area affects not only the hydraulic subsystem but also the coupling with the steering system. The 6th, 8th and 9th frequencies in Table 5.4, which are dominated by the hydraulic subsystem, repeat the values in Table 5.3. This shows the effect of the piston area changing the hydraulic subsystem. The difference between the 7th frequency in Table 5.4 and in Table 5.3 indicates the effect of the piston area changing the coupling in the system. Actually, the comparison also reconfirms the existence of the coupling between the two subsystems.

5.6 Discussion

The analysis in Section 4.2 finds two natural frequencies of the mechanical subsystem, 137.31 Hz and 175.57 Hz. The steering column and the pinion are the dominant components at these frequencies respectively. However, the numerical simulation of the steering system demonstrates a clear resonance at a frequency about 154.38 Hz, instead of these two frequencies. The natural frequencies of the hydraulic subsystem are obtained in Section 5.3, and the 154.38 Hz is not the natural frequency of the hydraulic subsystem either.

It is believed the reason for this frequency offset is because the hydraulic steering system integrates the mechanical and hydraulic subsystems and the hydraulic subsystem affects the natural frequencies of the whole system. This assumption is agreed by the analysis of the coupled system matrix. The frequency-dependent system matrix includes the characteristics of both the mechanical and the hydraulic components. The analysis of the matrix clearly illustrates the natural frequency of the whole system at about 154 Hz, instead of the frequencies of the mechanical subsystem or the hydraulic subsystem. The result of the system matrix analysis has a good agreement with the result of the time domain simulation. Furthermore, the system sensitivity to the variations of the hydraulic cylinder volume and the piston area is investigated. The effects of the two parameters on the system frequencies are understood, and the results also reaffirm the existence of the coupling relationship in the steering system.

CHAPTER 6 APPLICATIONS OF THE STEERING SYSTEM MODEL

6.1 Introduction

In Chapter 3, a comprehensive mathematical model of the hydraulic power steering system is developed and it is a general model for a typical hydraulic power steering system. Further applications of the model are shown in this chapter and the analysis is conducted to study the dynamic characteristics of two specially designed hydraulic power steering systems, the variable ratio steering system and the speed sensitive steering system. The general steering system model is extended in these applications and the special characteristics of the two steering systems are investigated.

6.2 Variable ratio steering system

6.2.1 Introduction

The steering system equipped with a rack and pinion gear is widely used in automotives due to its natural advantages, namely higher mechanical efficiency and fewer linkage parts. The variable ratio (VR) rack and pinion steering mechanism was invented to enhance the vehicle on-centre handling performance and reduce the lock-to-lock circles of the steering wheel. The variable ratio of a rack and pinion gear is usually achieved by the continuously variable shapes of the teeth of the rack from the centre to the two ends and Figure 6.1 [Website 3] illustrates a typical variable ratio steering gear. Figure 6.2 shows the ratio characteristics of the steering gear. The rack gain (deg/mm) in the centre of the rack is much higher than the rack gain at the two ends of the rack. This means that the pinion needs to have more angular displacement at the centre of rack than that it needs to have at the two ends of the rack to push the rack with the same distance. In other words, the steering ratio (steering wheel rotation/front wheel rotation) in the centre of the rack is significantly lower than the ratio at the two ends of the rack.

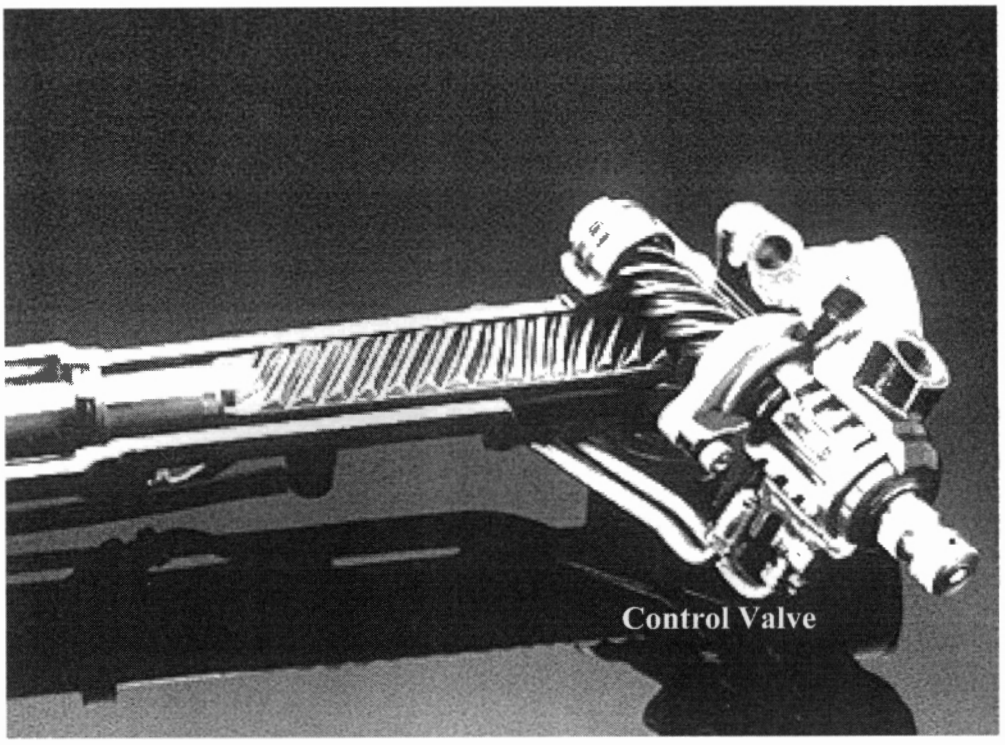

Figure 6.1 Variable ratio rack and pinion steering gear [Website 3]

Steering system mathematical models are efficient tools and are widely used to analyse and improve the performance of steering systems. As mentioned in Chapter 2, a number of steering system models have been developed by different researchers. It is found that none of the previous models includes the variable ratio rack and pinion gear set. Though the effects of the VR steering system on vehicle dynamics have been convincingly discussed by Heathershaw (2002 and 2004), the steady state and transient dynamic characteristics of the hydraulic power variable ratio steering system itself has not been reported.

Focusing on the interaction of different components and the transient dynamic responses of the complete system, a mathematical model of a variable ratio hydraulic power steering system is proposed in this section.

This model is based on the general model introduced in Chapter 3. In the model, mechanical parts of the system are developed as lumped masses interconnected with

springs and dampers. By integrating the cylinder, pump and hoses, a hydraulic circuit model is obtained where these hydraulic elements are constructed as hydraulic impedance elements, and the rotary spool valve is modelled as a four-way open centre spool valve.

With the proposed mathematical model, free and forced vibration analyses are conducted to investigate the dynamic behaviour of the hydraulic power VR rack and pinion steering system. The dynamic characteristics of the VR system are compared to that of a constant ratio (CR) steering system with the same hydraulic circuits except the rack-pinion gear set. It is found that the natural frequencies and the dynamic responses of the VR steering system are different from those of the steering system with a constant ratio.

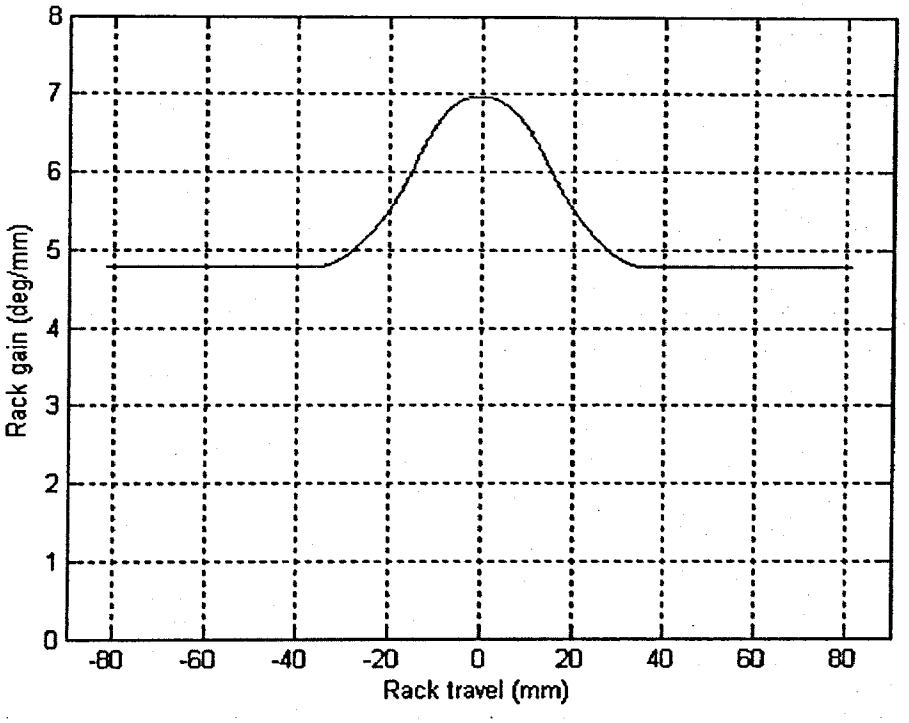

Figure 6.2 Ratio characteristics of variable ratio rack and pinion steering gear

6.2.2 Mathematical model of the variable ratio steering system

The dynamic components of a variable ratio steering system are the same as the components in a constant ratio system except the variable ratio rack. Therefore, the 12 degree of freedom (DOF) model of the mechanical subsystem of a VR steering system is similar with the model developed in Section 3.2. The structure of the VR system can also be drawn as the lumped mass model shown in Figure 3.1 except the steering rack.

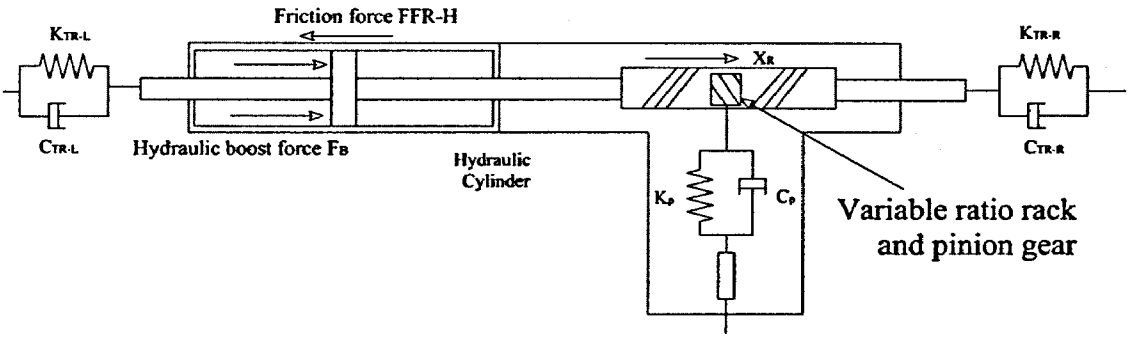

Figure 6.3 Schematic of variable ratio rack and the relevant components

As shown in Figure 6.3, the ratio between the pinion and rack in the mathematical model is variable. Thus, by using free body diagrams and the Newton's second law, the second order differential equation of motion of the rack is obtained.

$$m_R\ddot{x}_R = \frac{(\dot{\theta}_P - \dot{x}_R/N)C_P + (\theta_P - x_R/N)K_P}{N} + F_B - F_{FR-H}$$
$$-(\dot{x}_R - \dot{x}_{TR-L})C_{TR-L} - (x_R - x_{TR-L})K_{TR-L} - (\dot{x}_R - \dot{x}_{TR-R})C_{TR-R} - (x_R - x_{TR-R})K_{TR-R} \quad (6.1)$$

And the equations of motion of the VR mechanical subsystem are similar to Equation 3.13.

$$[I(M)]_{12\times12}[\ddot{\theta}(\ddot{x})]_{12\times1}+[C]_{12\times12}[\dot{\theta}(\dot{x})]_{12\times1}+[K]_{12\times12}[\theta(x)]_{12\times1}=[T(F)]_{12\times1} \tag{6.2}$$

where, θ and x are the rotational and translational displacements, I and M denote the moments of inertia and masses of the elements, C and K represent the damping and stiffness coefficient matrices, and T and F are the external torque and forces, respectively. But it should be noticed that N in Equation 6.1 is governed by the nonlinear rack gain relationship shown in Figure 6.2 whereas the N in Chapter 3 is a constant.

The characteristics of the variable ratio rack and pinion gear set are included in the parametric system by changing the variable N in the system matrices. Depending on the position of the rack and the rack gain curve shown in Figure 6.2, the value of the steering ratio changes at every time step of the numerical simulation, and the mass matrix, stiffness matrix and damping matrix of the system are re-determined at every time step to obtain the system response.

6.2.3 Free vibration analysis of the mechanical subsystem

The mechanical subsystem is linearised and its free vibration analysis is performed to investigate the natural frequencies and mode shapes of the VR mechanical subsystem.

The 12 DOF subsystem has 12 natural frequencies. Theses natural frequencies have been listed in Table 4.2, and in Figures 4.1 to 4.11. The mode shapes show the corresponding dominant components at these natural frequencies for constant gear ratio system. In this section, some natural frequencies of the VR mechanical subsystem, at which the pinion, steering column, and the tyre are the dominant components, are discussed as examples to illustrate the effects of the gear ratio on the system.

It can be seen from Figure 4.9 the pinion is the dominant component at the natural frequency 175.57 Hz. The relationship between the displacement of the rack and the

natural frequency is shown in Figure 6.4. When the pinion is at the centre position of the rack, the rack gain is at the maximum value (refer to Figure 6.2). When the pinion approaches the two ends of the rack, the rack gain decreases and then remains constant. In Figure 6.4, it can be seen that the natural frequency of the mode shown in Figure 4.1 (175.57Hz) is also the highest when the pinion is at the centre position of the rack, and the natural frequency decreases until it reaches a constant value (159.55 Hz) when the pinion approaches the end of the rack. From the centre of the rack to the end, the natural frequency reduces about 9.1%.

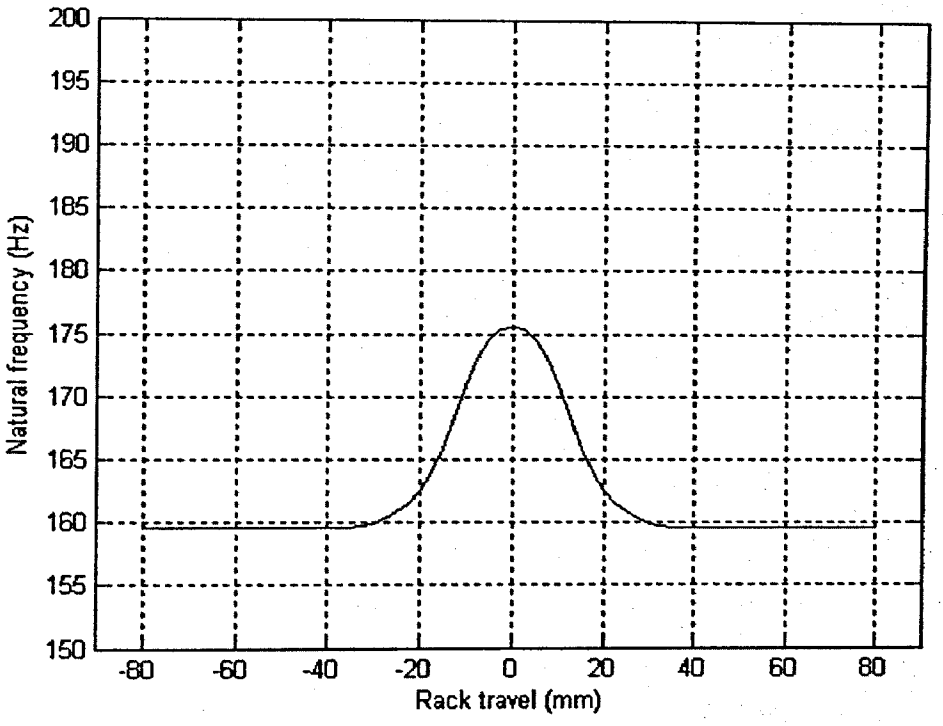

Figure 6.4 Change of natural frequency about 175.57 Hz in VR system

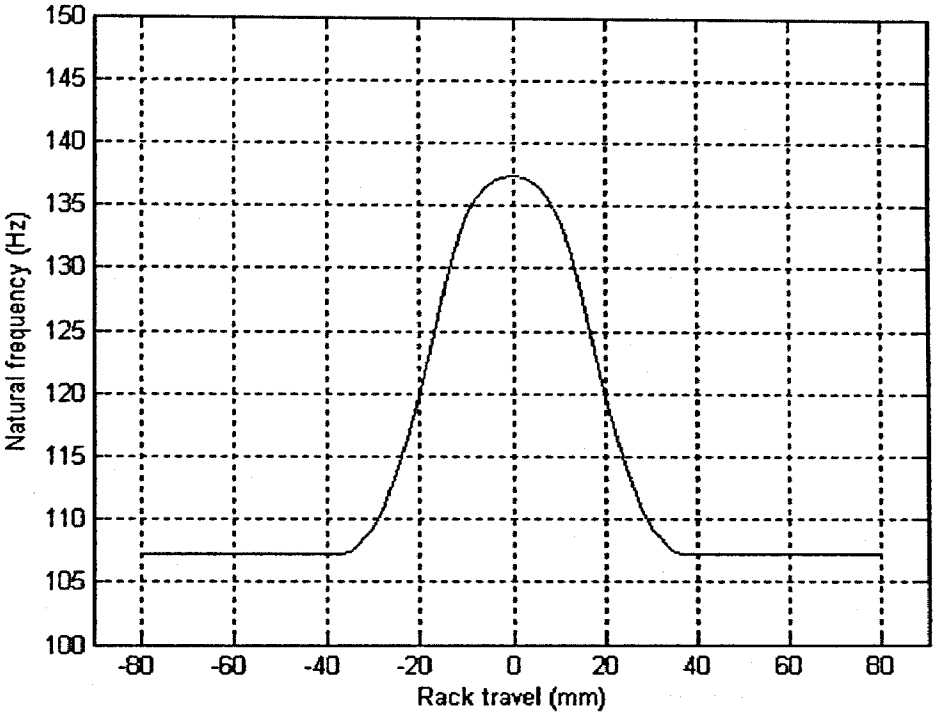

Figure 6.5 Change of natural frequency about 137.31 Hz in VR system

A similar procedure is used to analyse the natural frequency 137.31 Hz. In Figure 4.8, the steering column is the dominant component. Figure 6.5 shows the change of this natural frequency when the rack moves along the pinion. It can be seen that the natural frequency of the mode shown in Figure 4.2 (137.31 Hz) has a maximum value when the pinion is at the centre position of the rack, and the natural frequency declines to 107.26 Hz when the pinion is at the end of the rack. From the centre of the rack to the end, the natural frequency at this mode reduces about 21.9%.

The natural frequencies at other modes were also studied. It is found that not all the modes are affected by the variable ratio. When a natural frequency is dominated by the

components far from the rack and pinion gear, for example the tyre, this natural frequency is not affected by the variable ratio.

6.3.4 Transient vibration analysis of the steering system

The methods and procedures used to model the hydraulic circuit of the variable ratio system are same as those used in the Chapter 3. The VR mechanical subsystem and the hydraulic subsystem are integrated into a nonlinear hydraulic power steering system model. In the calculation, while the Runge-Kutta method is still used in the numerical simulation to analyse the forced response of the steering system in the time domain, a new computing scheme is used to overcome the calculation difficulty.

In Chapter 4, the stiffness and damping matrices of the system are unchanged during the whole process of the numerical calculation. But this method can not be used for the variable ratio steering system, as there is a variable in the system matrices. To solve the problem, the discrete data of the rack gain is collected. The data is fitted by a spline curve, and a continuous gear ratio function is generated. In the Runge-Kutta calculation, the new position of the rack is monitored at every time step. The gear ratio at that point is obtained by substituting the new rack position into the gear ratio function. Then the system matrices are updated by the new gear ratio, and the new response of the system is computed. The process is shown in Figure 6.6.

Figure 6.7 shows the simulated response of the VR steering system. The arrangement of the figure is same as Figures 4.6, 4.7 and 4.8. The initial conditions and the input of the VR system are same as those in Figure 4.6. At time zero, the steering system is at a neutral position and the displacements and velocities of all the steering components are zero. From time zero, a slow angular velocity input, which is 0.2 rad/s (11.46 deg/s), is applied on the steering wheel. Compared to Figure 4.6, it is found that the response of the VR system is almost same as the response of the CR steering system. The reason is that under a slow steering input in the first 2 seconds, the VR gear works in the area close to the neutral position of the rack, and the ratio of the VR gear close to the neutral position is similar to the ratio of a CR gear. Therefore, in this situation, the two systems have similar responses.

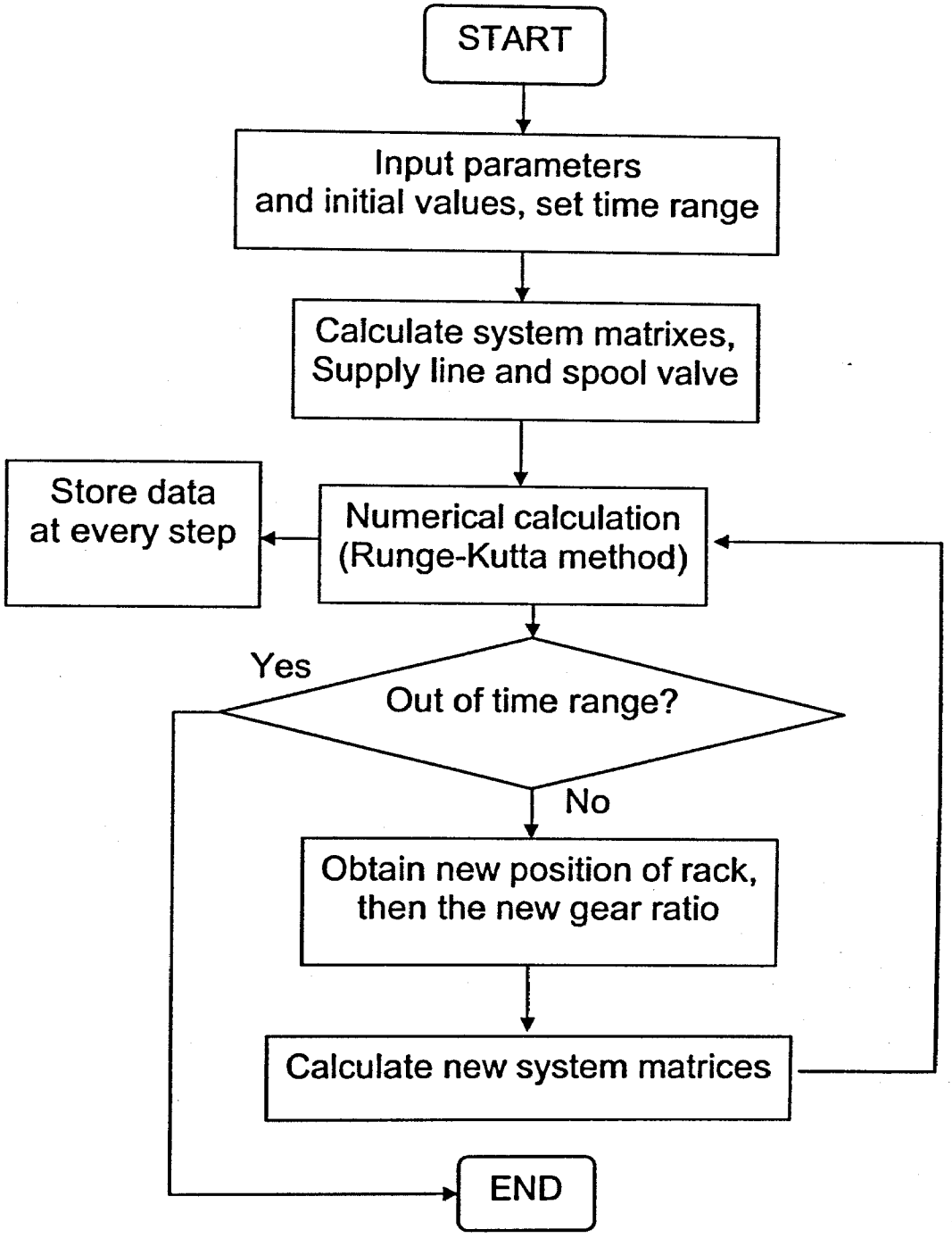

Figure 6.6 Computing scheme for the time domain simulation of the VR system

Figure 6.8 shows the responses of VR system under another steering input. Same as the input in Figure 4.7, the input in Figure 6.8 is a 3 rad/s (171.7 deg/s) constant angular velocity input. In Figure 6.8, the steering wheel and the pinion rotates about 340 degrees after 2 seconds, which is same as the CR system in Figure 4.8. It is found that the angular displacement of front wheels of the VR steering system is almost the same as the displacement of the CR steering system after 0.5 second, but it is greater than the latter after 2 seconds. The front wheel of VR system rotates about 23.12 degrees while the contact patch of the tyre turns about 16.35 degrees. These rotations are significantly larger than the wheel and tyre rotations in the constant ratio steering system shown in Figure 4.8, which are 14.9 degrees and 9.1 degrees respectively. The reason is that, while the gear ratios of the two systems are not much different when the pinion rotates in the central area of the rack, the ratio of VR system decreases sharply when the pinion meshes the outer part of the rack while the ratio of CR system remains the same. This indicates that with the same steering input the VR system has more tyre rotation than the CR system. Thus, as an important advantage of the VR system, the VR gear could has less lock-to-lock turns with similar on-center performance with the CR gear.

Since the ratio of the VR gear when the pinion is off-centre of the rack is less than the ratio of the CR gear, a larger steering torque is needed to keep a constant angular velocity steering input. Thus, as shown in Figure 6.8, the twist angle of the torsional bar of the VR system is slightly larger than the twist angle of the CR system shown in Figure 4.7. As a result, the boost force of the VR system is considerably larger than the boost force of the CR system, and it helps the driver to quickly turn the front wheels and tyres.

6.3.5 Summary

A variable ratio rack and pinion hydraulic power steering system model has been developed and its free and forced vibration has been analysed. The mechanical subsystem and hydraulic subsystem are integrated into the completed system model. Numerical simulations have been conducted to investigate the dynamics of the nonlinear parametric steering system. The hydraulic power steering system equipped variable ratio rack and pinion gear behaves differently from its constant ratio

counterpart. It is found that the variable ratio of the rack and pinion gear significantly affects not only the system natural frequencies but also the time domain responses. The developed analytical VR hydraulic power steering model produces valid predictions of the system's behaviour and therefore could assist engineers in the design and analysis of the complete system.

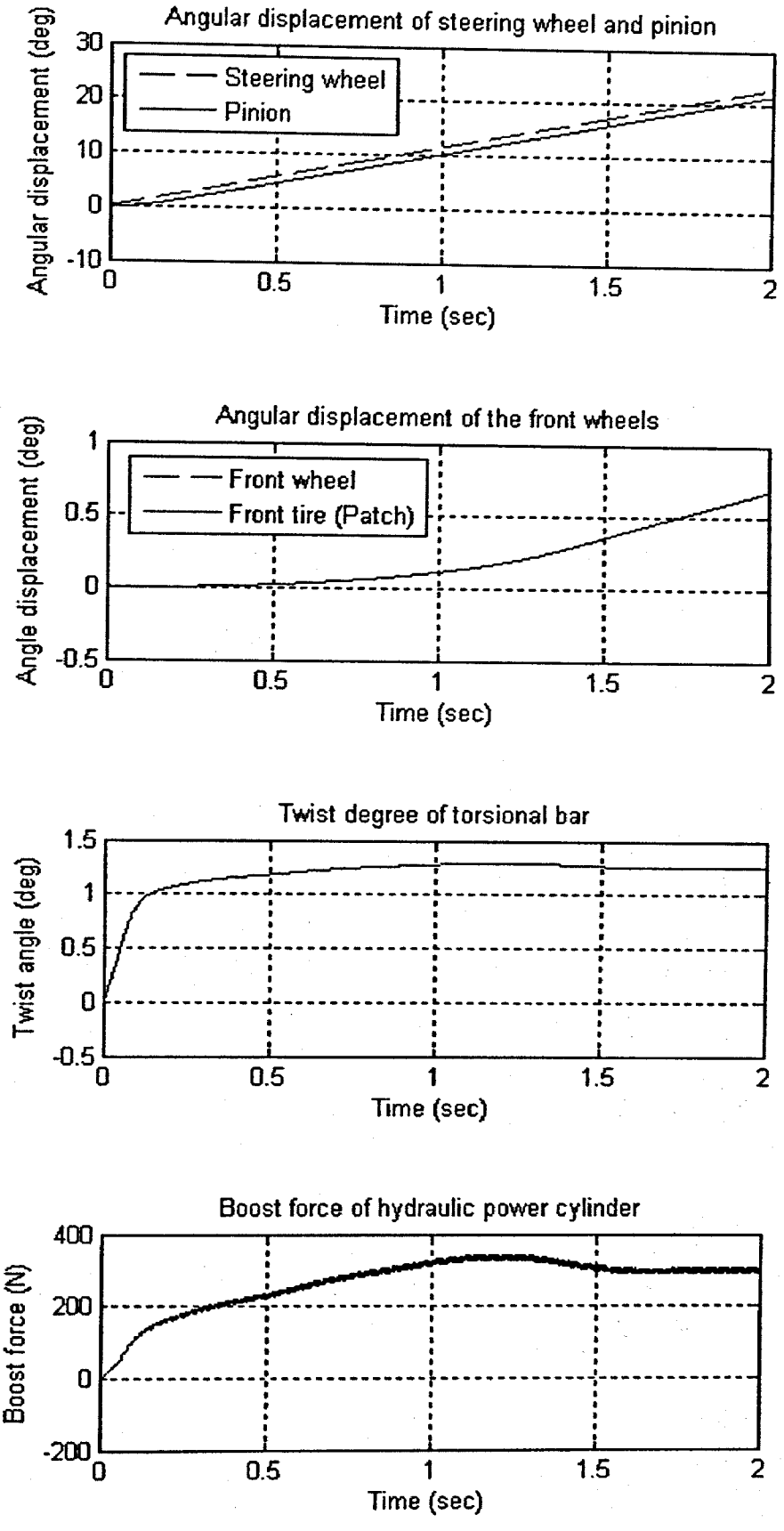

Figure 6.7 Response of variable ratio steering system to 0.2 rad/s steering input

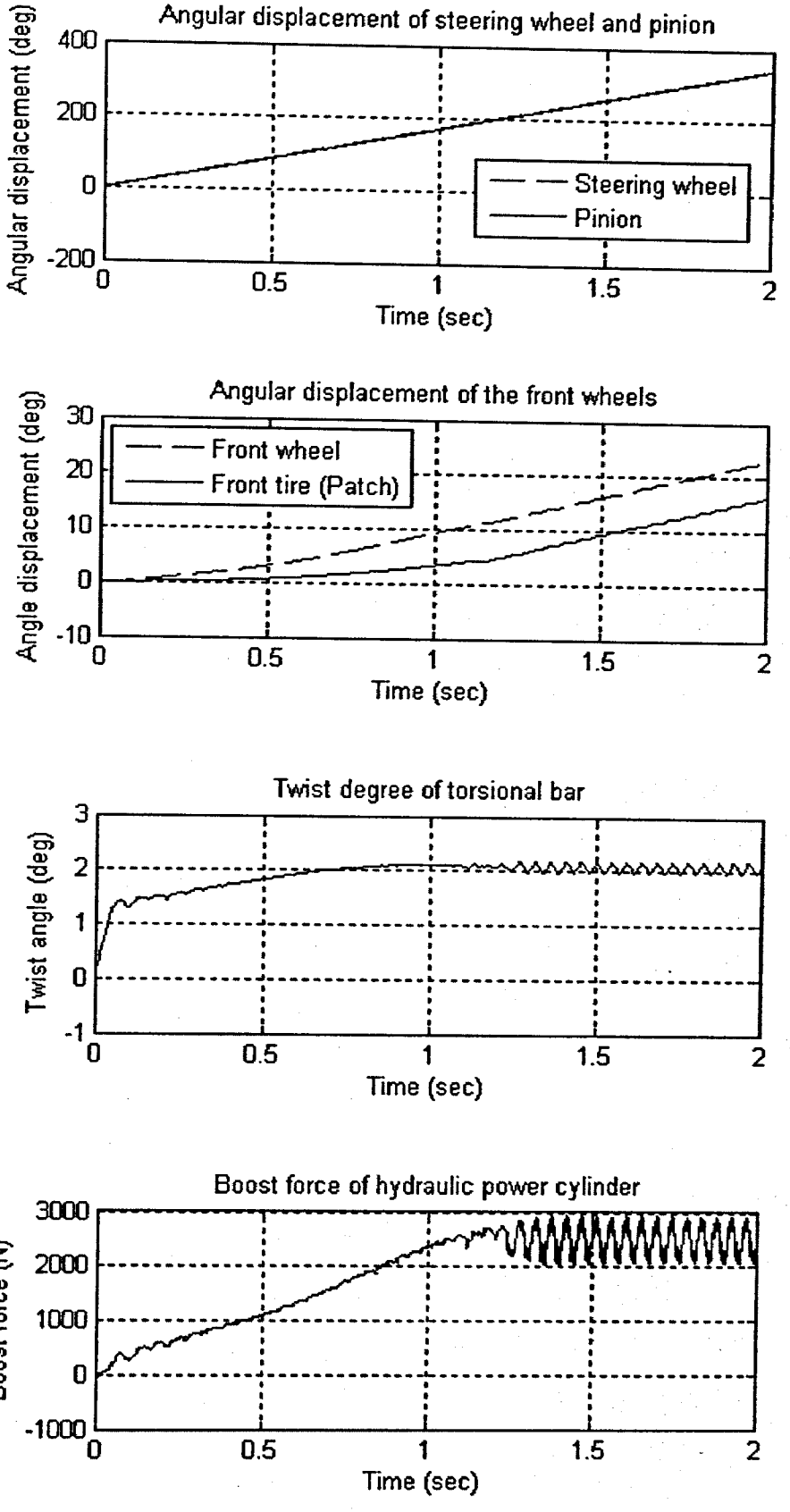

Figure 6.8 Response of variable ratio steering system to 3 rad/s steering input

6.3 Speed sensitive hydraulic power steering system

6.3.1 Introduction

The boost characteristic of a hydraulic steering system determines the relationship between the input torque and the operating pressure. A conventional hydraulic power steering system can only provide a fixed boost characteristic. In order to improve the steering performance both at high and low vehicle speeds, speed sensitive power steering systems were introduced into automobiles. These steering systems generate a variable boost characteristics as a function of the vehicle speed.

In this section, the VARIATRONIC^{TM} speed sensitive power steering system invented by A. E. Bishop and Associates [Baxter and Dyer (1988)] is modelled. While this system was designed and developed from the concept of a conventional hydraulic power steering system, it can modulate the boost characteristics by moving the outer sleeve of the spool valve along the inner shaft of the valve as a function of vehicle speed. In a conventional rotary spool valve, the only movement of the sleeve relative to the spool is the angular displacement. In a VARIATRONIC^{TM} system, however, the sleeve not only has the angular displacement but also moves axially. In this system, a solenoid valve controls the hydraulic pressure on the return side of the valve and determines the axial position of the sleeve along the spool according to vehicle speed. With the specially designed slot shapes on the spool, the valve provides variable opening area characteristics against vehicle speed.

In this section, the performance and dynamic characteristics of the speed sensitive hydraulic power steering system are investigated. The result highlights the variable boost characteristics of the speed sensitive steering system, which is the key feature of the system.

6.3.2 Mathematical model of speed sensitive power steering system

As per the general steering system model developed in Chapter 3, the mathematical model of a speed sensitive power steering system consists of the mechanical subsystem model and the hydraulic subsystem model. The mechanical components of the speed sensitive steering system are also modelled as the lumped masses or moments of

inertia and are connected by springs and dampers. The details of the 12-DOF mechanical model have been shown in Chapter 3.

Since the hydraulic circuit of the speed sensitive steering system is also the same as a conventional steering system except for the rotary spool valve, the valve is the focus in the study of a speed sensitive model.

The rotary spool valve used in this hydraulic power steering system can be modelled as a four-way open centre valve, in which the fluid passes through four ports simultaneously. During a steering manoeuvre, two ports open more, and the other two ports open less. Since the steering pump can be regarded as a constant flow rate pump, the changes of the opening areas increase the pressure of the fluid in the supply line. Consequently, the pressure difference between the two sides of the hydraulic cylinder increases. In Chapter 3, the two governing equations of the rotary spool valve were given. They are rewritten as follows:

$$Q_S = C_d A_1 \sqrt{\frac{1}{\rho}(P_S - P_L)} + C_d A_2 \sqrt{\frac{1}{\rho}(P_S + P_L)} \tag{6.3}$$

$$Q_L = C_d A_1 \sqrt{\frac{1}{\rho}(P_S - P_L)} - C_d A_2 \sqrt{\frac{1}{\rho}(P_S + P_L)} \tag{6.4}$$

where Q_S is the supply flow rate, A_1 and A_2 are the opening and closing areas of the valve ports respectively, P_S and P_L are the pressure of supply flow and the pressure drop across the load respectively, and Q_L is the load flow rate. ρ is the density of the fluid.

The performance of a hydraulic power steering system, including the boost characteristics of the spool valve, is largely dependent upon the relationship between the twist angle of the torsional bar and the opening areas of the valve ports. The schematic of open area of a conventional steering control valve is shown in Figure 3.11, and the nonlinear relationship between the valve angle (twist angle of the

torsional bar) and the orifice area of the valve is shown in Figure 6.9. It is noted that when the valve angle is relatively small the opening area decreases at a greater rate, and when the valve angle is relatively large the slope of the area has a smaller rate. This characteristic helps to quickly increase the assistant force in small valve angle conditions and avoid steering system instability in large valve angle conditions.

To reduce the steering effort of the driver, the hydraulic steering system is required to supply a large assistant force with a relatively small effort from the driver at parking or low vehicle speeds. At high vehicle speeds, however, the steering system should provide enough steering feel [Baxter (1988)], which is the ratio between the differential of torque on the steering wheel and the differential of output force of the steering system (dT/dF), in order to improve the vehicle's on-centre handling and avoid accidents. It is hard for a conventional steering system to fulfill both of the requirements because it only has a fixed boost characteristic which is independent of the vehicle speed.

Speed sensitive steering systems solve this dilemma by changing the boost characteristics according to the vehicle speed. There are several ways the hydraulic power steering systems provide variable boost characteristics. The VARIATRONIC™ system has a variable relationship between the valve angle and the opening area to achieve the variable boost characteristics, as featured in Figure 6.10. In contrast to the characteristics of the conventional system shown in Figure 6.9, the speed sensitive system provides appropriate relationships between valve angle and orifice area at different vehicle speeds. While the valve opening area drops with the increase of the valve angle at all speeds, with a certain valve angle the valve opening area at low speed is smaller than that at high speed. This feature allows the system to generate a higher boost force quickly at low speed and have a relatively slow increase of boost force at a high speed. In the simulation, A_1 and A_2 in Equations 6.3 and 6.4 are determined by the 3D plot in Figure 6.10 to generate the variable boost characteristics of the system.

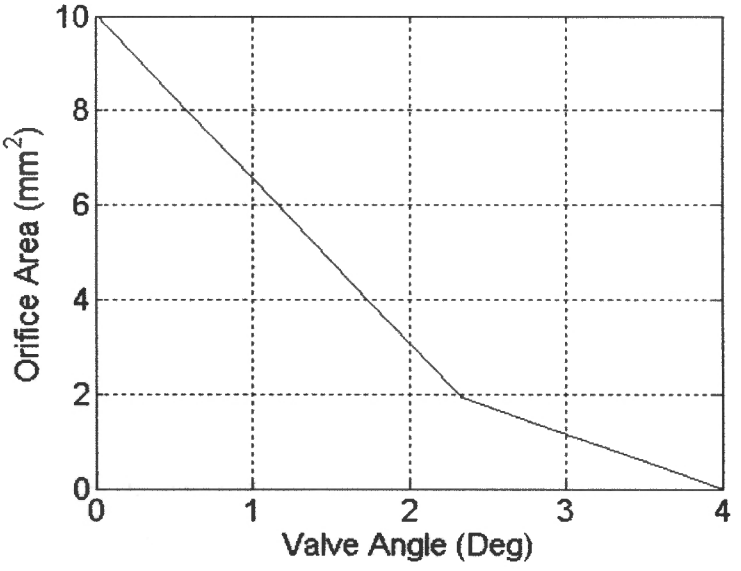

Figure 6.9 Relationship between valve angle and orifice area of a conventional steering valve

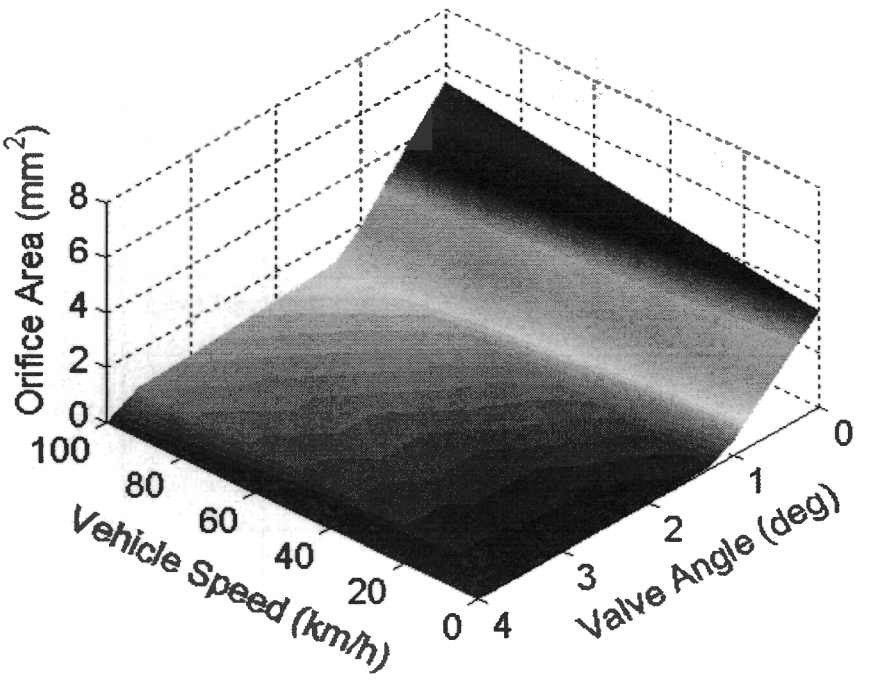

Figure 6.10 Relationship between valve angle and orifice area of a speed sensitive valve

6.3.3 Family of Boost Characteristics

As the speed sensitive steering system can provide variable boost characteristics to optimise the performance of the system under different vehicle speeds, the study here focuses on the special characteristics of the system. During the simulation, different vehicle speeds, such as parking speed (0 km/h), 15km/h, 50km/h and high speed (100 km/h), are input in the steering system model respectively as a parameter. The characteristics of the valve opening areas are determined by the relationship shown in Figure 6.10. The system response in the time domain is obtained by the calculation scheme introduced in Chapter 4. Therefore, the characteristics of the control valve (the boost characteristics of the system) can be obtained after the twist angle of the torsional bar and the working pressure are compared.

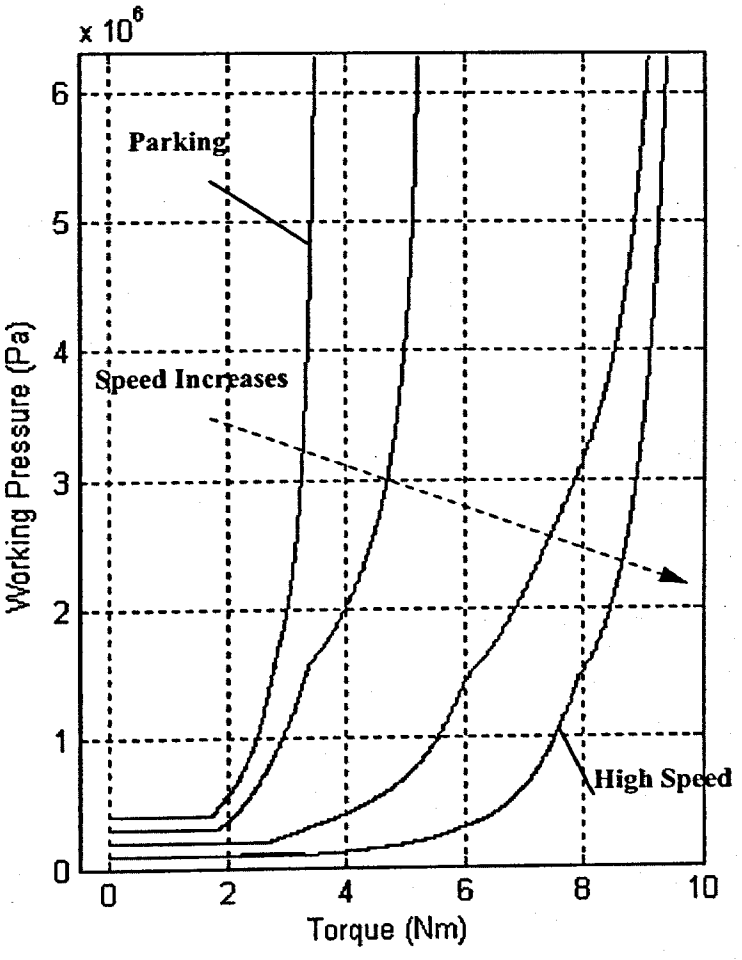

Figure 6.11 Simulation of the boost characteristics family

Figure 6.11 shows the family of simulation results of the boost characteristics of a typical hydraulic speed sensitive steering system. The horizontal axis is the input torque on the steering wheel and the vertical axis denotes the hydraulic operating pressure of the steering system. Every curve in the figure indicates the dynamic characteristics of the speed sensitive system at a particular vehicle speed.

At parking and low vehicle speeds, the system supplies high pressure when the input torque is small, therefore the system helps the driver turn the front wheels quickly and easily. At high vehicle speeds, however, the system deliberately provides a small assistant force even when the input torque is relatively high; as a result, the vehicle handling is improved and the vehicle is more stable at the high speeds. The simulated results agree very well with the experimental results reported by Baxter *et al.* (1988). Furthermore, by tuning the parameters of the simulation, a variety of boost curves can be generated to satisfy different design objectives and requirements.

It needs to be pointed out that the high frequency pressure ripple is eliminated from the simulation of the speed sensitive system to highlight the variable boost characteristics. As a result, the curves in Figure 6.10 do not record the dynamic relationship between the torque and the pressure. This makes the curves of Figure 6.10 smoother than the curve in Figure 4.9 although both of them present the boost characteristics of the steering system.

In summary, the applications of the developed model of the integrated power steering system show the dynamic characteristics of the two special steering systems. In addition, the analysis process demonstrates the capabilities and efficiencies of the model in the steering system design, analysis and simulation. The model can be a flexible tool to design steering systems and simulate the performance of the system before the prototype is made. Also, it can analyse the dynamics of existing systems and be used to optimise the system components. This can reduce the trial-and-error and assist the improvement of steering systems.

CHAPTER 7 STEERING SYSTEM TEST RIG

7.1 Introduction

In order to experimentally investigate the dynamics of hydraulic power steering systems and verify the developed mathematical models, a steering system test rig is designed and built. This low-cost test rig provides an approximately realistic operating condition for a hydraulic power steering system, and produces the transient responses in hydraulic pressure under various steering inputs.

Many other steering system test rigs have been developed by researchers in automotive industries and universities for different research purposes. However, most of these test rigs do not focus on the interaction between the hydraulic and mechanical steering components and can not simulate real world operating conditions. Steering system testing on vehicles is also conducted by car manufacturers, but these tests are costly and can only be done on particular steering systems and vehicles. In addition, the limited space under the vehicle hood can make testing difficult. Laboratory based experiments, on the other hand, are more efficient if realistic operating conditions can be simulated.

The test rig introduced in this chapter not only had all the components of a typical rack and pinion hydraulic power steering system, but also included the front suspension system and the front tyres. Therefore, the performance of the steering system could be tested in an environment that incorporated all the dynamic components interacting with the steering system. The interaction between the steering system and the front suspension could be clearly observed and the fluid pressures in the cylinder feeding lines of the system could be conveniently measured. In addition, the test rig was made flexible and many steering components or steering systems can be tested on the rig with minor modification.

7.2 Design of the test rig

The steering system test rig consisted of three main parts: the vehicle components including the steering system components and the chassis components that are kinematically linked with the steering system, the test rig frame and the control/measurement equipment. The test rig is shown in Figures 7.3 to 7.6.

7.2.1 Vehicle components

In consideration of the cost, a used vehicle front suspension is purchased. The suspension system is disassembled from a 1997 model Holden Commodore VT sedan which was manufactured by GM Holden Ltd in Australia. It is a McPherson suspension that includes the front crossmember, control arms, springs, shock absorbers and tyres. Also, the steering column, steering pump, reservoir and hydraulic hoses are from the same sedan.

Tristar Steering and Suspension Australia Ltd, the steering system supplier for the GM Holden Ltd, generously supplies a hydraulic power steering gear for this test rig. The gear includes the rotary spool valve, rack and pinion gear, hydraulic power cylinder and tie rods. Figure 7.1 shows all the components of the front suspension and the steering system.

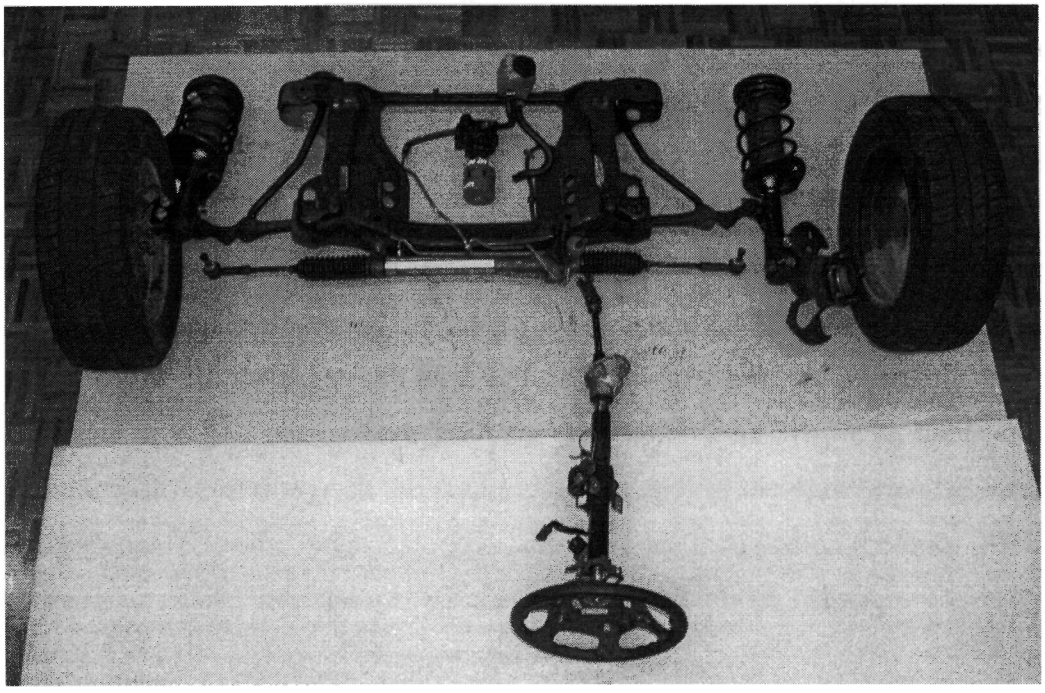

Figure 7.1 Disassembled hydraulic power steering system and front suspension

7.2.2 Test rig frame

A test rig frame is designed and installed to support the front suspension and the steering system (Refer to Appendix). The main structure of the frame consists of 75×75×3mm RHS tubes. Three pairs of crossbeams are welded on the frame; the upper crossbeams, the middle crossbeams and the lower crossbeams. The crossmember of the vehicle is fixed on four brackets of the middle crossbeams by four bolts. An upper channel and a lower channel (150x75mm) are bolted on the upper crossbeams

and lower crossbeams respectively. The two channels compress the front suspension. The two ends of the upper channel are inclined at ten degrees angle from the horizontal to accommodate the kingpin inclination in the suspension.

Two disks are mounted on the lower channel to support the tyres. By tightening the clamp screws, the disks can be fixed on the beam to provide a higher friction force to the tyres. Otherwise, the clamp screws can be loosened, the disks so that rotate with the tyres and simulate a low friction surface.

The average load on each front spring of the Holden Commodore sedan is about 432 kg, and this load compresses the spring from a free length of about 280 mm to a compressed length of about 180 mm. During the installation, the two front wheels are dissembled from the hubs at first. Then, the suspension units are put on the frame and a hydraulic jack is used to push the suspension unit against the upper channel until there is enough space for the tyres. After that, the tyres are installed on the hubs. At last the two disks are raised until the springs are compressed to about 180 mm.

The upper and lower channels can be replaced or modified, and the height of the disks can also be adjusted. Thus, if it is required, other suspension systems with different dimensions can also be mounted on the test rig frame.

The steering pump and an electric motor are fixed on a plate which is mounted on the middle crossbeams of the frame. The steering column is fixed on the test rig frame by a holder made from 50×50×2mm RHS tubes and a bracket made of 5 mm thickness steel plate. In the test rig, the pump and the steering column are mounted so that their positions relative to the other steering system components are the same as in the original vehicle.

7.2.3 Control and measurement equipment

In a vehicle, the engine drives the hydraulic pump of the steering system through the drive belt. In this test rig, an electric motor is used to drive the steering pump through a flexible coupling. Both sides of the coupling are modified to fit the shaft of the pump and the shaft of the motor. Since an engine driven steering pump operates over a range

of speeds, a SAMI GS ACS Frequency Converter made by ABB is used in the test rig to adjust the rotational velocities of the electric motor. A pressure gauge with 0-100 bar measure range is installed in the high pressure supply line by a brass female branch tee. The gauge provides a reading of the pressure in the supply line and indicates if the hydraulic system is working normally.

To measure the cylinder pressure, two AST 4000 stainless steel pressure sensors manufactured by American Sensor Technologies, Inc are respectively installed in the two cylinder feeding pipes using two branch tees. The signals of the two sensors are sent to an AR 1200 six-channel analysing recorder made by Yokogawa Electric Corporation. The signals can be read on the screen of the recorder and the data can be saved on floppy disks for further analyse in a personal computer.

In addition, an accelerometer (Brüel & Kjær type 4332) is mounted on the front wheel to check the dynamic characteristics of the mechanical subsystem. The signal of the accelerometer is amplified by a charge amplifier (Brüel & Kjær type 2651) and sent to the Yokogawa analysing recorder. During testing, the accelerometer is mounted at different positions to monitor the vibration modes of the front wheel.

The schematic of the test rig is shown in Figure 7.2, and Figures 7.3 to 7.6 are the photos of the test rig from different angles of view.

The design drawings of the steering system test rig are completed in Solid Edge V14. Some drawings of the test rig are shown in the Appendix of this thesis.

Figures 7.7 to 7.9 show the three different positions of the accelerometer which are named Positions A, B and C respectively. The details of the testing are discussed in the following chapter.

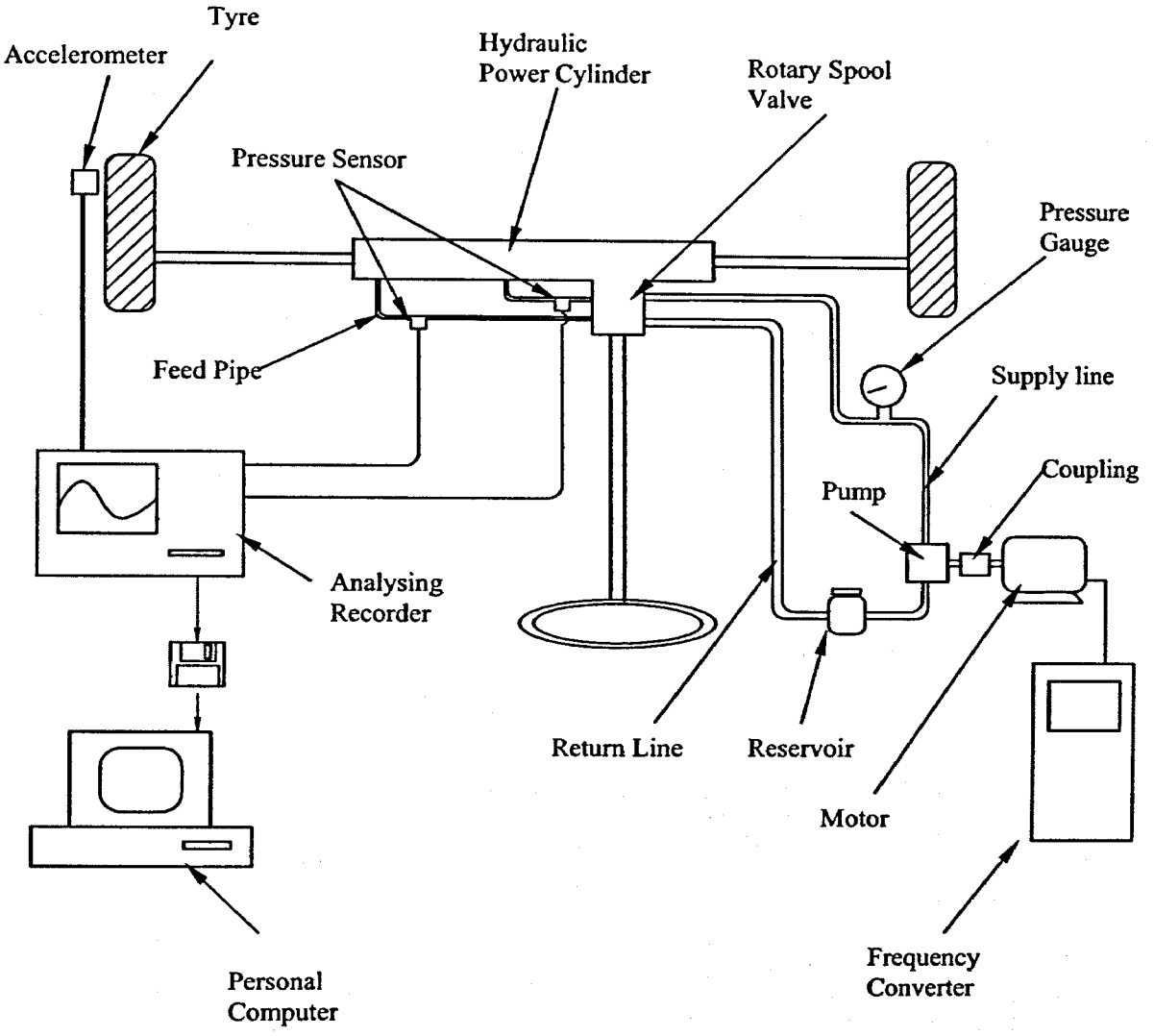

Figure 7.2 Schematic of hydraulic power steering system test rig

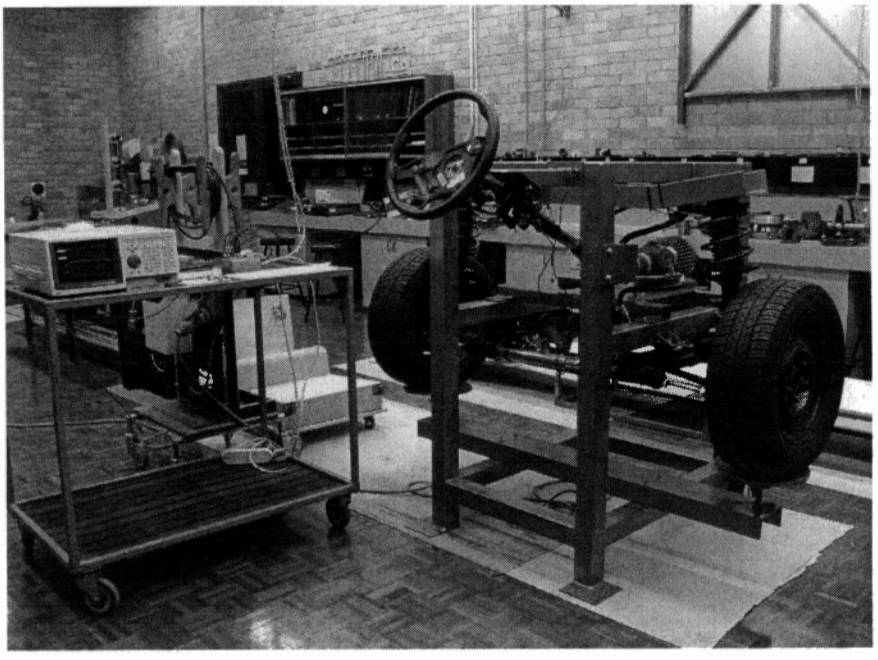

Figure 7.3 Hydraulic power steering system test rig (main view)

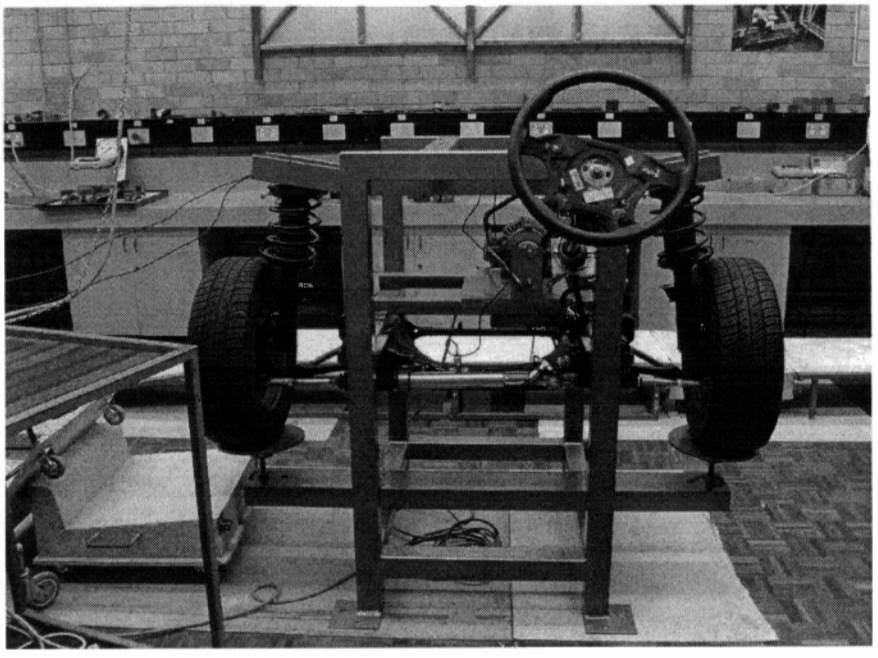

Figure 7.4 Hydraulic power steering system test rig (front view)

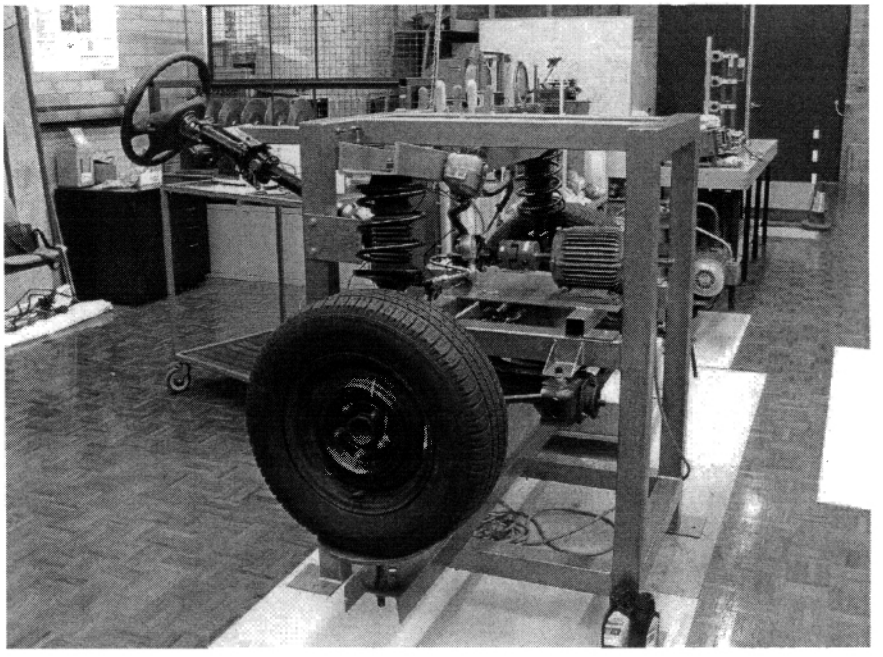

Figure 7.5 Hydraulic power steering system test rig (side view)

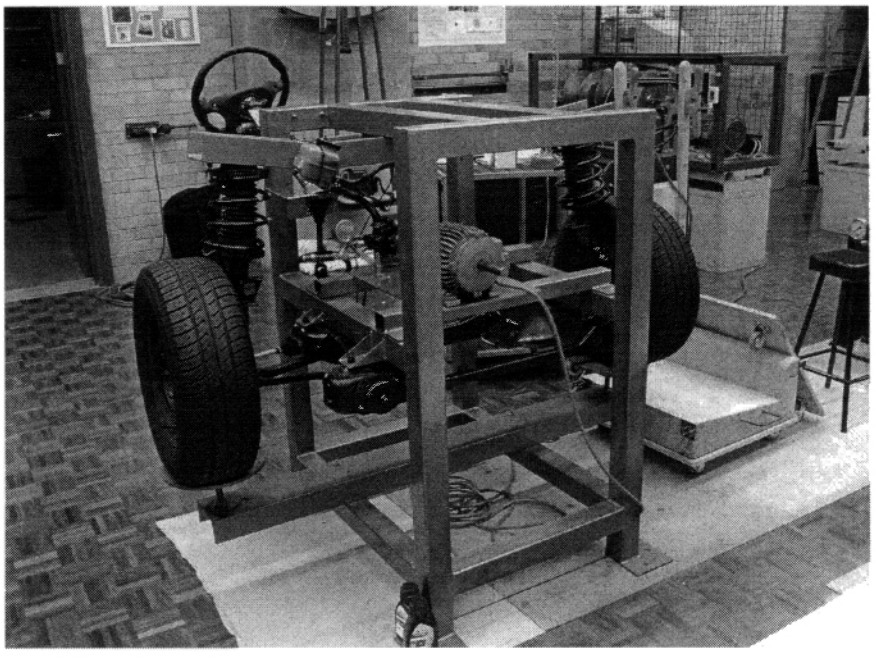

Figure 7.6 Hydraulic power steering system test rig (back view)

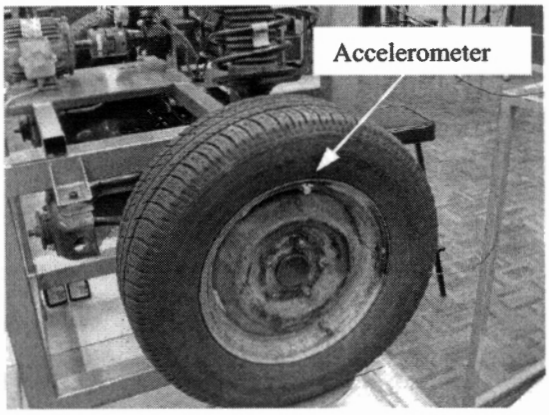

Figure 7.7 Accelerometer on the top of the wheel rim (Position A)

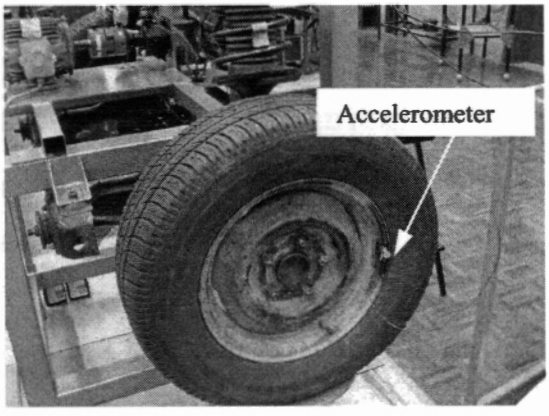

Figure 7.8 Accelerometer on one side of the wheel rim (Position B)

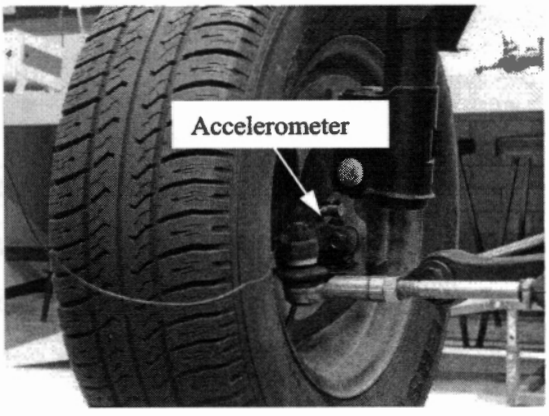

Figure 7.7 Accelerometer on the centre of the wheel (Position C)

CHAPTER 8 TESTING AND ANALYSIS

8.1 Introduction

After the hydraulic power steering test rig is commissioned, a series of experiments were carried out to validate the mathematical models and the computer simulation of the system. This enables a deeper understanding of the dynamic characteristics of the hydraulic power steering system. The experiments can be classified into three main parts, the impact testing on the mechanical subsystem, the steering shudder testing and the pressure ripple testing. The impact testing on the mechanical subsystem was performed to validate the mathematical model and the free vibration analysis of mechanical subsystem. The steering shudder testing was to validate the transient time domain analysis of the hydraulic power steering system. The coupled system natural frequency was confirmed by the pressure ripple testing.

8.2 Impact testing on the mechanical subsystem

According to free vibration analysis of the mechanical subsystem presented in Section 4.2, the front wheels and tyres have significant effects on the hydraulic power steering system, especially at 21.45 Hz shown in Figure 4.3. The impact testing was designed and conducted to investigate the dynamic characteristics of these components. An impulse input was applied to different positions of the front wheel, and the acceleration signals of the different positions of the front wheel and tyre were recorded and analysed.

Using the left front wheel as an example, Figure 8.1 shows the coordinate system of the front wheel and the tyre. The six degrees of freedom include the translation in X, Y and Z directions and the rotation in γ, ω and α directions. The restrictions on the front wheel motion (also called the steel hub) are simplified and include the forces from the control arm of the front suspension, the tie rod and the rubber tyre. The impact testing obtains the main vibration modes and find the effects of the modes on the hydraulic power steering system. It must be pointed out that because of the complicated structure of the front suspensions and the nonlinear characteristics of the tyres, the vibration modes of the front wheel are coupled and complex. However, the testing does provide

a general understanding of the dynamic characteristics of the front wheel and tyre and highlight effects of the components on the steering system.

During the testing, there was no steering pump input and no steering wheel input. A hammer was used to provide an impact to the centre of the wheel, the sidewall of the tyre at the 12 o'clock position and the sidewall of the tyre at the 3 o'clock position. The three inputs were named Case 1, 2 and 3, and they are listed in Tables 8.1, 8.2 and 8.3 respectively. In each case, the accelerometer was mounted on different positions of the wheel. Referring to Figures 7.7, 7.8 and 7.9, the position at the top of the wheel rim is named Position A, the position of the one side of the wheel's sidewall is named Position B and the position at the centre of the wheel is named Position C. Therefore, combining the different positions of the shock inputs and the accelerometer, the nine cases of the impact testing, from Case 1A to Case 3C are listed in Tables 8.1 to 8.3.

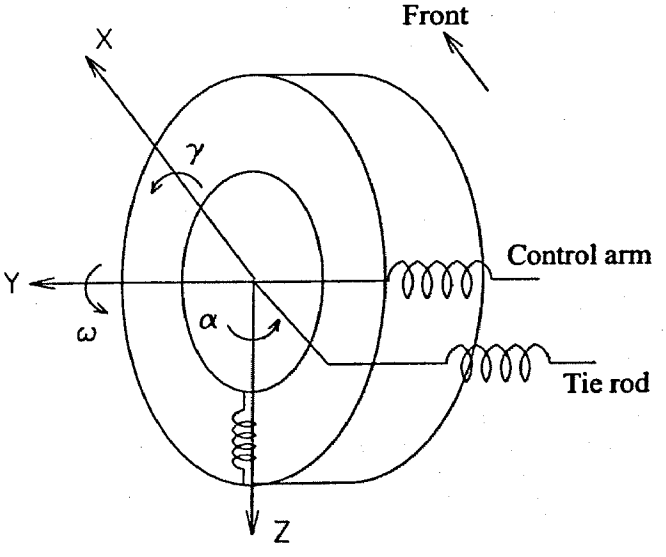

Figure 8.1 Coordinates of front wheel and tyre

The figure in the first column of Table 8.1 shows the coordinates of the front wheel and the black triangle marks the position where the impulse input is applied. In the second column, the side views of the wheel are shown and the different positions of the accelerometer are represented by a black hexagon. The testing data of Table 8.1 is shown in Figures 8.2, 8.3 and 8.4. In these figures, the top plot is the signal of the accelerometer in time domain and the bottom plot is the FFT (Fast Fourier Transform) result of the time domain response. The vertical axis of the bottom plot is the power spectrum obtained from FFT. The main frequencies found in the FFT analysis are listed in the third column of Table 8.1 for each case. Also, based on their amplitudes in the FFT analysis, in Table 8.1 the frequencies are given approximate evaluations, such as large, medium and small, to describe their effects in certain case. Therefore, in the every line of third column of Table 8.1, the first number is frequency, the second number is the amplitude of the frequency in FFT plot, and the approximate evaluation follows the two numbers. The aim of those plots is to compare the frequency components within every single impact test, for example, to compare the frequency components in Case 1A. It is not to compare the amplitudes of frequency components in different cases. The comparison of amplitudes of FFT results between two cases, for example between Case 1A and 1B or between Case 1A and 3A, is meaningless. In the analysis, only the frequencies less than 200 Hz are discussed because the main concern of the frequencies of the wheel and tyre focuses on the low frequencies. Tables 8.2 and 8.3 list the frequency responses of Case 2 and Case 3 respectively, and Figures 8.5 to 8.10 show the testing data for the two cases.

In Case 1, the impulse input is applied on the centre of the wheel. It is believed that the main vibration mode of the wheel stimulated by the input is the translational movement along the Y axis. Also, due to the restriction of the friction from the ground, a rotational movement in the γ direction is found. In Case 1A of Table 8.1, when the accelerometer is fixed on the top of the wheel's sidewall, 70.3 Hz is the main frequency whereas a 34.7 Hz frequency also can be found. In Case 1B, 70.8 Hz is also important. In Case 1C, when the accelerometer is at the centre of the wheel, only 69.8 Hz is found. The Case 1 testing indicates a frequency about 70 Hz dominates the translation vibration mode in the Y direction.

Table 8.1 Frequency responses of front wheel in Case 1

Cases (The triangle represents the position where the impulse input is applied, and the hexagon shows the position of the accelerometer)		**Frequency responses (Frequency, amplitude in FFT, evaluation)**
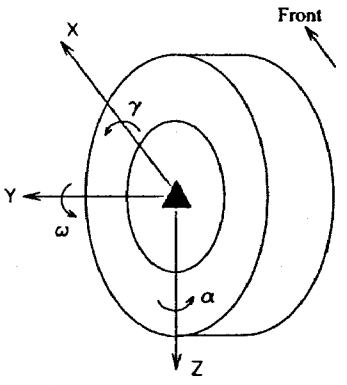 **Case 1** Impulse input is applied to the centre of the tyre	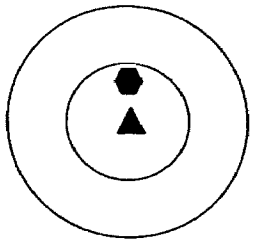 **Case 1A** Accelerometer at the 12 o'clock position on the wheel rim	34.7 Hz, 0.004203, small 70.3 Hz, 0.0257, large (Refer to Figure 8.2)
	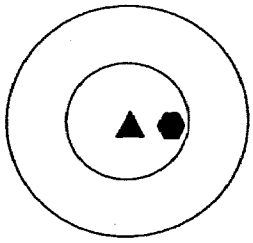 **Case 1B** Accelerometer at the 3 o'clock position on the wheel rim	39.1Hz, 0.001757, small 70.8 Hz, 0.006486, large (Refer to Figure 8.3)
	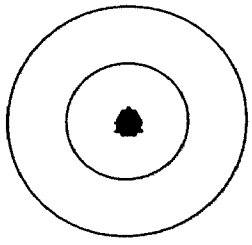 **Case 1C** Accelerometer at the centre of the wheel	69.8 Hz, 0.01107, large (Refer to Figure 8.4)

Shown in Table 8.2, the impulse input is applied on the top of the sidewall of the tyre. As a result, the main vibration modes of the wheel stimulated by this input should include the rotation in the γ direction and the translation along the Y axis. It was found in Case 2A, a 33.2 Hz frequency is significant and the 43.0 Hz and 67.4 Hz could be found. The frequencies in Case 2B include 31.3 Hz, 39.1 Hz and 68.9 Hz. The responses of Case 2C are similar to the responses of Case 2A. Supported by the analysis of Case 1A, Case 2 shows a frequency about 33 Hz could be the main vibration frequency of the rotation in the γ direction. Also, the frequencies close to 70 Hz reaffirm the analysis in Case 1.

In Case 3, the impulse input is applied to one side of the sidewall of the tyre. Thus, the rotations in the α and γ directions and the translation along the Y axis could be the main vibration modes of the wheel stimulated by this input. Case 3A generates the frequencies of 33.7 Hz, 41.5 Hz and 82.0 Hz. It is noticed that in Case 3B and 3C there are frequencies about 24 Hz which are not present in other cases. Because of the position of the input in Case 3, it is believed the 24 Hz frequency are the vibration mode of the rotation in α direction, and obviously this mode has a significant effect on the steering system. There are frequencies about 40 Hz in most of the cases in spite of the different inputs. It is regarded as the local vibration mode of the tyre.

Table 8.2 Frequency responses of front wheel in Case 2

Cases (The triangle represents the position where the impulse input is applied, and the hexagon shows the position of the accelerometer)		**Frequency responses**
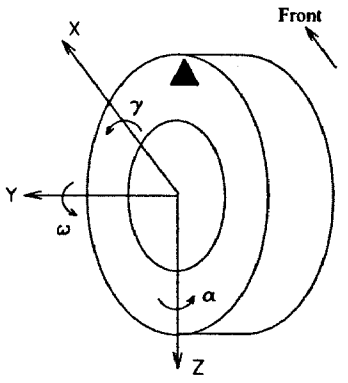 **Case 2** Impulse input is applied to the top of the sidewall of the tyre	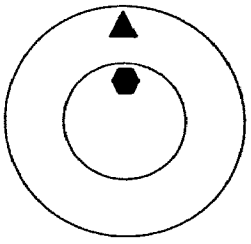 **Case 2A** Accelerometer at the 12 o'clock position on the wheel rim	33.2 Hz, 0.4034, large 43.0 Hz, 0.05721, small 67.4 Hz, 0.07459 medium (Refer to Figure 8.5)
	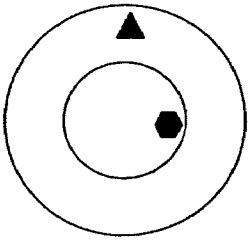 **Case 2B** Accelerometer at the 3 o'clock position on the wheel rim	31.3 Hz, 0.01054, small 39.1 Hz, 0.07868, large 68.9 Hz, 0.01851, medium (Refer to Figure 8.6)
	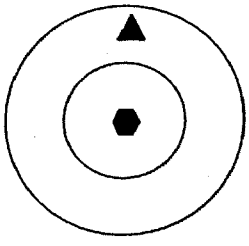 **Case 2C** Accelerometer at the centre of the wheel	33.7 Hz, 0.007633, large 43.0 Hz, 0.001077, small 68.4 Hz, 0.004122, medium (Refer to Figure 8.7)

Table 8.3 Frequency responses of front wheel in Case 3

Cases (The triangle represents the position where the impulse input is applied, and the hexagon shows the position of the accelerometer)		**Frequency responses**
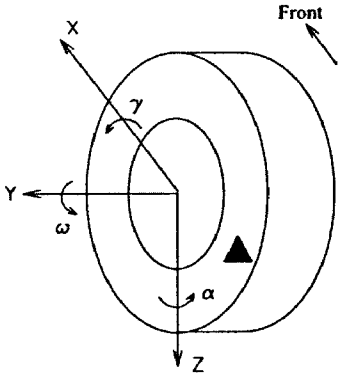 **Case 3** Impulse input is applied to the side of the sidewall of the tyre	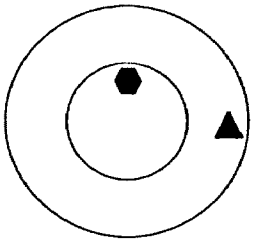 **Case 3A** Accelerometer at the 12 o'clock position on the wheel rim	33.7 Hz, 0.05859, large 41.5 Hz, 0.01462, small 82.0 Hz, 0.01583, medium (Refer to Figure 8.8)
	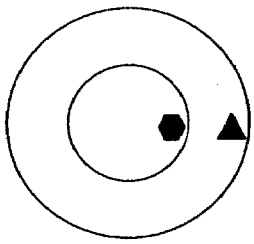 **Case 3B** Accelerometer at the 3 o'clock position on the wheel rim	24.9 Hz, 0.005344, medium 38.6 Hz, 0.02556, large 82.0 Hz, 0.004756, medium (Refer to Figure 8.9)
	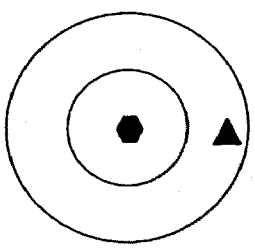 **Case 3C** Accelerometer is at the centre of the wheel	23.9 Hz, 0.0001122, small 38.1 Hz, 0.001671, medium 80.6 Hz, 0.002197, large (Refer to Figure 8.10

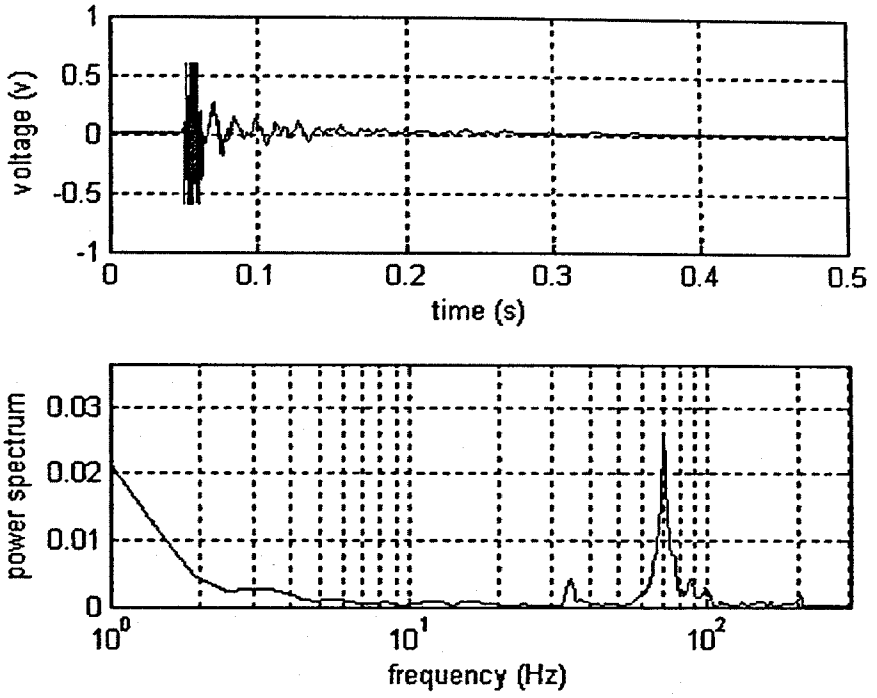

Figure 8.2 Test data from accelerometer in Case 1A

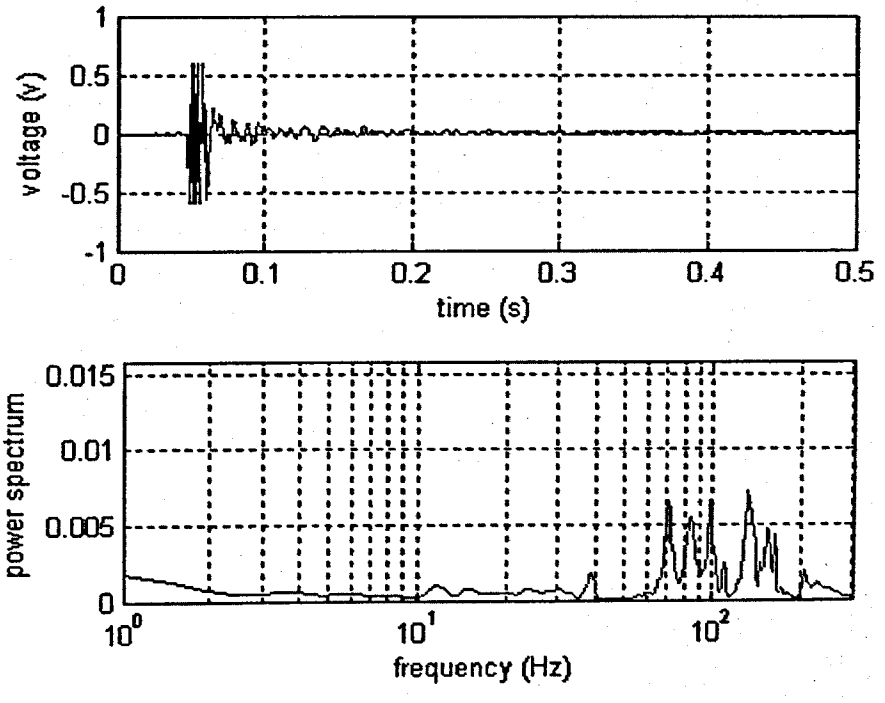

Figure 8.3 Test data from accelerometer in Case 1B

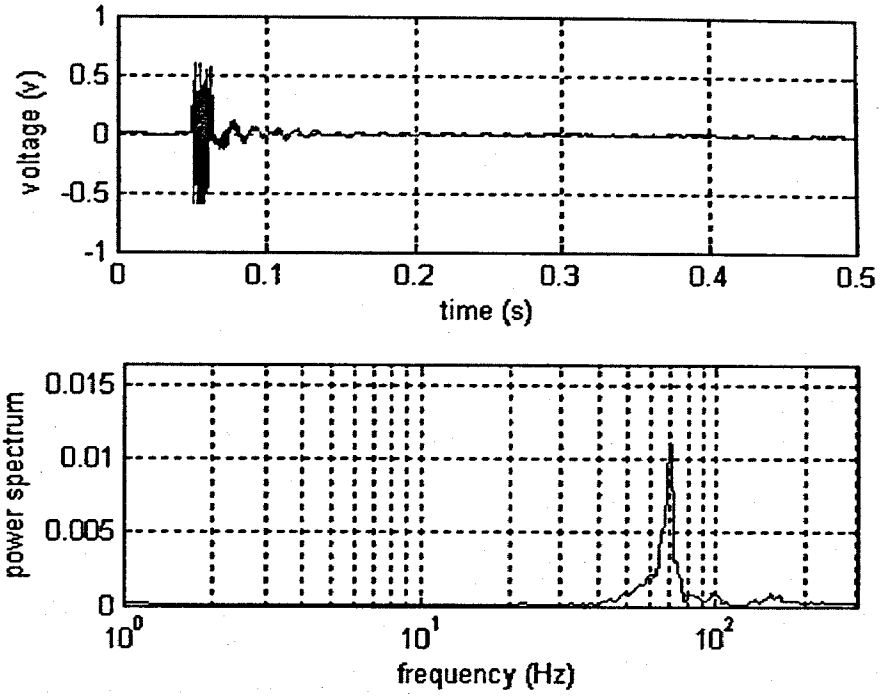

Figure 8.4 Test data from accelerometer in Case 1C

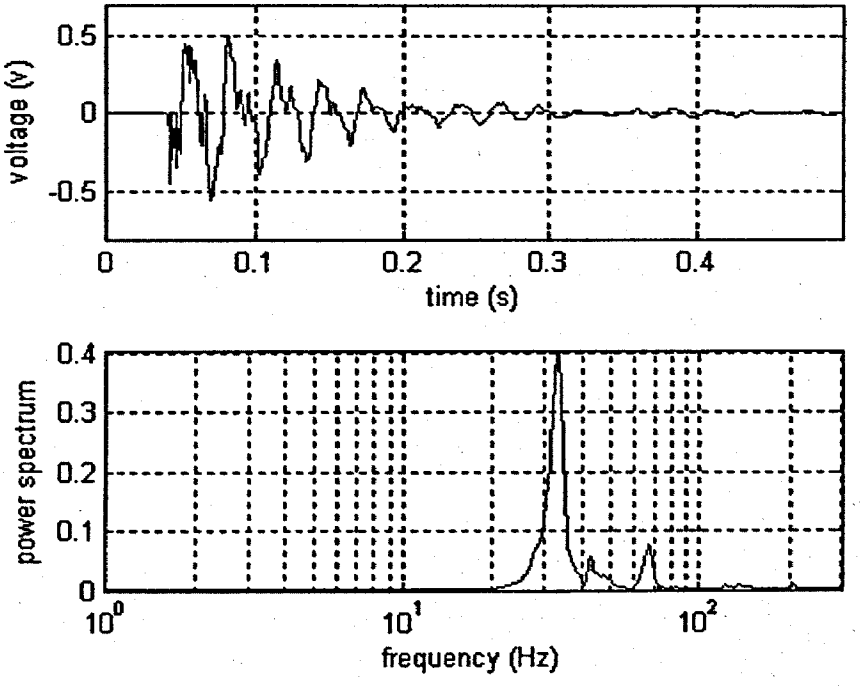

Figure 8.5 Test data from accelerometer in Case 2A

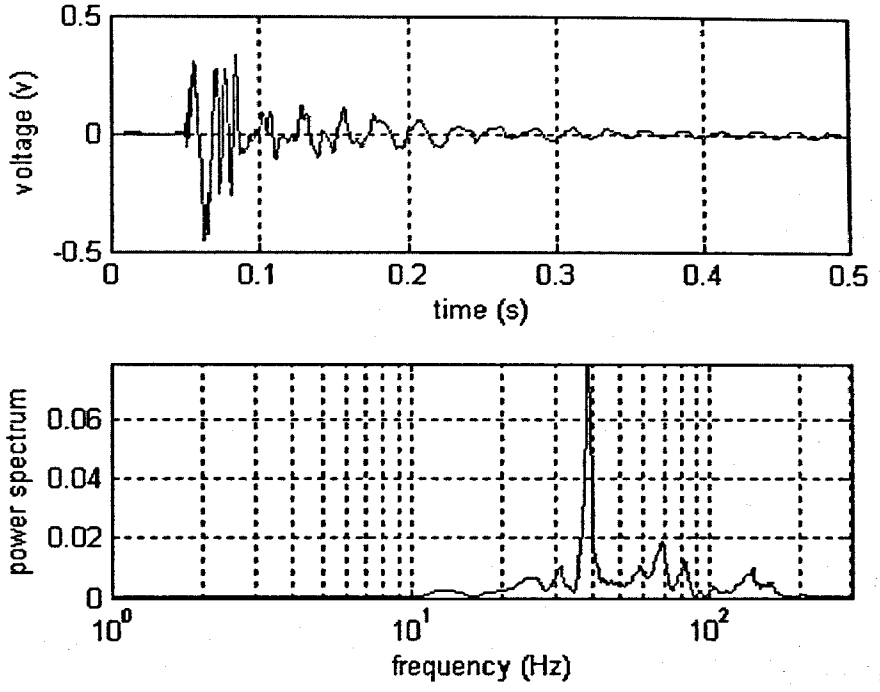

Figure 8.6 Test data from accelerometer in Case 2B

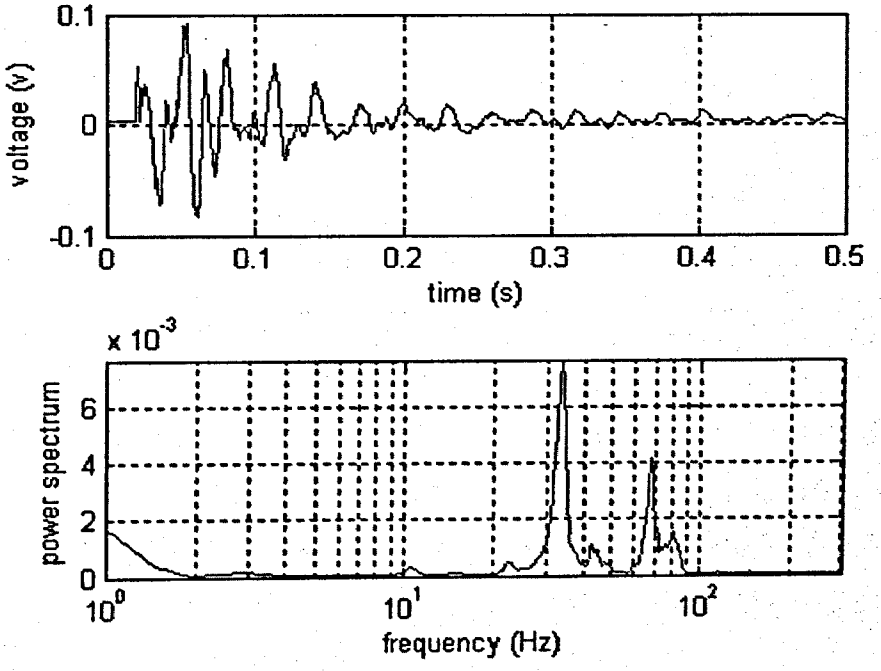

Figure 8.7 Test data from accelerometer in Case 2C

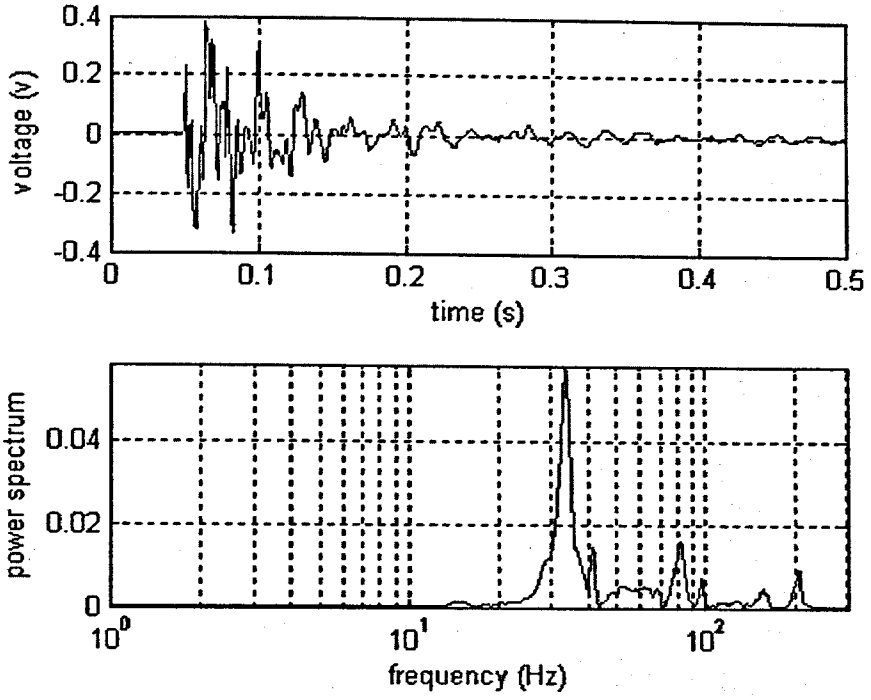

Figure 8.8 Test data from accelerometer in Case 3A

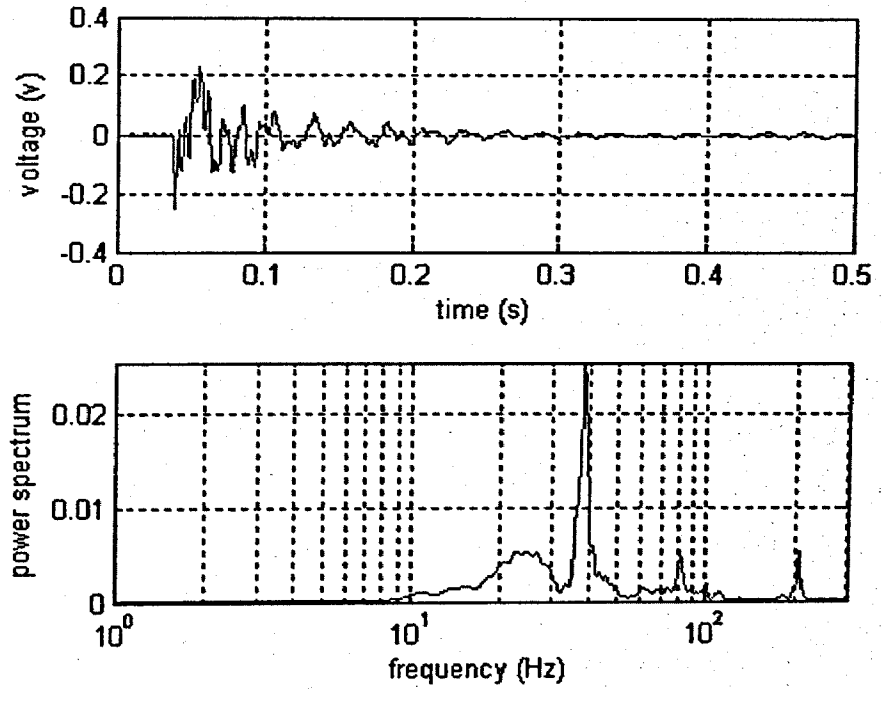

Figure 8.9 Test data from accelerometer in Case 3B

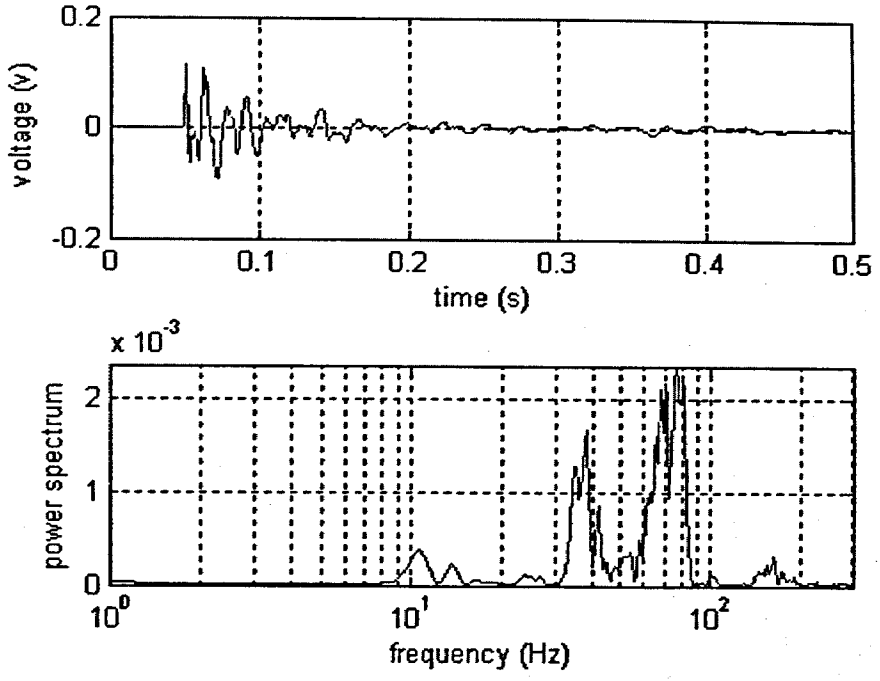

Figure 8.10 Test data from accelerometer in Case 3C

In summary, several main modes of the front wheel and tyre are obtained. From the testing, the frequency of the translation along the Y axis is about 70 to 80 Hz which confirms the free vibration analysis of this mode of the front wheel (refer to Figures 4.6 and 4.7, 72.85 Hz and 74.42 Hz). Furthermore, shown in Figure 4.3, the natural frequency dominated by the twist between the wheel and the contact patch of the tyre is about 21.45 Hz. The reasonable agreement (about 24 Hz in α direction) is obtained from the testing. Table 8.4 compares frequencies obtained from the free vibration analysis and the impact test. The test confirms the theoretical model and analysis. The impact test also describes the 33 Hz rotation in γ direction and the 40 Hz local vibration mode of the tyre. These frequencies of the front wheel and tyre are illustrated in Figure 8.11.

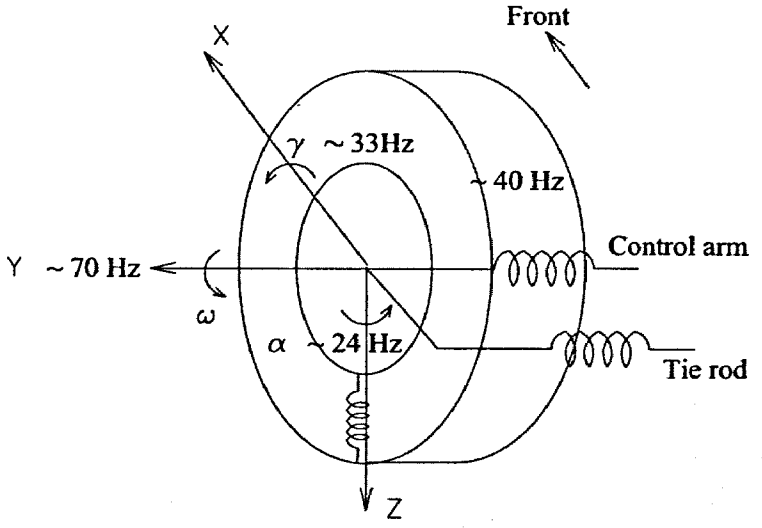

Figure 8.11 Vibration frequencies of the front wheel and tyre

Table 8.4 Comparison of free vibration analysis and impact test results

Free vibration analysis (Refer to Table 4.2)			**Test Results**
No.	**Natural Frequency (Hz)**	**Dominant Components**	**Natural Frequency (Hz)**
3	21.45	Two wheels and the contact patches of the tyres	About 24 Hz
6	72.85	Translational movement of two front wheels	About 70~80 Hz
7	74.42	Translational movement of two front wheels	About 70~80 Hz

8.3 Steering shudder testing

As discussed in the previous chapters, steering shudder is one of the main vibration problems of the hydraulic power steering system. The pressure sensors installed on the cylinder feeding pipes in the test rig were used to monitor the pressure change in the system. Before the steering shudder testing, the steering pump ran for 20 minutes to make the temperature of the steering fluid stabilise at about 50 °C. In each test, the steering wheel was quickly turned from neutral position to a large angle, say 360 degrees. Using different steering pump speeds, and the responses of the cylinder feeding line pressure were recorded.

The steering shudder, when the rotational speeds of the steering pump are 14, 16, 18 and 20 Hz, is shown in Figure 8.12 respectively. It is found that the time domain simulations shown in Figures 4.13 and 4.14 are in good agreement with the testing results, especially in the shudder frequencies.

Figure 8.13 shows the frequencies of the shudder under different steering pump speeds. The star symbol marks the raw test data, and the solid line is the polynomial curve fitted to the raw test data. It can be found that the frequency of the shudder is about 24 Hz, and it is not affected by the speed of the pump. The analysis in the previous chapters has found the low frequency shudder is dominated by the mechanical components of the system. Since the change of pump speed does not alter the characteristics of the mechanical components, the shudder frequency should not be affected by the pump speeds. The experimental result shown in Figure 8.13 confirms the time domain simulation and frequency domain analysis in the previous chapters (refer to Figure 4.14 and Table 5.2), and it concludes that the steering shudder is mainly generated by the mechanical subsystem and its frequency is around 22 Hz.

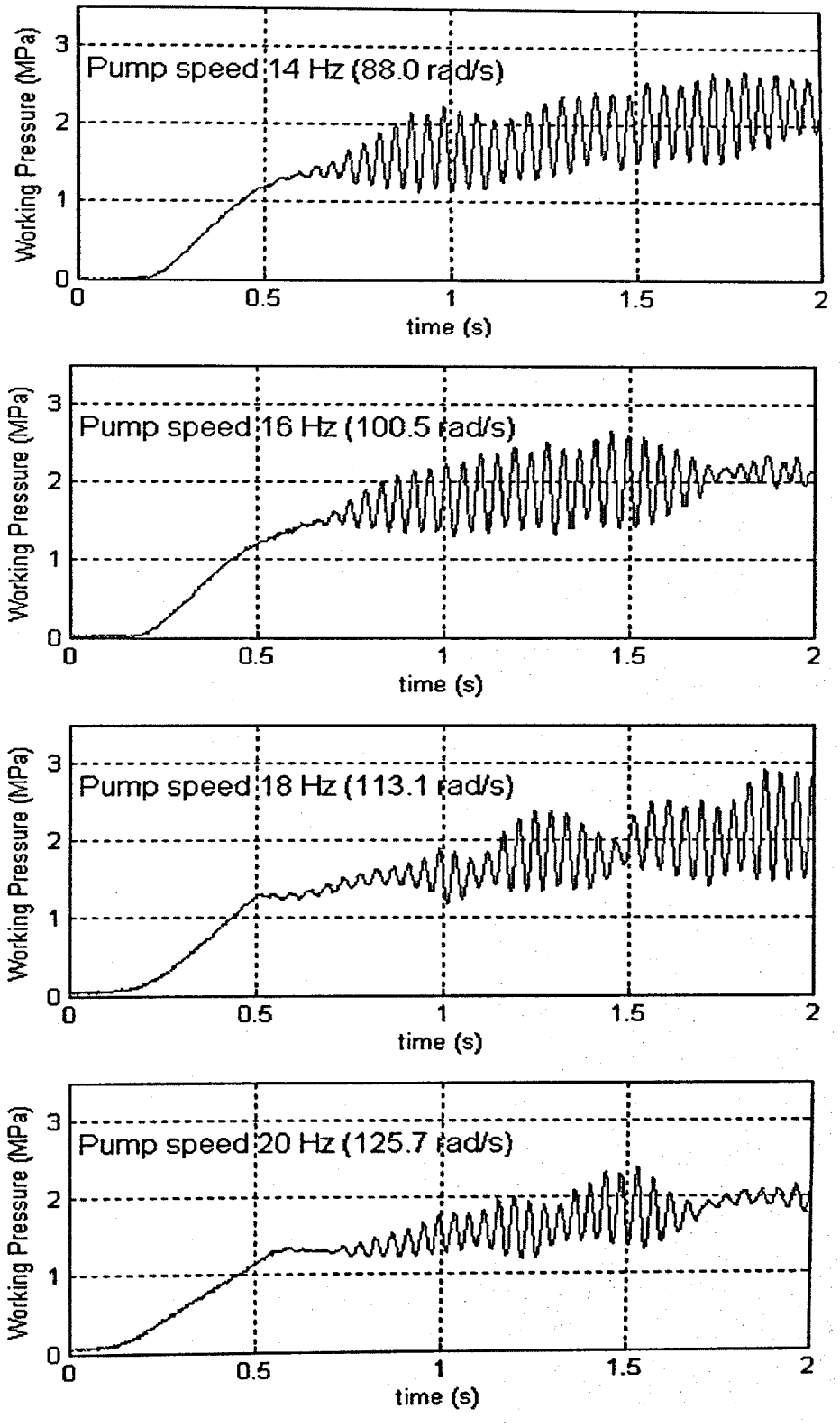

Figure 8.12 Test data of steering shudder

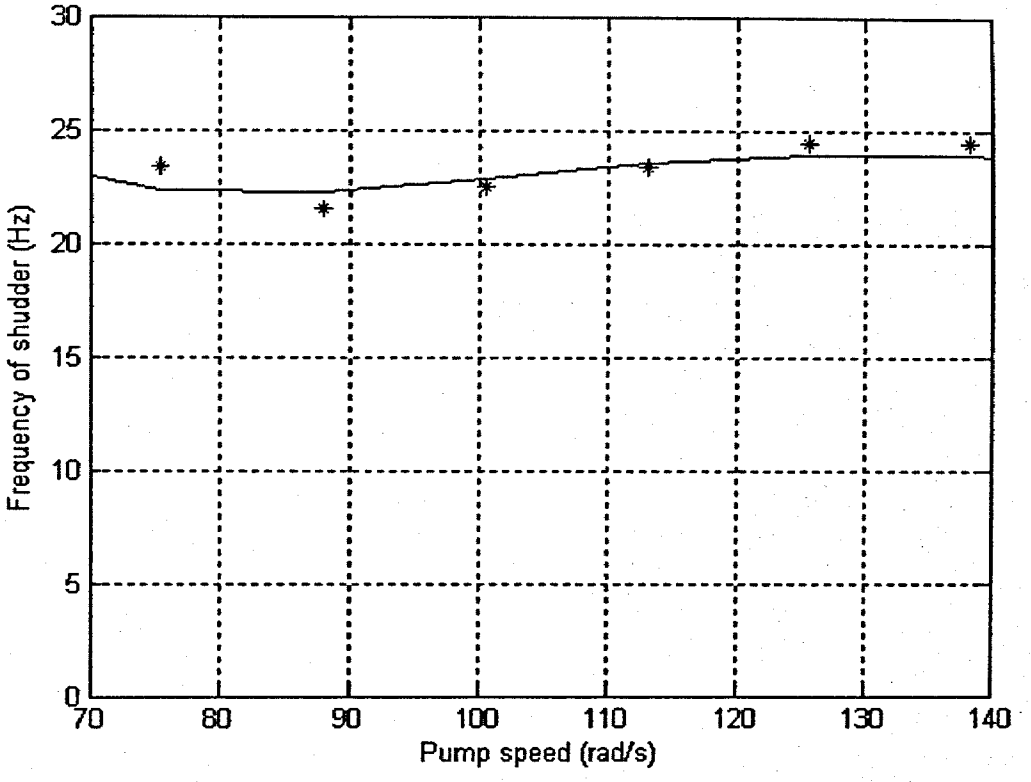

Figure 8.13 Frequency of steering shudder under different steering speeds

Figure 8.14 shows the signal of the accelerometer when the steering shudder is present. For this measurement, the accelerometer is mounted on one side of the wheel rim (Position B). According to Figure 8.14, the two main frequency components are 20.0 Hz and 41.0 Hz, and a component at 31.3 Hz frequency is also noticeable. It is believed that the 20.0 Hz is related to the twist effect of the front wheel and tyre. The difference between the measured result and free vibration analysis may be due to the high damping level in the tyre for this vibration mode. The 31.3 Hz and 41.0 Hz are

related to an incline mode of the wheel and a local mode of the tyre respectively. This measurement affirms the results of the impact testing.

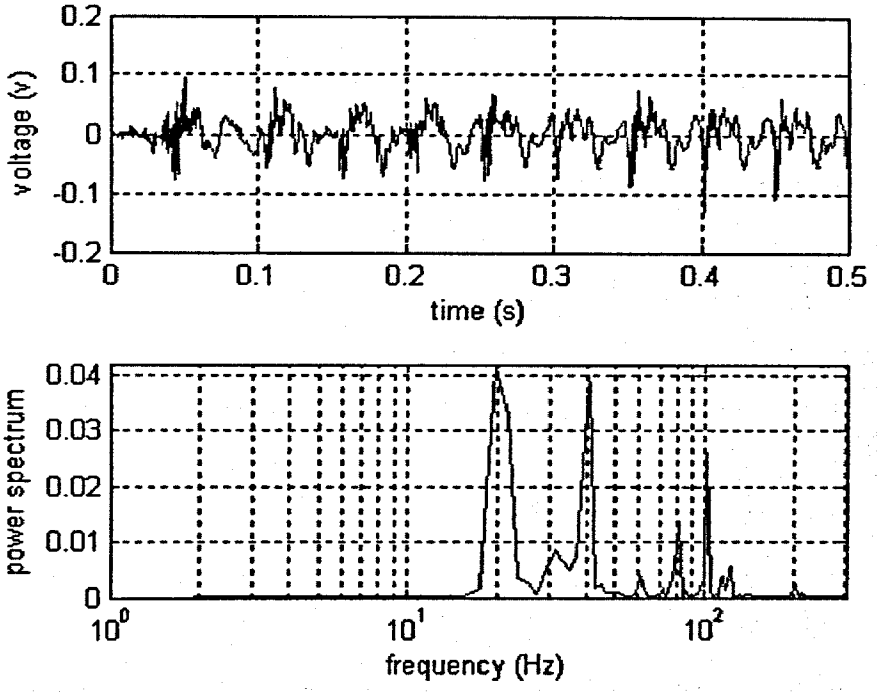

Figure 8.14 Test data from accelerometer during steering shudder

8.4 Pressure ripple testing

In order to study the dynamic characteristics of the mechanical and hydraulic coupled system, the high frequency pressure ripple in the hydraulic power steering system was also investigated in the testing, although the effect of the ripple was not as significant as that of the steering shudder.

In the pressure ripple testing, using different steering pump speeds, the steering wheel was slowly turned, and a small angular displacement of the tyres was generated. Figure 8.15 shows the cylinder feeding line pressures when the rotational speeds of the

steering pump were 14, 16, 18 and 20 Hz. The pressure ripples after 1.5 seconds were considered as the steady state responses, and the amplitudes of the ripples were recorded.

Figure 8.16 shows the amplitudes of the pressure ripple against the different pressure ripple frequencies that are ten times the rotational speeds of the steering pump due to the ten vanes. The star symbol marks the test data, and the solid line is the polynomial curve fitted to the test data. It can be seen that the amplitude of the ripple has a peak when the ripple frequency is about 942.5 rad/s (150 Hz). In Chapter 4, the time domain simulation of the steering system finds a resonance frequency at about 970 rad/s which is shown in Figures 4.18 to 4.20. Also, in the frequency domain analysis of Chapter 5, the couple natural frequency at about 969.09 rad/s is found. The testing result generally supports the time domain and frequency domain analysis and verifies the comprehensive mathematical model of the hydraulic power steering system developed in this thesis.

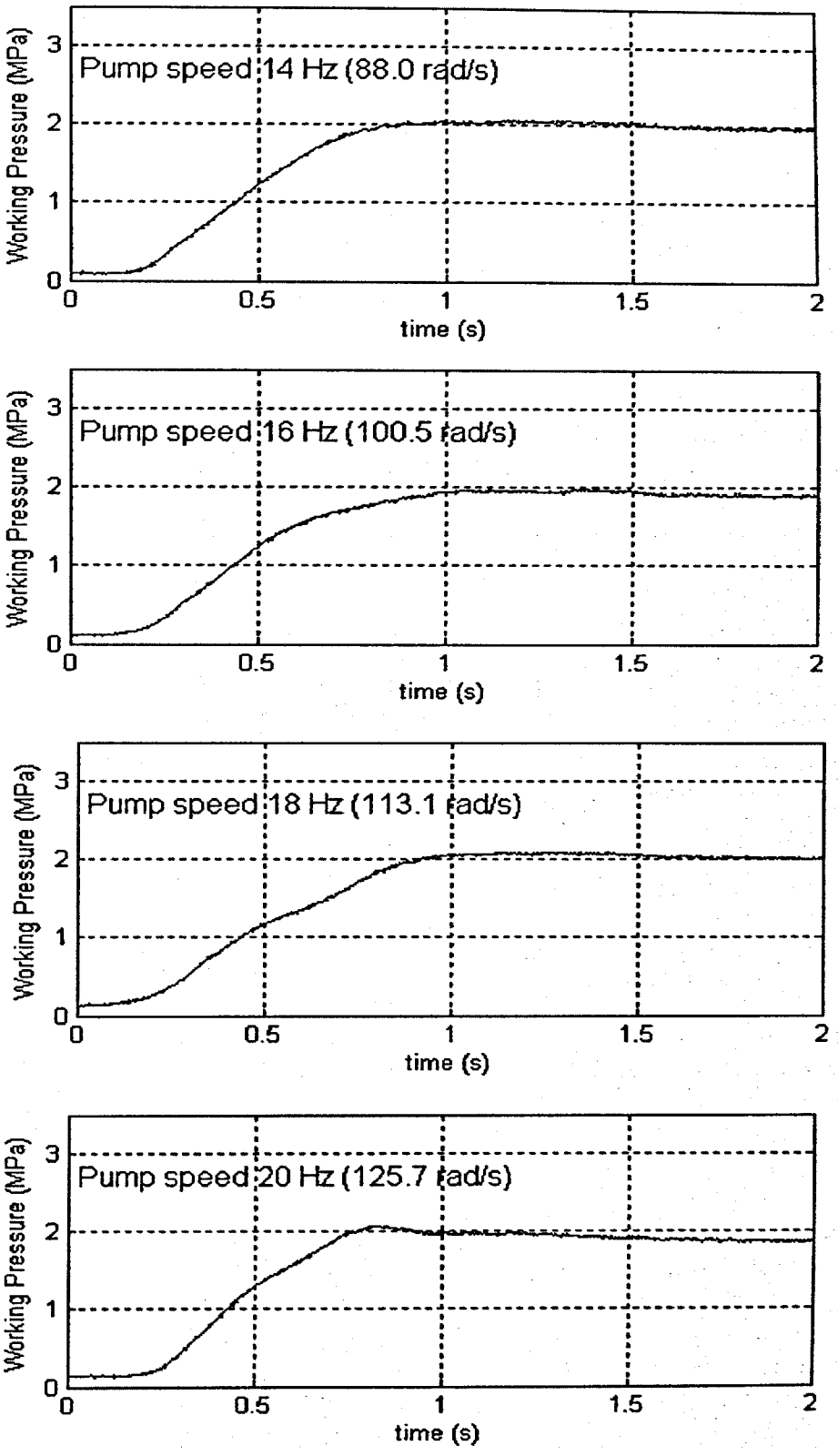

Figure 8.15 Cylinder feeding line pressure with a slow steering wheel input

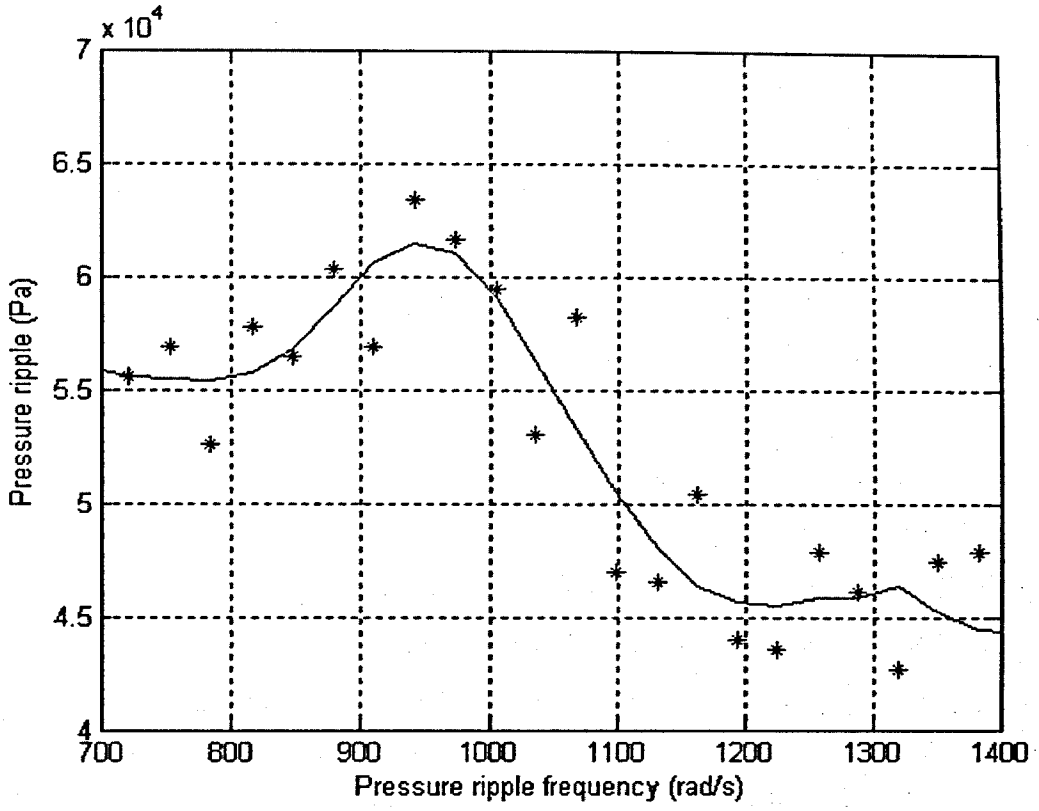

Figure 8.16 Amplitude of pressure ripple with different ripple frequencies

CHAPTER 9 SUMMARY AND CONCLUSION

9.1 Summary

The dynamic characteristics of a typical rack and pinion hydraulic power steering system are investigated analytically and experimentally in this thesis. At first, the latest discoveries and studies about the NVH phenomena of hydraulic power steering systems are reviewed, and the general causes of vibration problems are classified and discussed. Also, a good understanding of the physical components of the steering system is gained. After that, the comprehensive mathematical models of the steering system for free and forced vibration analysis are developed.

Due to the complexity of the system, models of the mechanical subsystem and the hydraulic subsystem are derived separately at first. Both the frequency domain analysis and the time domain analysis are conducted based on the two subsystem models.

By simplifying the components to lumped masses or mass moments of inertia connected by linearised springs and dampers, a 12 DOF model that describes the dynamics of the mechanical elements of the steering system is developed. The model includes steering wheel, input shaft, torsional bar, rack and pinion gear, tie rod linkages, front wheels and tyres. The natural frequencies and the corresponding mode shapes of the mechanical subsystem are determined from the eigenvalue and eigenvector analysis. The hydraulic subsystem model consists of the high pressure supply line, the rotary spool valve and the hydraulic cylinder/piston unit. The transfer matrix method is adopted to construct the supply line model after the transfer matrix of every single section of the supply line is obtained from a one dimensional hydraulic impedance model. The rotary spool valve is regarded as a four-way open centre valve, and in the model, the governing equations of the valve determine the physical relationships between the supply line and the hydraulic cylinder.

The mathematical models of the mechanical subsystem and the hydraulic subsystem are integrated in a comprehensive system model by introducing the couplings between the mechanical and hydraulic components. One of the main interactions is the twist angle of the torsional bar controling the valve opening angle. Also, the flow rate and pressure fluctuations in the supply line alters the operating pressure inside the

hydraulic cylinder, and therefore alters the external force of the mechanical subsystem and induces vibration in the torsional bar. The transient responses of the steering system are generated by numerical calculation of the time domain model of the integrated system. Low frequency steering shudder and high frequency pressure ripple are illustrated in the simulation.

After the rotary spool valve is modelled using branch impedance method, the global transfer matrix of the hydraulic subsystem is obtained. The natural frequencies of the subsystem are calculated from the global matrix. Then, an innovative derivation transforms the transfer matrix of the hydraulic subsystem to a state vector form and paves the way to establish a system matrix of the whole steering system. The root searching technique is adopted to determine the natural frequencies of the system. The results obtained in the frequency domain analysis are compared to those obtained from the time domain analysis, and the natural frequencies which are dominated by the mechanical components, the hydraulic components or the coupling effect are determined.

Based on the steering system model, the variable ratio steering system and speed sensitive system are studied and the special features of the two steering systems are presented.

A hydraulic power steering system test rig, which provides approximately realistic working environment for the hydraulic steering system, is designed and built to validate the presented mathematical models. A series of experiments including impact testing on the front wheel, steering shudder testing and pressure ripple testing are carried out. The computer simulation based on the mathematical models has good agreement with the testing results.

9.2 Limitations and future work

One of the limitations of the presented study is the linearisation of the mechanical subsystem. In the mathematical model, the complex mechanical components of the system are simplified as lumped masses or mass moments of inertia, and linear springs

and dampers are used to connect these components. Although these linearised mechanical models are adequate to investigate the mechanical-hydraulic coupling, more detailed nonlinear models are required if the dynamic characteristics of a special component, such as the tyre, are the main research concern.

Another limitation of this research is that a one-dimensional linear resistance compressible model is used in the fluid circuit of the steering system and the parameters of the hydraulic oil, like density, fluid bulk modulus and viscosity, are constants. These assumptions are valid when the hydraulic power steering system works in normal conditions and the temperature of the oil is stable, say 50 °C. But further considerations should be taken if extreme applications are studied.

In the future, more complex distributed parameter models, such as a two-dimensional viscous compressible flow model, could be integrated into the steering system if more details of the fluid dynamics in the supply line's cross-section plane are the research interests. By using an eight-equation model [Tijsseling, 1996], more fluid-structure interaction, such as the junction coupling at the bends of the pipes, could be introduced to analyse the vibration of the pipes and hoses. The CFD (Computational Fluid Dynamics) method is suggested if more details of the fluid dynamics in the rotary spool valve are required. But it should be noted that access of the details to the valve edge profiles, which is essential to this analysis, is usually restrained by commercial confidentiality.

The parameters used in this thesis are from steering system manufactures and literatures, and they have been proved to be valid and correct. But, more practical parametric studies will assist the research on hydraulic steering systems if the required experiment resources are available. With further parametric studies, some key components could be improved and the model of steering systems could be further generalised.

9.3 Conclusion

This thesis presents the dynamic analysis and the laboratory based testing for the dynamic characterisation in the frequency domain and the transient analysis in the time domain of hydraulic power steering systems. The mathematical models, computer simulation and experimental validation of a power steering system with typical dimensions and configuration lead to the following conclusions:

1. The transient and steady states, such as the displacement of mechanical elements, pressures and flow rates of fluid elements, of a power steering system under various operating conditions can be determined through a numerical procedure. In this procedure, the mechanical subsystem dynamics are governed by a set of linear differential equations and the dynamic states of fluid elements of the hydraulic subsystem are modelled using the transfer matrix method. The dynamic interactions between the two subsystems are integrated. The fluid subsystem applies loads to the mechanical subsystem and the resulting mechanical states in turn change the operating conditions of the fluid system. The low frequency steering shudder (about 21 Hz) is simulated by the mathematical model, and it matches the free vibration analysis of the mechanical subsystem which found the pinion and the front wheels have significant effects on the steering shudder. However, the time domain simulation shows the high frequency pressure ripple has a resonance at a frequency which is neither the natural frequency of the steering column nor the natural frequency of the pinion. It is found that significant dynamic coupling between the mechanical and fluid subsystems exists in the hydraulic power steering system, in particular about 154 Hz. Numerical calculation offers a convenient approach for time domain analysis of the steering system while it is limited in use for frequency domain analysis.

2. The state space representation of a power steering system, in which the translational and angular displacements of mechanical elements, their corresponding velocities and pressures in the fluid circuits are combined into the system state vector, describes the coupled dynamic characteristics effectively. The system natural frequencies and modal shapes can be determined from a root search numerical computation scheme. After the study of the global matrix of the hydraulic subsystem excludes the possibility that the

pressure ripple resonance is the natural frequency of the hydraulic circuit, the frequency domain analysis of the coupled matrix finds the natural frequencies of the integrated system. Compared to free vibration analysis of the mechanical subsystem, the investigation demonstrates that in low frequency range (under 100 Hz) the system dynamics are dominated by the mechanical subsystem and in high frequency range (above 200Hz) the system dynamics are mainly dominated by the hydraulic subsystem. The sensitivity analysis of the key parameters, including the volume of the hydraulic cylinder and the area of the piston, confirms the frequency domain analysis. Between 100 Hz and 200 Hz, the frequency domain analysis locates the system natural frequency, 154 Hz, which is caused by the coupling between the mechanical components and the hydraulic components. This analysis explains the offset of the system natural frequency found in the time domain simulation.

3. The impact testing on the steering system test rig obtains the main vibration mode of the front wheels, which has an important effect on steering shudder. It also confirms the free vibration analysis of the mechanical components. The steering shudder testing validates the time domain simulation and the result of the pressure ripple measurement is close to the frequency domain analysis of the whole steering system.

The presented methods for the analyses in both time and frequency domains of a hydraulic steering system provide thorough understanding of the dynamic characteristics of the hydraulic power steering system, especially the coupling between the mechanical components and the hydraulic components. The models and test rig may assist automotive engineers to perform theoretical noise and vibration analysis of the system to optimise its performance. Furthermore, the presented modelling methods and numerical solution scheme which reveal the mechanical and hydraulic coupling action can be applied to the analysis of dynamics of other complex mechanical/hydraulic systems.

APPENDIX Drawings of the steering system test rig

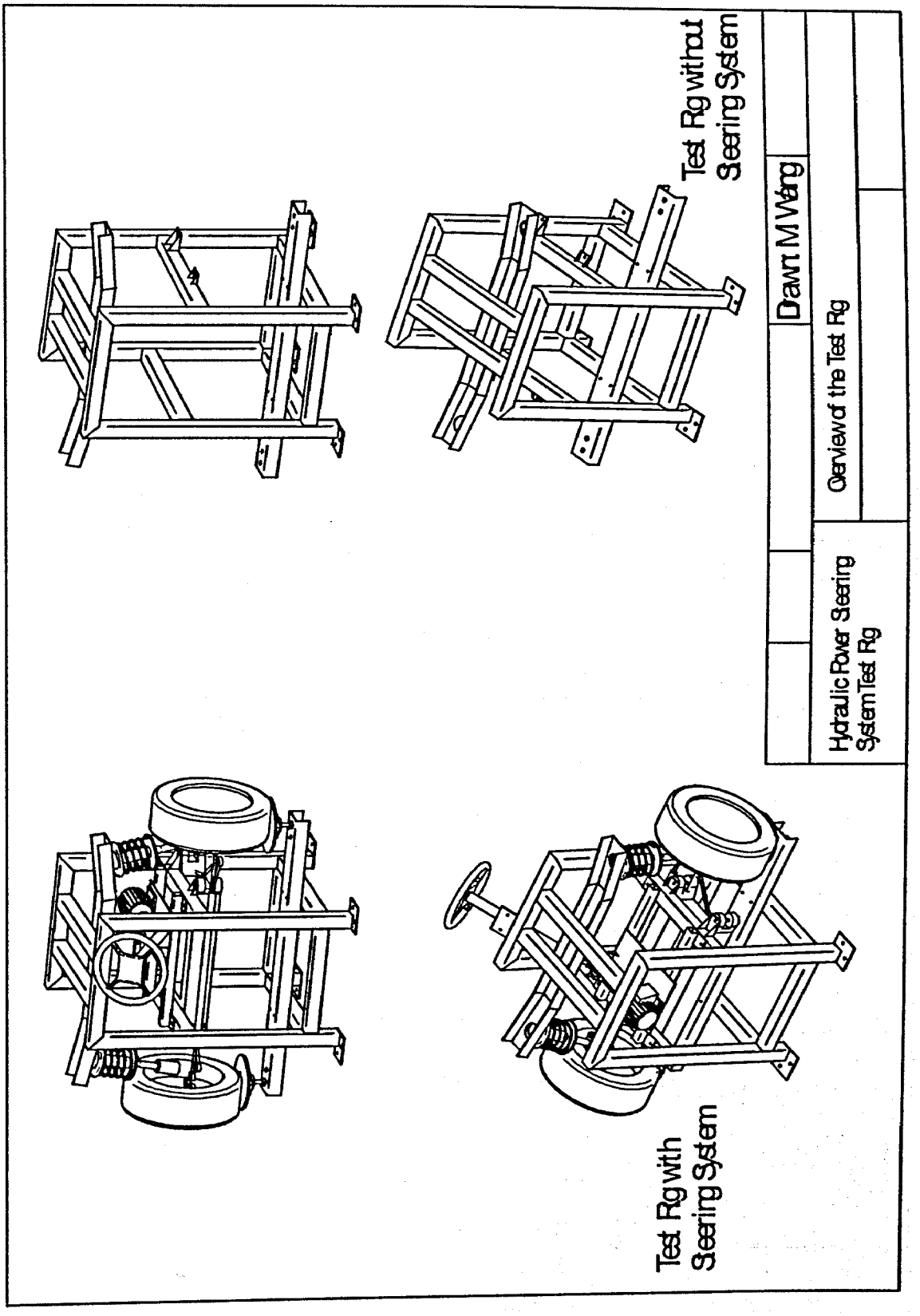

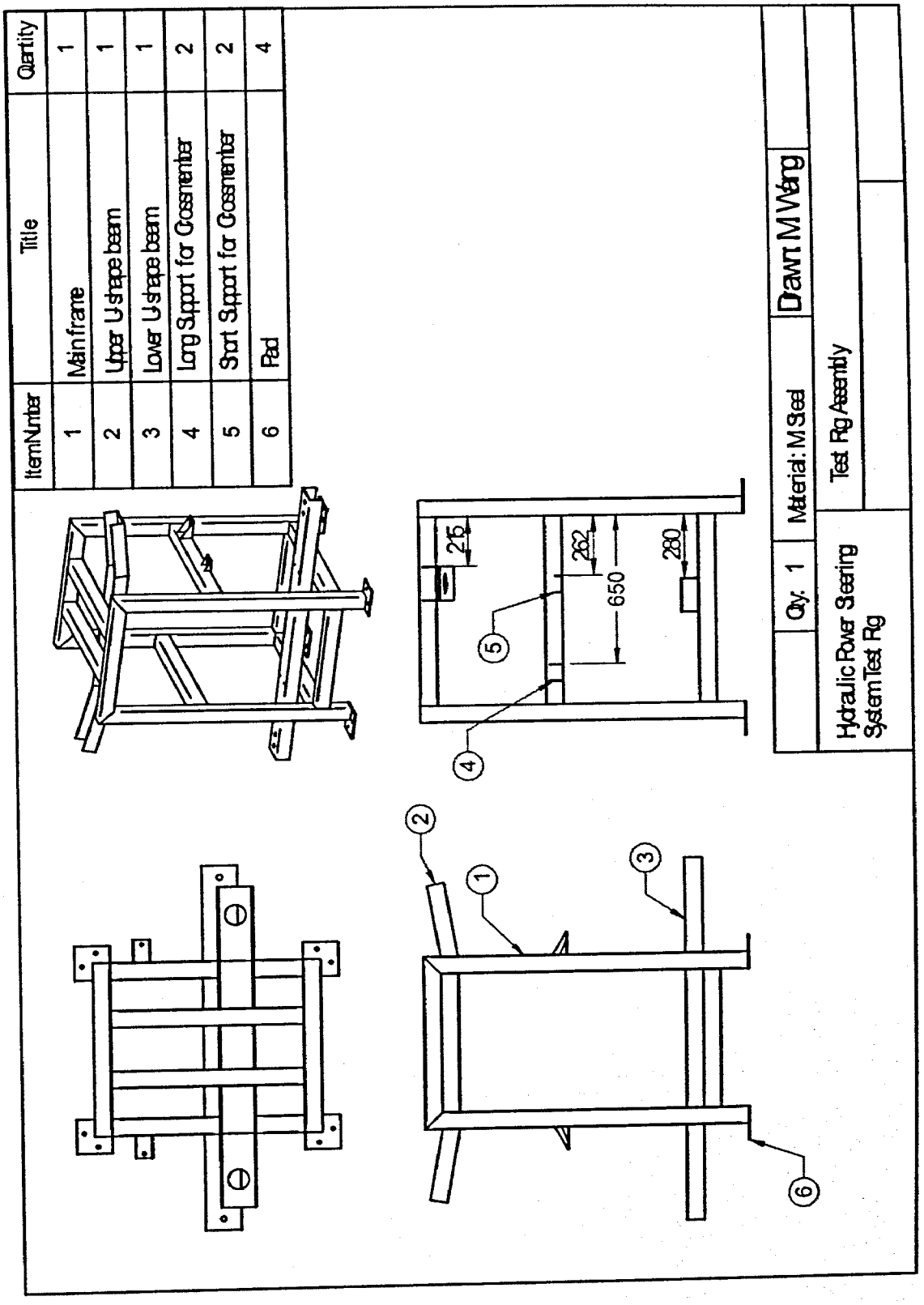
ItemNumber
Title
Quantity
1
Mainframe
1
2
Upper Ushape beam
1
3
Lower Ushape beam
1
4
Long Support for Crossmember
2
5
Short Support for Crossmember
2
6
Pad
4
215
262
280
650
Qty. 1
Material: MSteel
Drawn MWang
Hydraulic Power Steering System Test Rig
Test Rig Assembly

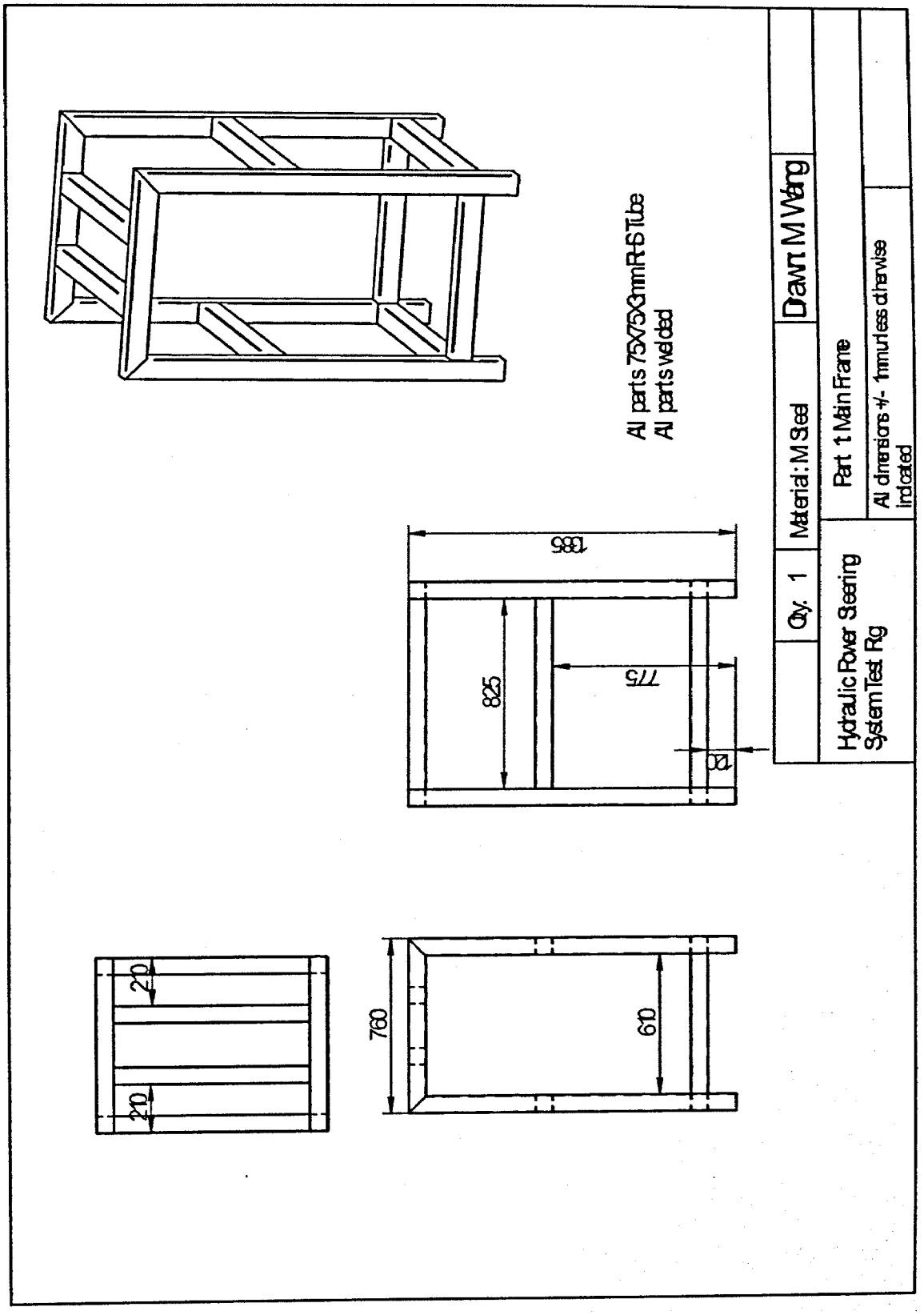
All parts 75X75X3mmRHSTube
All parts welded
Drawn M Wang
Material: M Steel
Qty. 1
Part 1 Main Frame
All dimensions +/- 1mm unless otherwise indicated
Hydraulic Power Steering System Test Rig
980
825
775
80
760
610
210
210

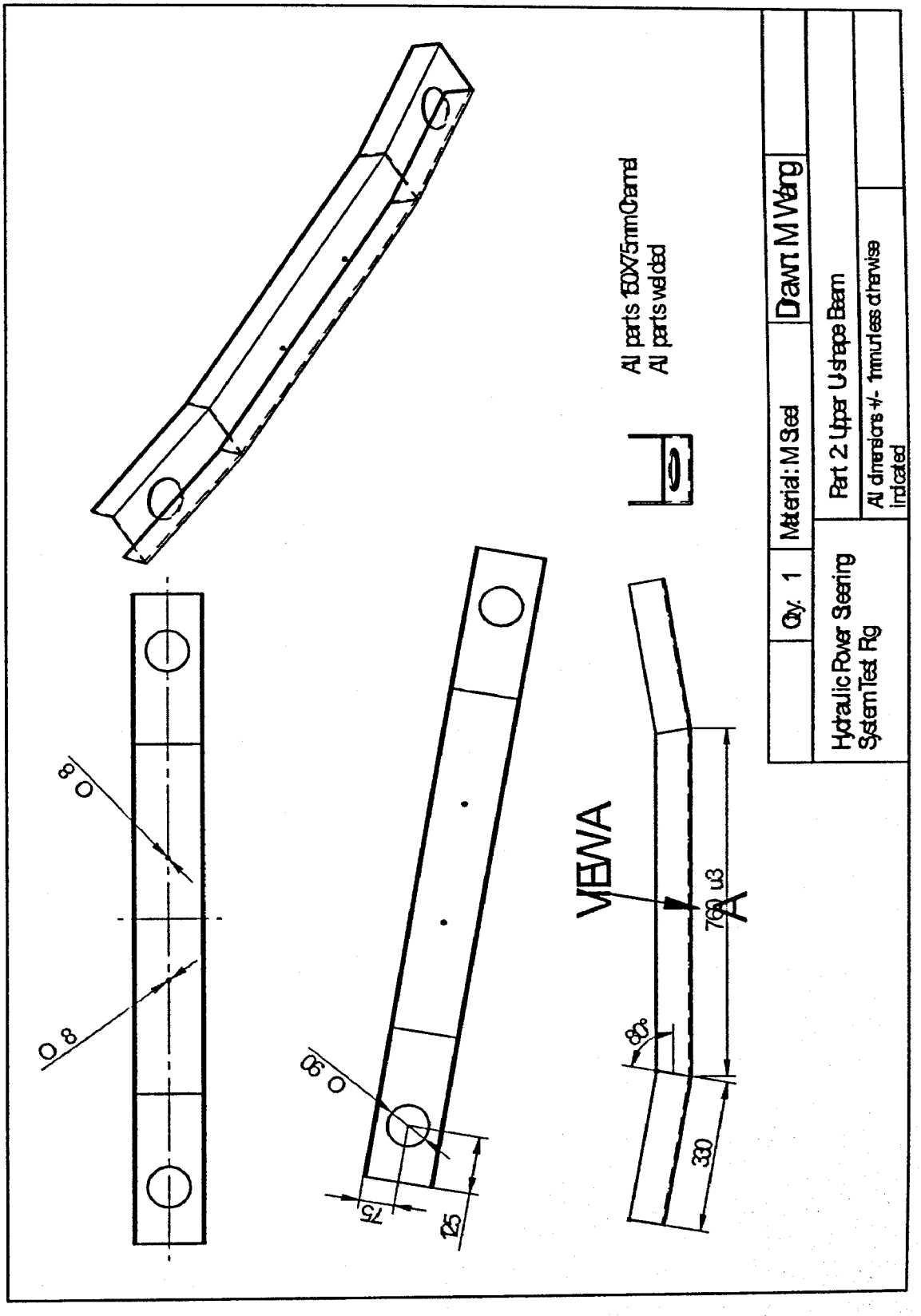
All parts 150X75mm Channel
All parts welded
VIEW A
Qty. 1
Material: M Steel
Drawn M Wang
Part 2 Upper U shape Beam
All dimensions +/- 1mm unless otherwise indicated
Hydraulic Power Steering System Test Rig
80
80
90
75
125
330
760
8°

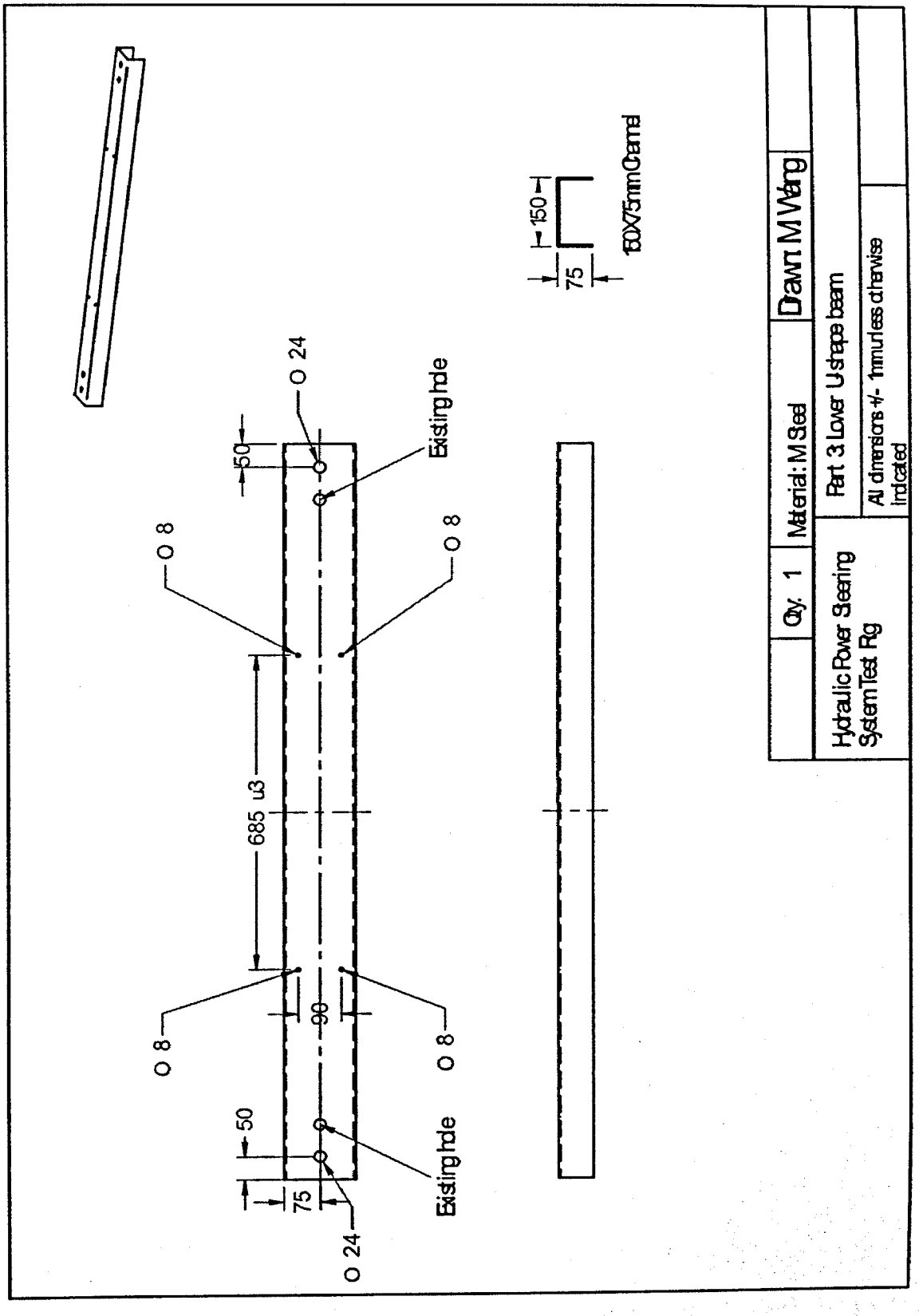
150
75
150X75mm Channel
O 24
Existing hole
50
O 8
O 8
685
90
O 8
O 8
50
75
Existing hole
O 24
Qty. 1
Material: M Steel
Drawn M Wang
Hydraulic Power Steering System Test Rig
Part 3 Lower U shape beam
All dimensions +/- 1mm unless otherwise indicated

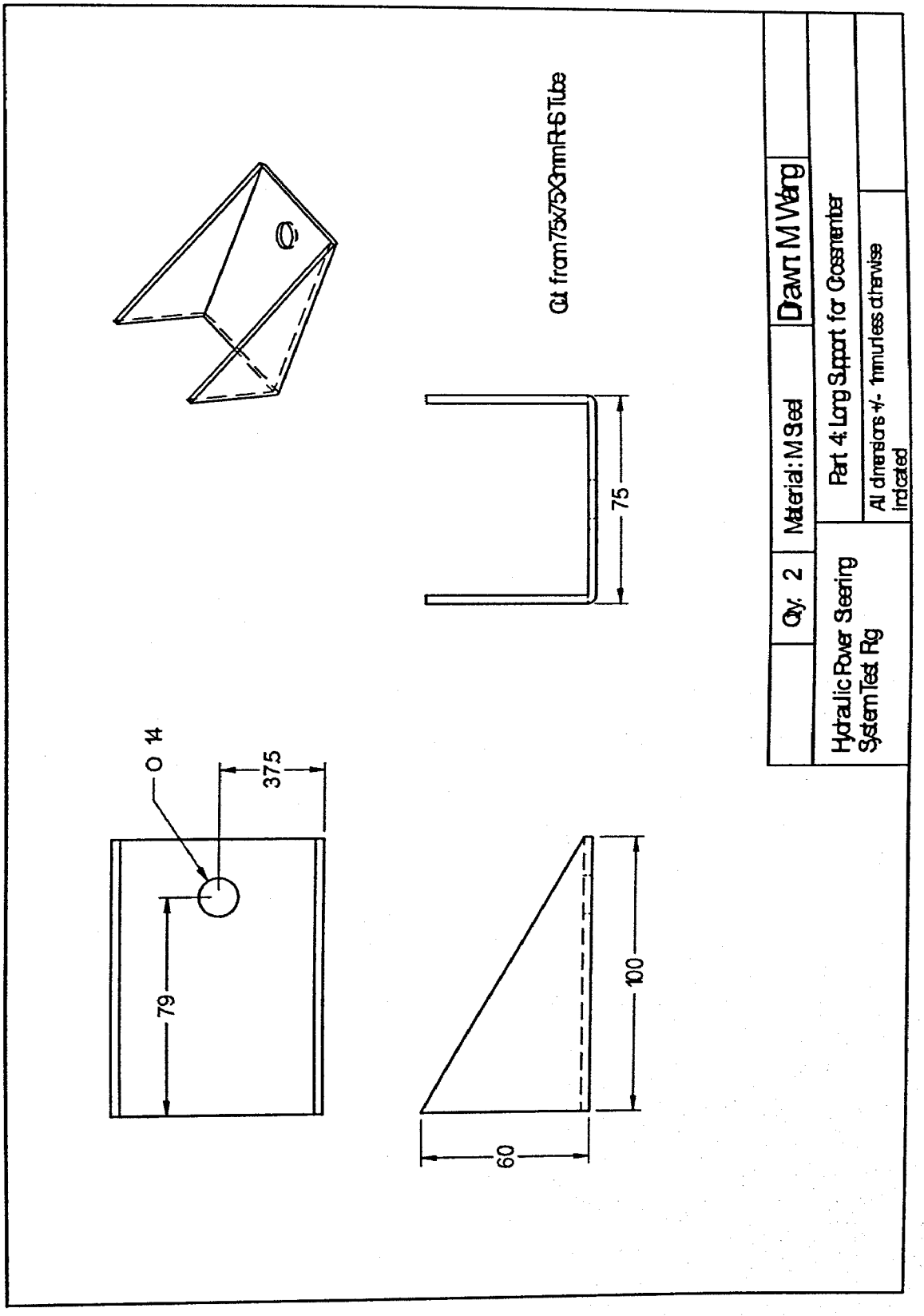
Cut from 75x75x3mm RHS Tube
75
O 14
37.5
79
100
60
Hydraulic Power Steering System Test Rig
Qty. 2
Material: M Steel
Dawn M Wang
Part 4: Long Support for Crossmember
All dimensions +/- 1mm unless otherwise indicated

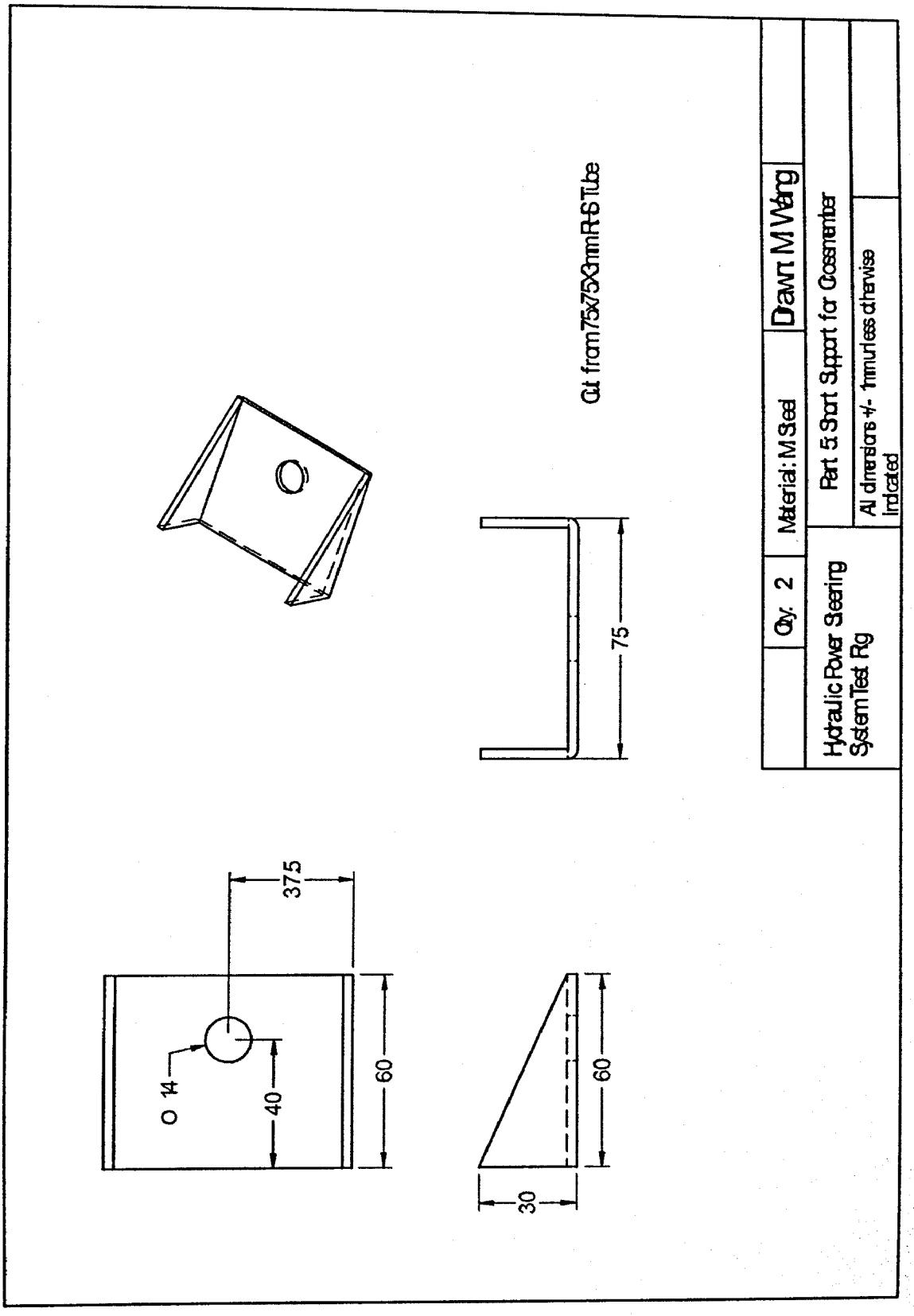
Cut from75x75X3mmRSTube
75
37.5
O 14
40
60
60
30
Hydraulic Power Steering System Test Rig
Qty. 2
Material: M Steel
Drawn M Wang
Part 5 Short Support for Crossmember
All dimensions +/- 1mm unless otherwise indicated

Item Number	Title	Quantity
1	Disk for Tyre	1
2	Holder	1
3	Bolt	1

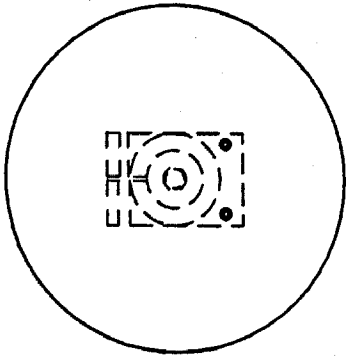

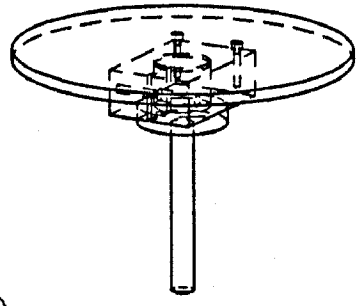

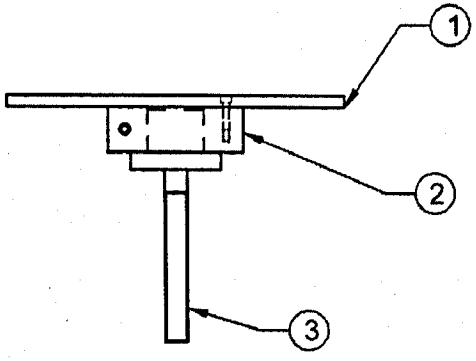

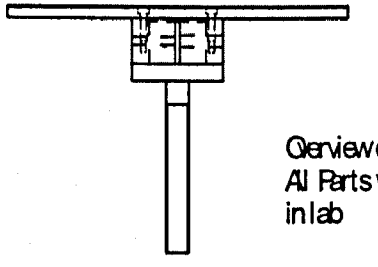

Overview of the tyre support assembly
All Parts will be assembled by bolts and nuts in lab

	Qty: 2	Material: M Steel	Drawn: M Wang	
Hydraulic Power Steering System Test Rig	Tyre Support Assembly			

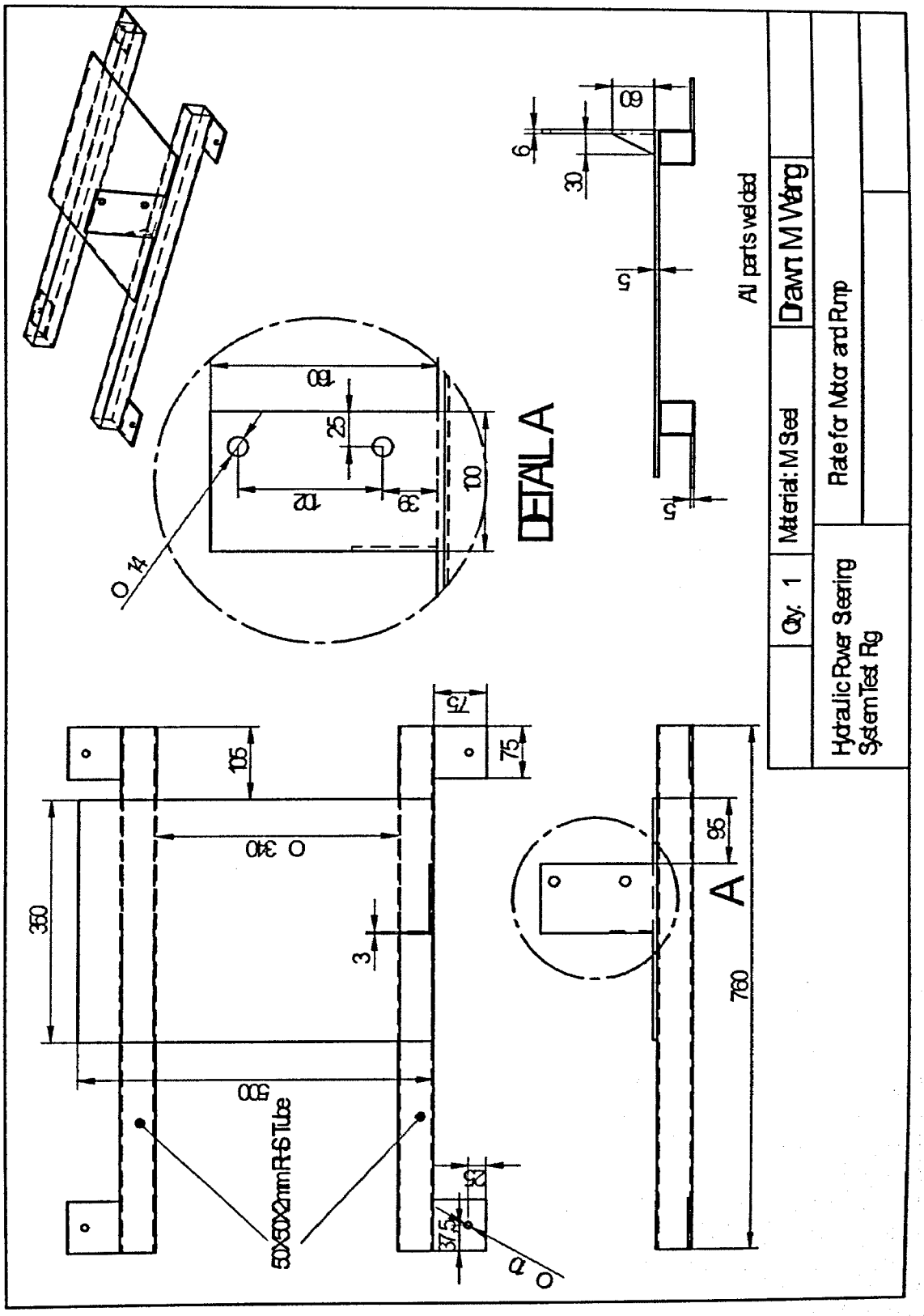
DETAIL A
All parts welded
Qty. 1
Material: M Steel
Drawn M Wang
Rate for Motor and Pump
Hydraulic Power Steering
System Test Rig
50X50X2mm RHS Tube
760
350
330
105
95
75
60
25
38
100
30
6
5
3
37.5
A

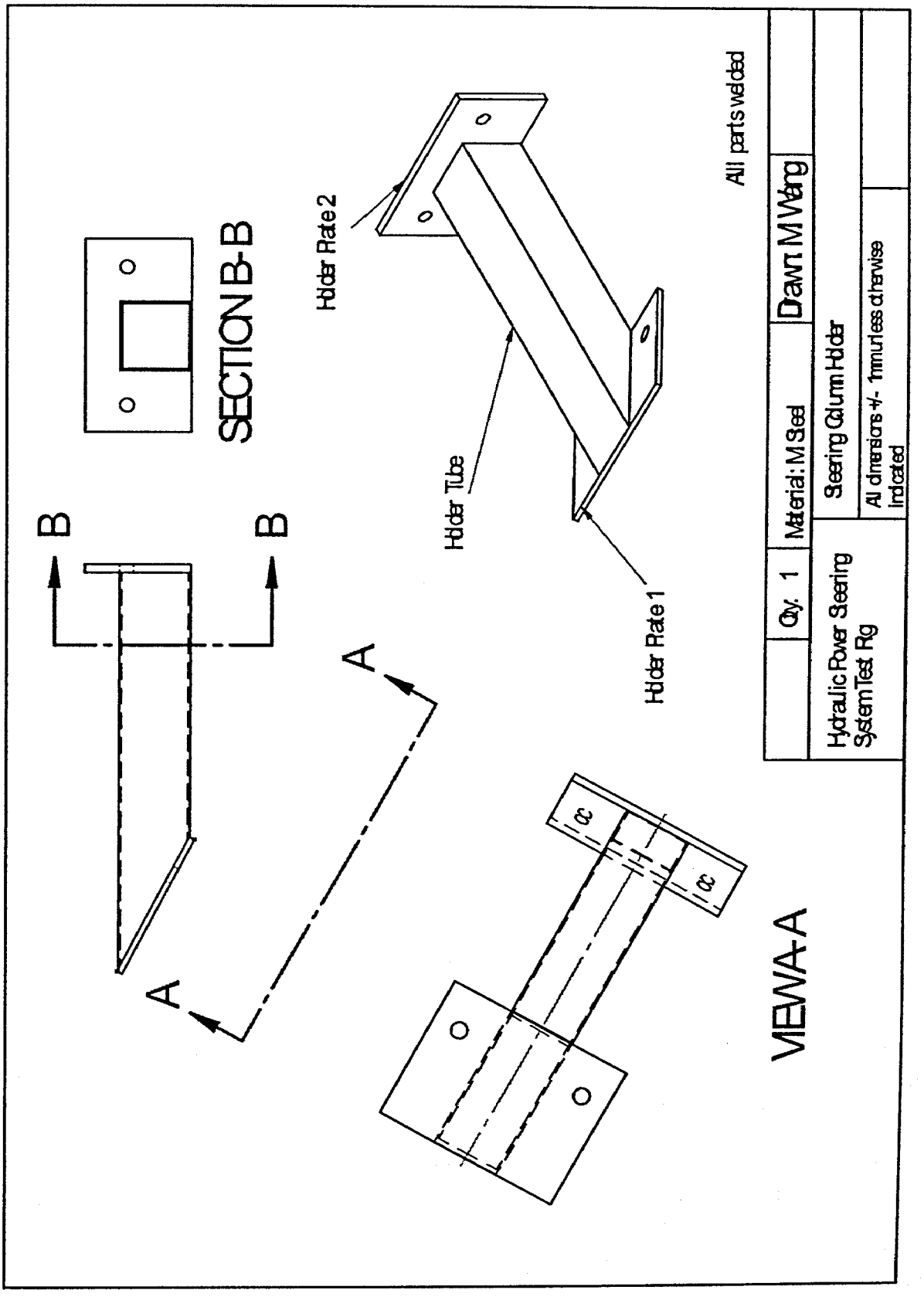
SECTION B-B
B
B
A
A
VIEW A-A
Holder Rate 2
Holder Tube
Holder Rate 1
All parts welded
Qty. 1
Material: M Steel
Drawn M Wang
Steering Column Holder
Hydraulic Power Steering System Test Rig
All dimensions +/- 1mm unless otherwise indicated

References

Adams, W.K. and Topping, R.W. (2001). "The steering characterizing functions (SCFs) and their use in steering system specification, simulation and synthesis," SAE Technical Paper Series 2001-01-1353.

Andersen, T.O., Hansen, M.R. and Ennemark, P. (2003). "Stabilization of a hydraulic steering unit OSPF," Bath Workshop on Power Transmission & Motion Control (PTMC 2003), pp. 165-182.

Baxter, J. (1988). "Analysis of stiffness and feel for a power-assisted rack and pinion steering gear," SAE Technical Paper Series 880706.

Baxter, J. and Dyer, G.P. (1988). "Bishop VARIATRONIC power steering system," SAE Technical Paper Series 880708.

Chen, C.C. (2001). "An investigation of noise and vibration in an automotive power steering system," PhD Thesis, The Ohio State University, US.

Delphi, 2004. General information of Delphi rack and pinion gears.

Drew, J.E., Longmore, D.K. and Johnston, D.N. (1994). "The noise characteristics of power steering systems," International Conference of Vehicle NVH and Refinement, 3, pp.167-176.

Drew, J.E., Longmore, D.K. and Johnston, D.N. (1995). "The systematic design of low noise power steering systems," The 4th Scandinavian International Conference on Fluid Power, pp.1195-1206.

Ferries, G.R. and Arbanas, R.L. (1997). "Control/structure interaction in hydraulic power steering systems," The American Control Conference, pp.1146-1151.

Gillespie, T.D. (1992). "Fundamentals of Vehicle Dynamics." Warrendale, Pa : Society of Automotive Engineers.

Harter, W., Pfeiffer, W., Dominke, P., Ruck, G. and Blessing, P. (2000). "Future electrical steering systems: Realization with safety requirements," SAE Technical Paper Series 2000-01-0822.

Heathershaw, A. (2000). "Optimizing variable ratio steering for improved on-centre sensitivity and cornering control," SAE Technical Paper Series 2000-01-0821.

Heathershaw, A. (2004). "Matching of chassis and variable ratio steering characteristics to improve high speed stability," SAE Technical Paper Series 2004-01-1103.

ISO, (1996). "Hydraulic fluid power - Determination of pressure ripple levels generated in systems and components Part 1: Precision method for pumps," Ref. No. ISO 10767-1:1996(E).

ISO, (1996). "Hydraulic fluid power - Determination of pressure ripple levels generated in systems and components Part 2: Simplified method for pumps," Ref. No. ISO 10767-2:1999(E).

ISO, (1996). "Hydraulic fluid power - Determination of pressure ripple levels generated in systems and components Part 3: method for motors," Ref. No. ISO 10767-3:1999(E).

Kim, H.-S., Do, W.-J., Shim, J.-S. and Chol, S.-r. (2002). "The stability analysis of steering and suspension parameters on hands free motion," SAE Technical Paper Series 2002-01-0620.

Kumar, S., Kumar, D., M. L. Doughterty, S. and Spadafora, W.G. (1999). "Active reduction of pressure ripple in power steering systems," SAE Technical Paper Series 1999-01-0398.

Long, M.R. (1999). "Isolating hydraulic noise from mechanical noise in power rack & pinion steering systems," SAE Technical Paper Series 1999-01-0397.

Lozia, Z. and Zardecki, D. (2002). "Vehicle dynamics simulation with inclusion of freeplay and dry friction in steering system," SAE Technical Paper Series 2002-01-0619.

Matsunaga, T., Tanaka, T. and Nishimura, S. (2001). "Analysis of self-excited vibration in hydraulic power steering system: prevention against vibration by supply line," SAE Technical Paper Series 2001-01-0488.

McCloy D and Martin HR. (1980). "Control of Fluid Power: analysis and design," 2nd (Revised) Edition. Chichester [Eng.] : E. Horwood ; New York : Halsted Press.

Merritt, H.E. (1967). "Hydraulic Control Systems." New York : Wiley.

Milliken, W.F. and Milliken, D.L. (1995). "Race Car Vehicle Dynamics." Warrendale, PA, U.S.A. : SAE International.

Neureder, U. (2002). "Investigation into steering wheel nibble," Proceedings of the Institution of Mechanical Engineers Part D: Journal of Automobile Engineering, Vol. 216 (Special Issue), pp. 267-277.

Pacejka HB, (2002). "Tyre and Vehicle Dynamics," Oxford : Butterworth-Heinemann.

Phillips, R.W. (2003). "Self-excited vibration in hydraulic steering racks," SAE Technical Paper Series 2003-01-0580.

Post, J.W. and Law, E.H. (1996). "Modeling, characterization and simulation of automobile power steering systems for the prediction of on-center handling," SAE Technical Paper Series 960178.

Qatu, M., Llewellyn, D. and Edwards, R. (2000). "Correlation of hydraulic circuit dynamic simulation and vehicle," SAE Technical Paper Series 2000-01-0811.

Qatu, M.S., Llewellyn, D.R. and Spadafora, W.G. (2000). "Measurement of steering gear impedance," Experimenal Mechanics.

Sahinkaya, Y. (1996). "A novel steering vibration stabilizer," SAE Technical Paper Series 960930.

Sciortino, G. and Bamdad-Soofi, J. (1997). "Identification and elimination of steering systems squawk noise," SAE Technical Paper Series 972058.

Sharp, R.S. and Granger, R. (2003). "On car steering torque at parking speeds," Proceedings of the Institution of Mechanical Engineers Part D: Journal of Automobile Engineering, Vol. 217, pp. 87-96.

Smid, G.E., Qatu, M.S., Dougherty, M.L. and Drew, J. (1998). "Optimizing the power steering components to attenuate noise and vibrations," European Conference on Vehicle Noise and Vibration, pp. 103-112.

Smith, J.M., Ferries, G.R. and Arbanas, R.L. (1995). "An analytical control systems approach to steering shudder," SAE Technical Paper Series 951254.

Stecki, J.S. and Davis, D.C. (1986). "Fluid transmission lines - distributed parameter models. Part 1 : a review of the state of the art," Proceedings of the Institution of Mechanical Engineers, Vol. 200(A4), pp. 215-228.

Stecki, J.S. and Davis, D.C. (1986). "Fluid transmission lines - distributed parameter models. Part 2 : comparison of models," Proceedings of the Institution of Mechanical Engineers, 200(A4), pp. 229-236.

Taheri, S., Kazemi, R. and Tabatabai, M. (1998). "Analysis and optimization of vehicle steering system," SAE Technical Paper Series 981113.

Takeuchi, S. and Adachi, E. (1995). "Analysis and reduction of power steering noise during static steering operation," SAE Technical Paper Series 950581.

Tijsseling, A.S. (1996). "Fluid-structure interaction in liquid-fluid pipe systems: a review," Journal of Fluids and Structures, Vol. 10, pp.109-146.

Vijayakumar, S. and Barak, P. (2002). "Application of Bond Graph technique and computer simulation to the design of passenger car steering system," SAE Technical Paper Series 2002-01-0617.

Website 1, http://auto.howstuffworks.com/steering2.htm

Website 2, http://www.larescorp.com/tour.html

Website 3, http://www.aebishop.com/index.htm

Wong, T. (2001). "Hydraulic power steering system design and optimization simulation," SAE Technical Paper Series 2001-01-0479.

Wylie, E.B. and Streeter, V.L. (1993). "Fluid Transients in Systems." Englewood Cliffs, NJ 07632 : Prentice Hall.

Yang, K., Li, Q.S. and Zhang, L. (2004). "Longitudinal vibration analysis of multi-span liquid-filled pipelines with rigid constraints," Journal of Sound and Vibration, Vol. 273, pp. 125-147.